UNIVERSIDAD NACIONAL AUTÓNOMA DE MÉXICO

POSGRADO EN CIENCIA E INGENIERÍA DE MATERIALES

INSTITUTO DE INVESTIGACIONES EN MATERIALES

Structural, Electronic, and Thermodynamic Properties of Complex Materials. Simulation of the Binary Alloys AuAg, CuBi, and BN.

T E S I S

QUE PARA OPTAR POR EL GRADO DE

DOCTOR EN CIENCIA E INGENIERÍA DE MATERIALES

PRESENTA:

M. en C. DAVID HINOJOSA ROMERO

TUTOR PRINCIPAL

DR. ARIEL ALBERTO VALLADARES CLEMENTE
INSTITUTO DE INVESTIGACIONES EN MATERIALES, UNAM

COMITÉ TUTOR

DR. JUAN CARLOS ALONSO HUITRÓN
INSTITUTO DE INVESTIGACIONES EN MATERIALES, UNAM

DRA. RENELA MARÍA VALLADARES MC NELIS
FACULTAD DE CIENCIAS, UNAM

CIUDAD DE MÉXICO, MARZO 2023

This page intentionally left blank

Declaración de Autoría

Yo, M. en C. David Hinojosa Romero, declaro que esta tesis titulada, "Structural, Electronic and Thermodynamic Properties of Complex Materials. Simulation of the Binary Alloys AuAg, CuBi, and BN." y el trabajo presentado en ella son de mi autoría.

Yo confirmo que:

- Este trabajo fue hecho totalmente durante el periodo de mis estudios de Doctorado en el Posgrado en Ciencia e Ingeniería de Materiales (PCeIM) de la Universidad Nacional Autónoma de México (UNAM).
- Ninguna parte del presente trabajo ha sido usada para algún tipo de grado en la UNAM, ni en alguna otra Institución.
- La autoría de todo el material consultado se le atribuye debidamente a sus respectivos autores.
- Cuando se ha citado el trabajo de otros autores, siempre se ha dado la fuente de origen. Con la excepción de dichas citas, la totalidad de la información contenida en el presente trabajo es de mi autoría.
- He reconocido todas las fuentes de ayuda usadas en este trabajo.
- He especificado cuando el trabajo fue hecho en colaboración con otros.

Firma:

_____

Marzo 2023

This page intentionally left blank

Declaration of Authorship

I, M.Sc. David Hinojosa Romero, declare that this thesis titled, "Structural, Electronic and Thermodynamic Properties of Complex Materials. Simulation of the Binary Alloys AuAg, CuBi, and BN." and the work presented in it is my own. I confirm that:

- This work was done wholly while pursuing a PhD degree in Materials Science and Engineering at Universidad Nacional Autónoma de México (UNAM).
- No part of this work has been used for any type of degree at UNAM or at any other Institution.
- Where I have consulted the published work of others, this is always clearly attributed.
- Where I have quoted from the work of others, the source is always given. With the exception of such quotations, this thesis is entirely my own work.
- I have acknowledged all main sources of help.
- Where the thesis uses work done by myself jointly with others, I have specified it.

Signature:

_____

March 2023

This page intentionally left blank

"*Most elementary physics textbooks describe a world that seems filled with very simple, regular and symmetrical systems. A student might get the impression* [...] *that regular crystalline solids are 'typical' materials.* [...] *If our hypothetical students look at the world with an unbiased eye, they will see a richness quite unlike anything described in physics texts. In the real world, simplicity is a rare exception.*"

Leo P. Kadanoff - *On complexity.* Physics Today **40**, 3 (1987), 7-9.

"*Thus, the theorist is required to abandon tried and true procedures and to exercise taste and judgement; he is driven out of his comfortable, well troden ways, and is forced to be creative, a skill which is neither taught in courses, nor rewarded, very reliably, by the NSF and other funding agencies.*"

Phillip W. Anderson - *Brainwashed by Feynman?* Physics Today **53**, 2 (2000), 11-12.

This page intentionally left blank

UNIVERSIDAD NACIONAL AUTÓNOMA DE MÉXICO

Posgrado en Ciencia e Ingeniería de Materiales

Doctor en Ciencia e Ingeniería de Materiales

Resumen

Structural, Electronic and Thermodynamic Properties of Complex Materials. Simulation of the Binary Alloys AuAg, CuBi, and BN.

por M. en C. David Hinojosa Romero

La presente tesis consta de dos partes. En la primer parte se estudian tres diferentes aleaciones binarias desde un enfoque *ab initio*: i) la aleación sustitucionalmente desordenada Au_xAg_{100-x} ($x = 0, 4, 13, 20, 30, 40, 50, 75, 90,$ y 100) en las que se calculó la contribución electrónica al calor específico, obteniendo una comparación cualitativa favorable con los resultados experimentales reportados en la literatura; ii) la aleación amorfa $Cu_{61}Bi_{39}$ en la que se calculó su temperatura crítica superconductora, T_c, como $4.2\,\mathrm{K}$; y iii) el sistema amorfo BN equiatómico en el que se calculó la contribución fonónica a la energía interna y al calor específico. Estos cálculos contribuyen al desarrollo de un método eficiente de simulación de aleaciones en el que se considere el ambiente atómico local en cada sistema desde un enfoque *ab initio*. En la segunda parte se investigan los cambios en la T_c del bismuto puro debidos a modificaciones de su estructura electrónica y fonónica al encontrarse en tres estados: i) bajo presión externa manteniendo las simetrías de la estructura Wyckoff (estable bajo condiciones estándar), encontrando una disminución en la T_c al aumentar la presión externa; ii) en bicapas, utilizando un *slab model* con $5\,\text{Å}$, $10\,\text{Å}$, y $20\,\text{Å}$ de separación intercapa de la superficie (111) de la estuctura Wyckoff, encontrando $T_c = 0.08\,\mathrm{K}$, $2.61\,\mathrm{K}$, y $2.42\,\mathrm{K}$ respectivamente para cada separación intercapa; y iii) en las cuatro fases cristalinas bajo presión, calculando $T_c = 3.9\,\mathrm{K}$ para Bi-II, $T_c = 7\,\mathrm{K}$ para Bi-III, y $T_c = 6.8\,\mathrm{K}$ para Bi-V, de acuerdo con los valores reportados experimentalmente, y prediciendo una T_c de $4.25\,\mathrm{K}$ para la fase Bi-IV. Con esta extensión al estudio de las fases superconductoras del bismuto, el método utilizado para determinar las T_c (originalmente publicado en 2016 para Bi-I) muestra su potencial para ser aplicado a otros sistemas metálicos con la capacidad de predecir un estado superconductor. De esta manera se demuestra que el estudio de los sistemas complejos a través de simulaciones computacionales es tratable mediante nuestros enfoques.

This page intentionally left blank

UNIVERSIDAD NACIONAL AUTÓNOMA DE MÉXICO

Posgrado en Ciencia e Ingeniería de Materiales

Ph.D. Materials Science and Engineering

Abstract

Structural, Electronic and Thermodynamic Properties of Complex Materials. Simulation of the Binary Alloys AuAg, CuBi, and BN.

by M.Sc. David Hinojosa Romero

This thesis is divided into two parts. In the first part, the study of three different alloys from an *ab initio* approach is reported: i) the substitutionally disordered Au_xAg_{100-x} alloy for $x = 0$, 4, 13, 20, 30, 40, 50, 75, 90, and 100 in which the electronic contribution to the specific heat was calculated, finding a good qualitative comparison with experiments; ii) the $Cu_{61}Bi_{39}$ amorphous alloy, whose critical superconducting temperature, T_c, was calculated to be $4.2\,\mathrm{K}$; and iii) the amorphous BN system for the equiatomic concentration for which the phonon contribution to the internal energy and constant-volume specific heat were obtained. These calculations contribute to the development of an efficient method for the simulation of alloys that incorporates the local atomic environment from an *ab initio* approach. In the second part, changes in the T_c of pure bismuth are reported due to variations in its electronic structure and phonon frequency spectrum when being in three states: i) under external pressure conserving the symmetries of the Wyckoff structure (the stable structure under ambient conditions), finding lower T_cs for higher external pressures; ii) in the bilayered structure, using a slab model of the (111) surface of the Wyckoff structure and $5\,\text{Å}$, $10\,\text{Å}$, and $20\,\text{Å}$ of interlayer separation, obtaining T_c =$0.08\,\mathrm{K}$, $2.61\,\mathrm{K}$, and $2.42\,\mathrm{K}$ for each separation, respectively; and iii) the four crystalline under-pressure phases, calculating $T_c = 3.9\,\mathrm{K}$ for Bi-II, $T_c = 7\,\mathrm{K}$ for Bi-III, and $T_c = 6.8\,\mathrm{K}$ for Bi-V, in agreement with the measured values, and predicting a T_c of $4.25\,\mathrm{K}$ for Bi-IV. With this extension to the study of the superconducting phases of bismuth, the followed method to compute the T_c (originally published in 2016 for Bi-I), shows its potential to be applied to other metallic systems and to predict a superconducting behavior. Thereby, it is shown that the study of complex systems by computational simulations is feasible through our approaches.

This page intentionally left blank

List of Publications

The investigation reported in the present thesis produced the seven papers numbered below from 1 to 7. Five of them, numbered below from 1 to 5, are already published and their first page is reproduced immediately after the List of Publications. The remaining published papers in the list, numbered from 8 to 13, are investigations in which this thesis' author has collaborated.

1. David Hinojosa-Romero, Isaías Rodríguez, Zaahel Mata-Pinzón, Alexander Valladares, Renela Valladares and Ariel A. Valladares. **Compressed Crystalline Bismuth and Superconductivity - An *ab initio* Computational Simulation**. *MRS Advances* **2** (2017), pp. 499-506. DOI: 10.1557/adv.2017.66.

2. David Hinojosa-Romero, Isaías Rodríguez, Alexander Valladares, Renela M. Valladares and Ariel A. Valladares. **Possible superconductivity in Bismuth (111) bilayers. Their electronic and vibrational properties from first principles**. *MRS Advances* **3** (2018), pp. 313-319. DOI: 10.1557/adv.2018.119.

3. Ariel A. Valladares, Isaías Rodríguez, David Hinojosa-Romero, Alexander Valladares, and Renela M. Valladares. **Possible superconductivity in the Bismuth IV solid phase under pressure**. *Scientific Reports* **8** (2018), 5946. DOI: 10.1038/s41598-018-24150-3.

4. David Hinojosa-Romero, Isaías Rodríguez, Alexander Valladares, Renela M. Valladares and Ariel A. Valladares. ***Ab initio* Study of the Amorphous Cu-Bi System**. *MRS Advances* **4** (2019), pp. 81-86. DOI: 10.1557/adv.2019.83.

5. Isaías Rodríguez, David Hinojosa-Romero, Alexander Valladares, Renela M. Valladares and Ariel A. Valladares. **A facile approach to calculating superconducting transition temperatures in the bismuth solid phases**. *Scientific Reports* **9** (2019), 5256. DOI: 10.1038/s41598-019-41401-z.

6. David Hinojosa-Romero, Alexander Valladares, Renela M. Valladares, Isaías Rodríguez, and Ariel A. Valladares. **Amorphous Boron Nitride: Ab initio Study of its vibrational properties**. *Under review*.

7. David Hinojosa-Romero, Alexander Valladares, Renela M. Valladares, Isaías Rodríguez, and Ariel A. Valladares. **CASA: A Chemical Approach to the Study of Alloys. The $\mathbf{Au}_x\mathbf{Ag}_{100-x}$ alloy as a case study**. *To be published*.

8. Isaías Rodríguez, Renela M. Valladares, David Hinojosa-Romero, Alexander Valladares and Ariel A. Valladares. **Emergence of magnetism in bulk amorphous palladium**. *Physical Review B* **100** (2019), 024422. DOI: 10.1103/PhysRevB.100.024422.

9. Isaías Rodríguez, Renela M. Valladares, Alexander Valladares, David Hinojosa-Romero, Ulises Santiago, and Ariel A. Valladares. **Correlation: An Analysis Tool for Liquids and for Amorphous Solids**. *The Journal of Open Source Software* **6** (2021), 2976. DOI: 10.21105/joss.02976.

10. Isaías Rodríguez, Renela M. Valladares, Alexander Valladares, David Hinojosa-Romero, and Ariel A. Valladares. **Ab initio studies of magnetism and topology in solid Pd-rich a-PdSi alloys**. *Scientific Reports* **12** (2022), 4624. DOI: 10.1038/s41598-022-08656-5.

11. Isaías Rodríguez, Renela M. Valladares, Alexander Valladares, David Hinojosa-Romero, and Ariel A. Valladares. **Superconductivity Versus Magnetism in the Amorphous Palladium "Ides": $\mathbf{Pd}_{1-c}$(H/D/T)$_c$**. *Journal of Low Temperature Physics* **209** (2022), pp. 232-243. DOI: 10.1007/s10909-022-02807-8.

12. Flor B. Quiroga, David Hinojosa-Romero, Alexander Valladares, Renela M. Valladares, Isaías Rodríguez, and Ariel A. Valladares. **The effect of negative pressures on the superconductivity of amorphous and crystalline bismuth**. *Scientific Reports* **12** (2022), 19278. DOI: 10.1038/s41598-022-22261-6.

13. Isaías Rodríguez, Renela M. Valladares, Alexander Valladares, David Hinojosa-Romero, and Ariel A. Valladares. **Short-Range Atomic Topology of Ab Initio Generated Amorphous PdSi Alloys**. *Advanced Theory and Simulations* (2023), 2200399. DOI: 10.1002/adts.202200399.

MRS Advances © 2017 Materials Research Society
DOI: 10.1557/adv.2017.66

Compressed Crystalline Bismuth and Superconductivity−An *ab initio* computational Simulation

David Hinojosa-Romero[1], Isaías Rodríguez[2], Zaahel Mata-Pinzón[1], Alexander Valladares[2], Renela Valladares[2], and Ariel A. Valladares[1 *]

[1]Instituto de Investigaciones en Materiales, Universidad Nacional Autónoma de México, Apartado Postal 70-360, Ciudad Universitaria, México, D.F. 04510, México.

[2]Facultad de Ciencias, Universidad Nacional Autónoma de México, Apartado Postal 70-542, Ciudad Universitaria, México, D.F. 04510, México

*valladar@unam.mx

ABSTRACT

Bismuth displays puzzling superconducting properties. In its crystalline equilibrium phase, it does not seem to superconduct at accessible low temperatures. However, in the amorphous phase it displays superconductivity at ~ 6 K. Under pressure bismuth has been found to superconduct at T_cs that go from 3.9 K to 8.5 K depending on the phase obtained. So the question is: what electronic or vibrational changes occur that explains this radical transformation in the conducting behavior of this material? In a recent publication we argue that changes in the density of electronic and vibrational states may account for the behavior observed in the amorphous phase with respect to the crystal. We have now undertaken an *ab initio* computational study of the effects of pressure alone maintaining the original crystalline structure and compressing our supercell computationally. From the results obtained we infer that if the crystal structure remains the same (except for the contraction), no superconductivity will appear.

INTRODUCTION

Bismuth (Bi) is an interesting material for besides having a very high thermal conductivity, this semimetal displays puzzling superconducting properties. In its crystalline equilibrium phase it does not seem to display superconductivity at low temperatures. However, in the amorphous phase it displays superconductivity at ~ 6 K [1]. Under pressure bismuth has been found to superconduct at 2.55 GPa (Bi-II monoclinic crystalline phase), 2.7 GPa (Bi-III tetragonal phase) and 7.7 GPa (Bi-V body centered cubic phase), having superconducting transition temperatures of T_c = 3.9 K, 7.2 K and 8.5 K, respectively [2]. Therefore, it is desirable to investigate what changes in the electronic or vibrational properties occur that may explain this radical transformation in the conducting behavior of this material. In a recent publication [3] we argue that changes in the density of electronic and vibrational states may account for the behavior in the amorphous phase. That is why we have carried out an *ab initio* computational study of the effects of structural changes when crystalline Bi is subjected to pressure. In order to see the effect of pressure alone we maintain the original crystalline structure and computationally compress our sample, a 64–atom supercell with periodic boundary conditions, between 0 and 15

MRS Advances © 2018 Materials Research Society
DOI: 10.1557/adv.2018.119

Possible superconductivity in Bismuth (111) bilayers. Their electronic and vibrational properties from first principles

David Hinojosa-Romero[1], Isaías Rodriguez[2], Alexander Valladares[2], Renela M. Valladares[2] and Ariel A. Valladares[1] *.

[1]*Instituto de Investigaciones en Materiales, Universidad Nacional Autónoma de México, Apartado Postal 70-360, Ciudad Universitaria, CDMX, 04510, México.*
[2]*Facultad de Ciencias, Universidad Nacional Autónoma de México, Apartado Postal 70-542, Ciudad Universitaria, CDMX, 04510, México*

* Corresponding Author: Ariel A. Valladares, valladar@unam.mx

ABSTRACT

Using a 72-atom supercell we report ab initio calculations of the electronic and vibrational densities of states for the bismuth (111) bilayers (bismuthene) with periodic boundary conditions and a vacuum of 5 Å, 10 Å and 20 Å. We find that the electronic density of states shows a metallic character at the Fermi level and that the vibrational density of states manifests the expected gap due to the layers. Our results indicate that a vacuum down to 5 Å does not affect the electronic and vibrational structures noticeably. A comparison of present results with those obtained for the Wyckoff structure is displayed. Assuming that the Cooper pairing potential is similar for all phases and structures of bismuth, an estimate of the superconducting transition temperature gives 2.61 K for the bismuth bilayers.

INTRODUCTION

Bulk bismuth is known to be a semimetal, a metal or a superconductor, with peculiar electronic and vibrational properties depending on whether it is crystalline or amorphous or depending on the pressure applied on it. At ambient pressure and temperature, it crystallizes in the Wyckoff structure, Bi-I, [1] with rhombohedral symmetry in which each atom has three equidistant nearest-neighbor atoms and three equidistant next-nearest neighbors slightly further away, resulting in a buckled 2D honeycomb bilayer lying perpendicular to the [111] crystallographic direction.

Bismuthene, or the bilayers (111) of bismuth, Bi (111), recently has been the subject of much interest and investigation as an example of non-carbon low-dimensional materials and the influence of this low dimensionality on its electronic and transport properties. It has been argued that in this layered form, bismuth has properties of topological insulators [2-4] which are bulk insulators with protected boundary states [5]. This state of matter appears when there is an inversion in the electronic bands of 2D materials caused by perturbations [6]. Among the perturbing agents the following are

www.nature.com/scientificreports

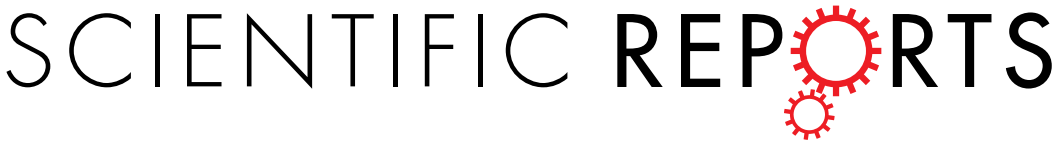

OPEN

Possible superconductivity in the Bismuth IV solid phase under pressure

Received: 15 November 2017
Accepted: 19 February 2018
Published online: 13 April 2018

Ariel A. Valladares[1], Isaías Rodríguez[2], David Hinojosa-Romero[1], Alexander Valladares[2] & Renela M. Valladares[2]

The first successful theory of superconductivity was the one proposed by Bardeen, Cooper and Schrieffer in 1957. This breakthrough fostered a remarkable growth of the field that propitiated progress and questionings, generating alternative theories to explain specific phenomena. For example, it has been argued that Bismuth, being a semimetal with a low number of carriers, does not comply with the basic hypotheses underlying BCS and therefore a different approach should be considered. Nevertheless, in 2016 based on BCS we put forth a prediction that Bi at ambient pressure becomes a superconductor at 1.3 mK. A year later an experimental group corroborated that in fact Bi is a superconductor with a transition temperature of 0.53 mK, a result that eluded previous work. So, since Bi is superconductive in almost all the different structures and phases, the question is why Bi-IV has been elusive and has not been found yet to superconduct? Here we present a study of the electronic and vibrational properties of Bi-IV and infer its possible superconductivity using a BCS approach. We predict that if the Bi-IV phase structure were cooled down to liquid helium temperatures it would also superconduct at a T_c of 4.25 K.

Bardeen, Cooper and Schrieffer (BCS) explained superconductivity by invoking two important concepts: The phonon-mediated electron Cooper pairing that occurs due to the vibrations in the material, giving rise to the transition to the superconducting state, and the coherent motion of the paired electrons that gives them the inertia to sustain electrical currents for a long time without dissipation. Simple but revolutionary. Several variations of these ideas have appeared in the course of time and even different concepts that pretend to substitute the original ones. Since vibrations are invoked to be the main factor leading to a bound electron pair, some manifestation of such interaction should appear in the phenomenon, and it does: the isotope effect. The Meissner effect is also duly accounted for and then the two main aspects of superconductivity are borne out by the BCS theory. Superconducting-like phenomena have been invoked in other realms of physics like nuclear and elementary particles where the pairing mechanism should be adequately chosen. It has also been ventured that in principle all materials may become superconductors if cooled down to low enough temperatures. We here show that invoking the corresponding electron and vibrational densities of states we can predict superconductivity, provided the Cooper attraction sets in. This elemental approach, if proven correct, would indicate that superconductivity in bismuth can be understood in a simple manner without invoking eccentric mechanisms.

In a very recent work[1] we computationally generated an amorphous structure of bismuth (*a*-Bi), characterized its topology, showed that it agreed remarkably well with experiment and then proceeded to calculate its electronic, $N(E)$, and vibrational, $F(\omega)$, densities of states to study their effect on the superconducting properties of this amorphous Bi phase. By comparing these results with the corresponding ones for the crystalline (Wyckoff) structure at atmospheric pressure we predicted that the crystalline material should become a superconductor at a temperature $T_c \leq 1.3$ mK[1]. A year later an experimental group reported that, in fact, the Wyckoff phase is superconductive with a transition temperature of 0.53 mK[2], in agreement with our prediction. Encouraged by this success we decided to undertake a systematic study of the superconductivity of the solid phases of Bi under pressure and, in this paper, we put forth another prediction: the solid phase of bismuth known as Bi-IV, hitherto considered non-superconducting, should become a superconductor with a transition temperature close to the boiling

[1]Instituto de Investigaciones en Materiales, Universidad Nacional Autónoma de México, Apartado Postal 70-360, Ciudad Universitaria, CDMX, 04510, México. [2]Facultad de Ciencias, Universidad Nacional Autónoma de México, Apartado Postal 70-542, Ciudad Universitaria, CDMX, 04510, México. Correspondence and requests for materials should be addressed to A.A.V. (email: valladar@unam.mx)

MRS Advances © 2019 Materials Research Society
DOI: 10.1557/adv.2019.83

Ab initio Study of the Amorphous Cu-Bi System

D. Hinojosa-Romero[1], I. Rodriguez[2], A. Valladares[2], R. M. Valladares[2], A. A. Valladares[1*]

1 Condensed Matter Department, Instituto de Investigaciones en Materiales, UNAM.

2 Physics Department, Facultad de Ciencias, UNAM.

* Corresponding Author: Ariel A. Valladares, valladar@unam.mx

ABSTRACT

As a pure element, bismuth is a semimetal which possesses several interesting physical properties, not all of them well understood. The recent discovery of superconductivity, as predicted by our group, and the increasing superconducting transition temperature as the pressure applied increases, are some examples of its particularities. Also, the fact that the amorphous phase is superconductive with a transition temperature several orders of magnitude larger than the crystalline at ambient pressure is unusual. These phenomena have also motivated our predictions for the transition temperatures of Bi-bilayers and the Bi-IV phase. When mixed with other elements, bismuth seems to contribute to the superconducting character of the resulting material. Here we study the binary copper-bismuth amorphous system which is known to superconduct in diverse compositions. Using ab initio molecular dynamics and the undermelt-quench method, we generate an amorphous structure for a 144-atom supercell corresponding to the $Cu_{61}Bi_{39}$ system. We calculate the electronic and vibrational densities of states for the amorphous system and estimate a superconducting critical temperature of 4.2 K for the amorphous state.

INTRODUCTION

Superconductivity, a phenomenon in which an electrical current can flow through a material with no resistance, has been an appealing field of study since its discovery on mercury, tin and lead by H. Kamerlingh Onnes in 1911 [1]. Later in 1957, J. Bardeen, L. Cooper and J. R. Schrieffer [2] proposed a microscopic theory of superconductivity based on the coupled movement of electrons through the material, leading also to a correct

www.nature.com/scientificreports

SCIENTIFIC REPORTS

OPEN

A facile approach to calculating superconducting transition temperatures in the bismuth solid phases

Received: 20 August 2018
Accepted: 5 March 2019
Published online: 27 March 2019

Isaías Rodríguez[1], David Hinojosa-Romero[2], Alexander Valladares[1], Renela M. Valladares[1] & Ariel A. Valladares[2]

All solid phases of bismuth under pressure, but one, have been experimentally found to superconduct. From Bi-I to Bi-V, avoiding Bi-IV, they become superconductors and perhaps Bi-IV may also become superconductive. To investigate the influence of the electronic properties *N(E)* and the vibrational properties *F(ω)* on their superconductivity we have *ab initio* calculated them for the corresponding experimental crystalline structures, and using a BCS approach have been able to determine their critical temperatures T_c obtaining results close to experiment: For Bi-I (The Wyckoff Phase) we predicted a transition temperature of less than 1.3 mK and a year later a T_c of 0.5 mK was measured; for Bi-II T_c is 3.9 K measured and 3.6 K calculated; Bi-III has a measured T_c of 7 K and 6.5 K calculated for the structure reported by Chen *et al.*, and for Bi-V T_c ~ 8 K measured and 6.8 K calculated. Bi-IV has not been found to be a superconductor, but we have recently predicted a T_c of 4.25 K.

When superconductivity was discovered by Kamerlingh Onnes in mercury in 1911 ($T_c \sim 4.2$ K)[1] after he produced liquid helium for the first time in 1908 (boiling point of 4.2 K at atmospheric pressure) this phenomenon was assumed only to consist of a vanishing electrical resistance for some metallic materials. It was not until the Meissner effect (the expulsion of magnetic fields) was observed that this discovery became a puzzle. Now superconductivity is displayed by many and sundry materials and is characterized by exhibiting zero electrical resistance and the above-mentioned Meissner effect below a characteristic temperature T_c, the superconducting transition temperature.

In 1957 Bardeen, Cooper and Schrieffer (BCS)[2] developed the first successful theory of superconductivity based on two simple but revolutionary and decisive concepts. They proposed that electrons pair through the atomic vibrations in the material due to the now known Cooper pairing potential, and that this pairing gives rise to the transition to the superconducting state; also, that the coherent motion of the paired electrons gives them the inertia to sustain electrical currents without dissipation[2]. Alternative ideas have appeared since then and even different concepts to substitute the initial ones but BCS has withstood the passing of time. Since phonons are invoked to be responsible for the electron pairing, a manifestation of this interaction should appear in superconductivity, and it does: the so-called isotope effect which is the dependence of T_c on the isotopic mass, $T_c\sqrt{M} = \text{const}$. The Meissner effect is also borne out; hence the two main aspects of superconductivity are duly accounted for by the BCS theory.

Due to the variety and abundance of materials that superconduct, it has also been ventured that in principle all materials may become superconductors if cooled down to low enough temperatures. In what follows we demonstrate that invoking the corresponding electronic densities of states, $N(E)$, and the vibrational densities of states, $F(\omega)$, for the various solid phases of bismuth under pressure, the superconducting transition temperatures can be calculated if the Cooper attraction sets in with a strength comparable for all phases. This facile approach, if proven correct, can be generalized to study phases of other materials similarly related.

[1]Facultad de Ciencias, Universidad Nacional Autónoma de México, Apartado Postal 70-542, Ciudad Universitaria, México City, CDMX, 04510, Mexico. [2]Instituto de Investigaciones en Materiales, Universidad Nacional Autónoma de México, Apartado Postal 70-360, Ciudad Universitaria, México City, CDMX, 04510, Mexico. Correspondence and requests for materials should be addressed to A.A.V. (email: valladar@unam.mx)

This page intentionally left blank

Agradecimientos

En primer lugar, agradezco a mi tutor, el Dr. Ariel Valladares, por permitirme continuar mi formación académica dentro de su grupo de investigación. Sus consejos y sabia dirección a lo largo de estos 8 años de Posgrado (12, desde que tomé su clase) han logrado concretar este esfuerzo que se llama Doctorado. Reitero que es un mentor, en la academia y en la vida.

Agradezco también a mi comité tutor: el Dr. Juan Carlos Alonso Huitrón y la Dra. Renela Valladares Mc Nelis, por su dirección y comentarios críticos y constructivos hacia esta investigación.

Agradezco a la Dra Vicenta Sánches Morales (FC, UNAM), al Dr. Gerardo Jorge Vázquez Fonseca (IF, UNAM), a la Dra. Angélica Estrella Ramos Peña (IIM, UNAM) y al Dr. Ricardo Méndez Fragoso (FC, UNAM) por sus observaciones y comentarios dirigidos a mejorar esta tesis. Las omisiones y errores que se pudieran encontrar en este trabajo son mi entera responsabilidad.

Agradezco infinitamente al Programa de Becas Nacionales del Consejo Nacional de Ciencia y Tecnología, CONACyT, por la beca otorgada para realizar mis estudios de Doctorado.

Por permitirme contribuir a las tareas fundamentales de nuestra UNAM, agradezco al Instituto de Investigaciones en Materiales y a la Facultad de Ciencias, lugares donde me desarrollé como incipiente investigador y docente. Agradezco enormemente a todo el personal de la Biblioteca del IIM, en especial a la Mtra. Ma. Teresa Vázquez Mejía y a la Lic. Oralia Leticia Jiménez Alvarez, por su enorme y atento apoyo hacia nosotros.

Agradezco también al Posgrado en Ciencia e Ingeniería de Materiales, PCeIM, por permitirme continuar mi formación académica dentro de su Programa de Doctorado que, mediante su enfoque interdisciplinario, fomenta una mejor preparación y educación integral para sus alumnos. Gracias a su Comité Académico, a sus profesores y personal administrativo, todos ellos, junto con los alumnos, hacen del PCeIM un posgrado de gran calidad.

Un gran reconocimiento y agradecimiento a la Dirección General de Cómputo y de Tecnologías de Información y Comunicación, DGTIC, por permitirme realizar parte de las simulaciones en Miztli, así como por su eficiente respuesta y solución a los problemas que surgían.

La presente investigación fue realizada gracias al Programa de Apoyo a Proyectos de Investigación e Innovación Tecnológica (PAPIIT) de la UNAM, en el proyecto IN116520. Agradezco a la DGAPA-UNAM la beca recibida para concluir este trabajo.

This page intentionally left blank

Contents

This page intentionally left blank

List of Figures

List of Tables

This page intentionally left blank

List of Abbreviations

DFT	**D**ensity **F**unctional **T**heory
H-K	**H**ohenberg-**K**ohn
K-S	**K**ohn-**S**ham
LDA	**L**ocal **D**ensity **A**pproximation
GGA	**G**eneralized **G**radient **A**pproximation
VWN	**V**osko **W**ilk **N**usair
PBE	**P**erdew **B**urke **E**rnzerhof
MD	**M**olecular **D**ynamics
NVT	Constant **N**umber of Particles, **V**olume and **T**emperature
DND	**D**ouble **N**umerical plus **d** polarization functions
DSPP	**D**ensity Functional **S**emicore **P**seudo**P**otential
eDoS	**e**lectronic **D**ensity **o**f **S**tates
vDoS	**v**ibrational **D**ensity **o**f **S**tates
tPDF	**t**otal **P**air **D**istribution **F**unction
pPDF	**p**artial **P**air **D**istribution **F**unction
PADF	**P**lane **A**ngle **D**istribution **F**unction

This page intentionally left blank

A mis adoradas
Tere Romero Hernández y Claudia Villa Romero.

This page intentionally left blank

Objectives

The general objective for this work is the accurate quantum-mechanical calculation of electronic and thermodynamic properties of complex materials using first-principles simulation methods that adequately incorporate the local atomic environment in these materials. The properties of interest are the electronic and phononic contributions to the specific heat, the critical superconducting transition temperature, and the lattice contribution to the internal energy. The materials for which these properties are to be investigated are substitutionally and topologically disordered binary alloys, and pure crystalline materials under external pressures; these materials are chosen to investigate if the developed simulation methods adequately describe both metallic and insulating systems.

The specific objectives are:

- The calculation of the electronic specific heat of the Au_xAg_{100-x} system and its comparison with published results.
- The successful generation of an amorphous structure of the $Cu_{61}Bi_{39}$ alloy and calculation of its superconducting critical temperature.
- The successful generation of an amorphous structure of the equiatomic BN system and determination of the phonon contribution to some thermodynamic properties.
- The determination of the superconducting critical temperatures of pure, crystalline bismuth in different conditions, such as under pressure and in the bilayered form.

This page intentionally left blank

Preface

Materials Science is a multidisciplinary area of knowledge in which scientists, both theorists and experimentalists, merge their particular knowledge to enhance and create new devices that can be used for the well being of mankind. The fundamental idea is to understand the relation *structure-properties* for materials and this can be traced back, within the condensed matter realm [1], to the knowledge of how their atoms interact with each other and how they arrange themselves in the structure.

Advances in science, specifically in Physics with the development of quantum mechanics at the beginning of the 20th century, allowed us to understand some phenomena that occur on the atomic scale and in this way to be able to explain some of the macroscopic properties observed in Nature. However, the detailed study of complex systems was only possible until the development of computers and the creation of codes based on empirical methods and on first principles (*ab initio*), in such a way that it was possible to use quantum theory to understand the origin of the properties of practically any system.

Thus, thanks to computational experiments, it is now possible to predict the characteristics that a material would have in a large number of situations, from the change in its structure or atomic composition to when it is subjected to conditions difficult to achieve in a laboratory, such as high pressures or very low temperatures. In this way, numerical simulation can be considered as a link between the theoretical description and the experimental measurement of natural phenomena, in particular of the physical properties of materials. This fundamental and powerful tool may be applied to explore the properties from monoatomic crystals to DNA molecules; being the level of theory and the power for the computation two of the most difficult obstacles to overcome.

Starting from the basics, monoatomic crystals have been the subject of study of solid-state science since the application of quantum theory to their study. The reason for this is that those solids are assumed to be arranged in a perfect periodic lattice and the mathematical theory needed for their description was already well understood and ready to be applied in the solution of technological problems. Despite that solid-state theory fundamentally deals with perfect solids, rarely found in nature, its success is undeniable: the electronic devices mankind has created are examples of the successfully *structure-properties* knowledge acquired from simple models.

Realizing that *real* materials do not present the perfect crystalline structure that the majority of solid-state textbooks describe, the next step in increasing complexity for the study of condensed systems may be given in any direction, but always with the aim, perhaps impossible to reach, to construct a theory that fully describes their macroscopic physical and chemical properties. In this sense, two appealing and interesting fields of research are to be studied: binary disordered alloys and the effects of external pressure on the physical properties of materials; thereby, the present work explores these two topics from a quantum-mechanical simulation approach within the Density Functional Theory framework.

The first part of this thesis addresses the study of three binary alloys: Au_xAg_{100-x}, $Cu_{61}Bi_{39}$, and BN, each one with specific characteristics that provide them a disordered character. Within this part, the electronic contribution to the specific heat is studied for the substitutionally disordered Au_xAg_{100-x} alloy for gold atomic percentage concentrations $x = 0$, 4, 13, 20, 30, 40, 50, 75, 90, and 100. Also, amorphous structures and their characterization by pair correlation functions are reported for the metallic alloy $Cu_{61}Bi_{39}$ and the semiconductor BN in equiatomic concentration; the superconducting transition temperature is reported for the $Cu_{61}Bi_{39}$ alloy and the phonon contribution to the internal energy and to the specific heat are reported for BN. The motivation to study those three alloys is to prove that our approaches for first-principles simulation methods can be applied to metallic as well as to insulating systems.

The second part of this thesis revolves around superconductivity in pure crystalline bismuth. Here, the electronic and phononic energy spectra that lead to the estimation (within the BCS theory of superconductivity formalism) of the superconducting transition temperature (T_c) for the pure metal under three different conditions are reported. Changes in the T_c due to the application of external pressures up to $14.5\,\mathrm{GPa}$ on the stable structure at ambient conditions (known as the Wyckoff structure, corresponding to the Bi-I phase), are studied by analyzing compressed supercells that have the same symmetries of the Wyckoff structure. Also, the possibility of superconducting behavior in bismuth bilayers (which correspond to the (111) surface in the Wyckoff structure) is explored and a critical temperature is predicted for this two-dimensional structure of bismuth. Finally, the stable structures under pressure according to the bismuth phase diagram are considered. Specifically, critical temperatures for the Bi-II, the controversial Bi-III, and the Bi-V phases are calculated and compared with measured values reported in literature; for the Bi-IV phase, our predicted T_c awaits experimental verification. Our interest in the superconducting behavior of bismuth arises from the fact that it is a metal that maintains this state under several conditions.

Part I

Alloys

This page intentionally left blank.

1 Introduction

The study of alloys from a theoretical perspective is of great relevance since, from the fundamental knowledge of their physical and chemical properties, one can design useful materials with applications in several other fields of science. However, a fundamental theory of alloys has not yet seen the light due to the greater mathematical and computational challenges this represents compared to the theory of *perfect*, crystalline solids.

Emphasis is made on in the concept of a *perfect* solid, which is understood as a material whose atoms are assumed to occupy periodic positions according to a crystalline lattice that spans the whole space. The regularities in the spatial distribution of atoms make it possible to define a primitive cell that, while preserving the geometric symmetries of the bulk, contains the minimum number of entities such that the entire three-dimensional *perfect* solid is reproduced when the cell is repeated along three non-coplanar axes (or two non-colinear axes for two-dimensional materials) [2]. Since the mathematical methods for periodic functions were already developed, it is not surprising that perfect solids were the first systems to be studied under the quantum mechanics framework, giving rise to the so called *solid-state* theory [3].

Along with the successful technological advances that solid-state theory fostered since the middle of the 20th century, interests began to arise in non-perfect, *disordered* materials (e.g. alloys and amorphous solids) for which a primitive cell construction cannot be made due to the lack of periodicity. In this sense, the *disordered* concept emerges to label those materials which deviate from the periodic description of the *ordered*, crystalline solids [4], giving as consequences emerging challenges in their mathematical formulation which have prevented the development of a general theory of disordered media.

The degree and type of disorder present in a system are not trivial to define or measure, and different paths can be made [4–6]. To begin with, one must compare the disordered system with the perfect crystal. In this sense, substitutional alloys present “the weakest type of disorder" [4] since it is possible, following a certain probability distribution, to occupy lattice sites with each atomic specie the alloy is formed of, with little disturbance of the crystal lattice. An alloy is labeled as *disordered* if the

substituted sites do not form a periodic lattice by themselves, in contrast to an *ordered* alloy in which two or more crystalline sublattices, each containing only one type of atom, can be defined [4].

The lattice's little-disturbance feature is frequently found in substitutionally disordered binary alloys, allowing the use of tweaked crystalline models as a starting point to tackle those systems. The first attempt to build such a model was the Virtual Crystal Approximation, VCA, in which the underlying crystalline structure is maintained and the lattice sites are occupied by "virtual" atoms whose properties, described by their respective potentials, are an average between those of the pure compounds [4, 7–9]. Regardless of being a crude approximation, VCA model has proven to accurately calculate properties in some semiconductors [10] and ferromagnets [11] but fails in the accurate description for semiconducting nitride systems [12, 13].

A better approach than the averaged local potentials from the VCA is the consideration of the local atomic properties through averaging the site scattering matrix (*t-matrix*) of each pure constituent; this approach is known as the Averaged *t*-matrix Approximation (ATA) [4, 14, 15]. Although the ATA represents an improvement over the VCA, it implicitly generates an "effective atom" when averaging the *t*-matrices, not considering explicitly the local atomic environment and incorrectly describing the electronic structure of some alloys for which an spurious band gap appears [4, 16, 17].

The next step in the description of the electrons [17] and phonons [18] in random substitutional alloys was taken with the Coherent Potential Approximation (CPA). In this approach the *t*-matrix method is applied to the alloy's constituents embedded in an effective potential placed on every lattice site. This effective potential is constructed in the spirit that the *local* atomic environment mimics that of the *macroscopic* real alloy, leading to a successful description for the electronic and phononic energy spectra due to its emphasis in long-range order [19], but failing in considering the atomic local environment around each type of atom [4, 20].

The use of the VCA, ATA, or CPA greatly simplifies the calculation of some alloy properties that do not depend importantly on the atomic local environment. If we wish to include in someway this short-range interactions into a binary alloy model structure containing N atoms, the number of possible different configurations that must be analyzed is 2^N, making the process computationally prohibiting even for the actual computational power. This calculation problem has given rise to two independent approaches: the first one consists of averaging several small structures that contain a tractable number of atoms, and the second one consists of constructing a single structure with sufficient number of atoms that can be considered as a *representative* structure of the bulk. In the idea of bringing a model that incorporates the best features of the two approaches, the Special Quasirandom Structures (SQS's) approach [21, 22] emerged as a solution to describe the properties of random alloys using the least possible number of atoms.

The SQS's are constructed by a selective occupation of N atomic sites "guided by the principle of close reproduction of the perfectly random network for the first coordination shells around a given site, deferring spurious atomic correlations to more distant neighbors" [22]. Thus, although the SQS's approach seek to include the atomic local environment of the alloy, they do so by explicitly comparing with its perfectly random-version, a hypothesis not always valid for some systems. Nevertheless, the SQS's approach has provided considerably good results in modeling metallic, semiconducting and high entropy alloys [23–26] through optimized algorithms [27, 28].

Thus when dealing with disordered alloys, the problem to solve is that of the correct short and long-range order description of the electronic and phononic energy states in the disordered system's model. In the spirit of improving the VCA, ATA, CPA, and SQS models, results of Part I of this work are a contribution to the study of alloys with the perspective that a simple and elegant approach to the simulation of these complex systems may arise in the future. Specifically, electronic and phononic specific heats and critical temperature are the analyzed properties through our simulation approaches for the study of alloys in Part I; the justifications for choosing gold-silver, copper-bismuth, and boron-nitrogen as testing alloy models are explained in Sections 1.1, 1.2, and 1.3 where it corresponds.

1.1 Specific Heat

Every physical system, being solid, liquid or gas, absorbs energy from its surroundings in different rates according to their internal degrees of freedom. In this sense, one useful quantity that relates the internal degrees of freedom with the energy needed to excite them, is the specific heat. Formally, the molar specific heat c is defined as an intensive magnitude that measures the required energy dE an N-particle system needs to rise its temperature dT:

$$c = \frac{1}{N}\frac{dE}{dT} \tag{1.1}$$

Specifically for solids, those degrees of freedom are distributed into two main contributions (see Section 2.3): from the electrons and from the nuclei. Since the lighter mass of the electrons make them extremely mobile in comparison to the heavier-mass nuclei, the energy absorption at low temperatures will be predominantly done by the more mobile and energetic valence electrons of the material, whereas at high temperatures it will be principally done by the oscillating nuclei. Thus, the tools needed to accurately probe the electrons and nuclei vibrations energy spectra distributions are rooted in the quantum theory of materials though the calculation of the electronic (eDoS or $N(E)$) and the vibrational (vDoS or $g(\omega)$) Density of States (see subsections 3.3.4 and 3.3.5).

Both the eDoS and vDoS, being a bridge between theoretical calculations and experimental measurements, are fundamental concepts to understand the physics of ordered and disordered materials. Focusing on the electronic properties of ordered solids, the free and the quasi-free electron theories as well as the Friedel's model for transition metals have been employed to study this kind of materials with tremendous success [2, 29–32]. However, as mentioned in the Introduction, the disorder present in the alloy introduces several complications that are not fully understood nor yet solved. Thereby, one must start from the simplest possible disordered system to study the effects disorder produces in it. One such system is the substitutionally disordered gold-silver alloy.

1.1.1 The Gold-Silver System

Gold and silver are two elements known as noble-metals due to their almost lack of reactivity in the bulk with other elements. According to the Hume-Rothery rules [33, 34], the similar characteristics between gold and silver, such as their metallic radii, crystalline structure, lattice parameter, and valence electron concentration per atom (see Table 1.1) [33], have the consequence that gold-silver alloys are metallic and can form a solid solution for all concentrations, thereby being a simple binary metallic system to analyze and take as a starting point to understand the more complex mechanisms that occur in other types of alloys [35–37]. Besides their similarities, it is important to mention that the differences between gold and silver make it possible to manufacture nanoporous gold through the chemical process known as dealloying [38–40], having multiple successful applications as a catalyst [41] or for biological sensors [42, 43].

TABLE 1.1. Some characteristics of atomic Ag and Au.
From: Gersten and Smith [34]

Element	Z	Electronic Configuration	Metallic Radius[a] $[\text{Å}]$	Density[b] $[\text{g/cm}^3]$	Melting Temperature $[\text{K}]$	Crystalline structure[b]	Lattice parameter[b] $[\text{Å}]$
Ag	47	$[\text{Kr}]\,4\text{d}^{10}5\text{s}^1$	1.45	10.51	1234.93	FCC	4.09
Au	79	$[\text{Xe}]\,4\text{f}^{14}5\text{d}^{10}6\text{s}^1$	1.44	19.29	1337.33	FCC	4.09

[a] Determined from the FCC structure.

[b] Values are given at room temperature.

Seeking to study the effect of disorder in the electronic states of gold-silver alloys, in 1966 Green and Valladares [35] measured their specific heat at low temperatures (between $2\,\mathrm{K}$ and $4\,\mathrm{K}$). It would be expected that the coefficient (γ) of the electronic contribution to specific heat ($c_{\mathrm{el}}= \gamma T$, see Section 2.3) changed linearly with the concentration of one specimen "either because of the effect of scattering or because the averaging of the potentials" [35] (recall the above discussion on CPA and VCA). However, they found a parabolic dependency, shown in Figure 1.1, a result later confirmed by Martin [44] in 1968 and by Davis and Rayne [45] in 1972.

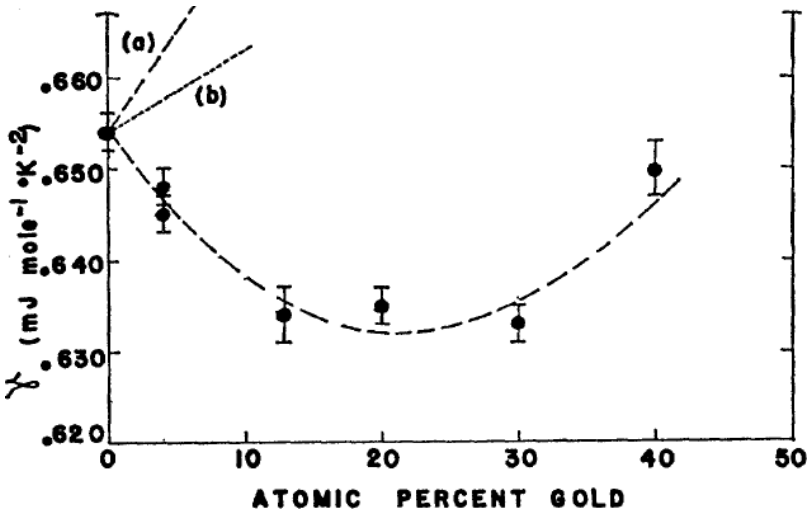

FIGURE 1.1. γ coefficient of the Electronic Specific Heat (c_{el}) for the $\mathrm{Au}_x\mathrm{Ag}_{100-x}$ alloy measured by Green and Valladares [35]. The predicted behavior due to scattering theory (broken (*a*) line) or the linear interpolation between the pure values (broken (b) line) does not agree with their parabolic adjustment (dashed line) to their measurements.

With the motivation of trying to explain these results, an *ab initio* study of the electronic structure of the $\mathrm{Au}_x\mathrm{Ag}_{100-x}$ system was carried out for the atomic gold concentrations $x = 0$, 4, 13, 20, 30, 40, 50, 75, 90, and 100 in order to determine the electronic specific heat coefficient γ through the eDoS at the Fermi level (see Section 2.3 for the explicit relation among them).

1.1.2 State of the art

Green and Valladares, 1966 [35].

As a collection of studies of the specific heat at low temperatures for different binary alloys [46–49], they studied the $\mathrm{Au}_x\mathrm{Ag}_{100-x}$alloy for gold concentrations $x = 0, 3.97, 12.90, 20.00, 30.00, 40.00$. An unexpected parabolic behavior as a function of gold concentration was found.

Stern, 1966 [50].

First attempt to explain the parabolic behavior of γ for this alloy. Stern considered the electron-impurity interaction and assumed that the electronic properties for the alloy can be determined from an average potential and then applied perturbation theory to a model which consists of a perfect lattice occupied by two different constituents randomly distributed.

Haga, 1967 [51].

Another attempt to explain the measurements of γ done by Green and Valladares. Haga considered the electron-phonon interactions in the alloy using perturbation theory while neglecting the electron-electron interaction. The calculation of the electronic properties of the alloy is assumed to be possible by the determination of an average potential that varies linearly from pure silver to pure gold (recall the VCA for alloys).

Martin, 1968 [44].

A second measure of γ for the concentrations $x = 0, 10.13, 25.57, 49.76, 100$. Martin suggested that the assumption that the electronic structure of the alloy can be determined from averaged potentials, a central hypothesis in the theories of Stern and Haga, may not be true.

Davis and Rayne, 1972 [45].

Measurements of electronic specific heat of the binary alloy, which were performed for the concentrations $x = 0, 10.0, 20.0, 30.0, 50.0, 75.0, 82.5, 90.0, 95.0, 100$, confirmed the previous results of Green and Valladares, and Martin. Their de Haas-van Alphen measurements on the dilute Ag-Au binary alloys suggest that the pure constituent averaged potential may not be justified, They also did the measurements for the Cu-Ag-Au alloy and extended the theories of Stern and Haga to the ternary system, maintaining their basic assumption of a perfect lattice with an averaged potential at each lattice point in the alloy (recall the VCA for alloys).

Kokko, Ojala, and Mansikka, 1989 [52].

A Linear Muffin-Tin Orbital (LMTO) calculation was performed to study the electronic structure of the ordered alloy which corresponds to gold concentrations of: $x = 0, 25, 33.3, 50, 66.7, 75, 100$, finding a nonlinear behavior with a minimum value for γ around 25 at% gold and qualitatively similar to those measured by Green and Valladares, Martin, Davis and Rayne. Although they are aware that *real* Ag-Au alloys are disordered structures, they believe that "it is possible to explain many phenomena, at least qualitatively, in real Ag-Au alloys by investigating these kinds of model systems because the [electronic] DOS is a rather smooth function of energy around the Fermi level and disorder smearing should not appreciably affect the results".

1.2 Superconductivity in bismuth-based materials

Superconductivity is a quantum-originated phenomena that can be macroscopically observed in some materials below certain critical temperature T_c and magnetic field H_c; the two principal measurable physical characteristics being the disappearance of the material's electrical resistance and the manifestation of the Meissner-Ochsenfeld effect, i.e. the total or partial expulsion of the magnetic flux density from the bulk of the material when placed inside a magnetic field lower than H_c) [34, 53]. Since their discovery in 1911 [54], superconductors have attracted attention from both theorists and experimental scientists, leading to a classification of Type I and Type II superconductors according to their response to temperature and external magnetic fields [2, 34, 53]

Along with new discoveries of superconducting materials, several theories trying to explain this phenomenon emerged, being the one by J. Bardeen, L. N. Cooper, and J. R. Schrieffer (BCS) [55] the first successful microscopic theory for superconductivity. Among several other features, BCS theory accurately relates the material's T_c to its electronic and phononic intrinsic properties [34, 53]. The majority of pure metals and some alloys [56–59] are correctly described by the BCS theory and therefore are given the surname of *conventional superconductors*.

Focusing on elemental bismuth, it is one of the few elements that maintains its superconducting properties under varied circumstances at atmospheric pressure, whether in the amorphous phase with a measured T_c of $\approx 6\,\mathrm{K}$ [60–62], or in the crystalline phase with a T_c predicted by our group to be below $1.3\,\mathrm{mK}$ [63], later confirmed to be $0.53\,\mathrm{mK}$ [64]. Moreover, three high-pressure crystalline phases are also superconducting [65]: Bi-II with $T_c = 3.9\,\mathrm{K}$, Bi-III with $T_c = 7\,\mathrm{K}$, and Bi-V with $T_c = 8\,\mathrm{K}$. An in-depth study of superconductivity in pure bismuth has also been carried out and the results are presented in Part II of this thesis.

With respect to the alloyed forms of bismuth, it is known that it forms superconducting compounds with almost every element in the periodic table (excepting those of the halogen and noble-gas groups), having superconducting critical temperatures ranging from $0.3\,\mathrm{K}$ for Bi_3Mo to $5.7\,\mathrm{K}$ for BiRu [66]. An interesting feature of bismuth binary alloys is that they rarely form solid solutions, having a tendency for segregation of the constituents and needing high-pressure-synthesis processes to be formed in metastable crystalline structures [67, 68].

1.2.1 The Copper-Bismuth System

The Cu-Bi system is one example of a bismuth alloy that does not make a solid solution for any concentration, presenting instead segregation of copper and bismuth [67–69]. Published studies [66, 69] have reported this alloy having an amorphous structure which is superconducting with T_cs ranging

from $1\,\mathrm{K}$ to $6\,\mathrm{K}$ depending on the composition. It is worth noting that the critical temperature for pure amorphous bismuth is close to $6\,\mathrm{K}$ [60–62]. On the other side, in 2017 it was possible to synthesize two crystalline structures of copper-bismuth by means of high-pressure processes: $Cu_{61}Bi_{39}$ [67] and $Cu_{50}Bi_{50}$ [68], both being superconductors with T_cs of $1.36\,\mathrm{K}$ and $1.3\,\mathrm{K}$, respectively.

Our interest in determining the effects of structural disorder on the T_c for the copper-bismuth system, led us to calculate the electronic and phononic energy spectra for the reported 39-at%Bi crystalline structure (x-$Cu_{61}Bi_{39}$) and compare them to those of our model for the amorphous structure with the same concentration (a-$Cu_{61}Bi_{39}$).

1.2.2 State of the art

Alekseevskii, Bondar, and Polukarov, 1960 [69].

They reported the first measurement of superconductivity in unannealed Cu-Bi alloys for ≈ 20 at.% Cu, finding a T_c around $2\,\mathrm{K}$. Annealing their samples at $120\,\mathrm{C}$ causes phase decomposition and dissapearing of superconductivity, whereas annealing them at $80\,\mathrm{C}$ does not produce a drop in the resistance measurements; concluding from these data that the amorphous phase is the one that can maintain a superconducting state.

Matthias *et al.*, 1966 [66].

They studied several bismuth alloys with transition metals and reported general features of superconductivity in those systems, without determining the crystal structure (if any) or the precise atomic compositions. For the case of CuBi, a T_c around $1.4\,\mathrm{K}$ was measured and hypothesized the possibility of determining the structure of the metastable phase through the x-ray data. The also reported the lost of the superconducting signal after annealing their sample at $200\,\mathrm{C}$.

Averback *et al.*, 1985 [70].

They demonstrated that low-temperature ion-beam mixing in copper-bismuth bilayered samples produces an amorphous phase that seems very similar to the Bi phase obtained by vapor quenching of pure Bi onto cold ($4.2\,\mathrm{K}$) substrates. Incidentally, they found that "irradiation of pure bismuth does not appear to produce an amorphous phase whereas vapor quenching does". Since the amorphous alloyed samples begin to recrystallize at $150\,\mathrm{K}$, which is a higher crystallization temperature than that for pure bismuth ($10\,\mathrm{K}$ to $20\,\mathrm{K}$), they conclude that impurities are necessary to retard recrystallization in amorphous Bi. The measured T_c is around $5\,\mathrm{K}$ to $6\,\mathrm{K}$ depending on deposition conditions, and these critical temperatures significantly decrease after annealing the samples at $\approx 150\,\mathrm{K}$. After annealing at $330\,\mathrm{K}$, no indication of superconductivity was detected upon cooling to $\approx 1\,\mathrm{K}$.

Clarke *et al.*, 2016 [71].

They synthesized the first crystalline alloy for the Cu-Bi system (39 at% Bi) through high-pressure processes. This material is metastable at ambient pressure and temperature, and has a measured superconducting critical temperature of $1.36\,\mathrm{K}$. They also calculated a value of $1.4\,\mathrm{K}$ for the T_c using the Allan-Dynes modified McMillan's approximation of the Eliashberg equation.

1.3 Amorphous semiconductors

1.3.1 The Boron Nitride System

When boron and nitrogen are mixed in an equiatomic concentration $B_{50}N_{50}$, or simply BN, is formed. Due to the electronic configurations of boron ($[\mathrm{He}]\,2s^2 2p^1$) and nitrogen ($[\mathrm{He}]\,2s^2 2p^3$), BN is isoelectronic to carbon and from this fact it is possible for BN to crystallize in structures analogous to those of carbon, namely: two-dimensional low-density and three-dimensional high-density structures. Specifically, the two-dimensional layered structures of BN are: the hexagonal structure (h-BN) shown in Figures 1.2, and the rhombohedral structure (r-BN) shown in Figures 1.3; whereas the three-dimensional structures are the wurtzite structure (w-BN) shown in Figures 1.4 and the cubic zincblende structure (c-BN) shown in Figure 1.5.

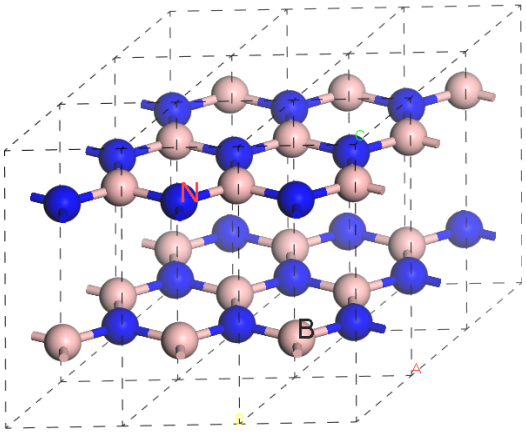

(A) Two different monolayers, stacked one above the other, are shown. N atoms in the top layer are located above B atoms in the bottom layer and *vice versa*.

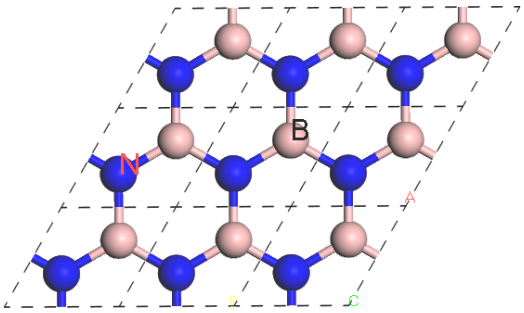

(B) Top view of the h-BN structure of Fig. 1.2a. The depicted hexagons lie on the same plane and the coordination number for each B and N is three.

FIGURE 1.2. Two views for the sphere-and-stick representation for the structure of hexagonal boron nitride, h-BN. Pink spheres are boron atoms and blue spheres are nitrogen atoms. The unit cell, delimited by dashed lines, is replicated $3 \times 3 \times 1$ times along the cell axes.

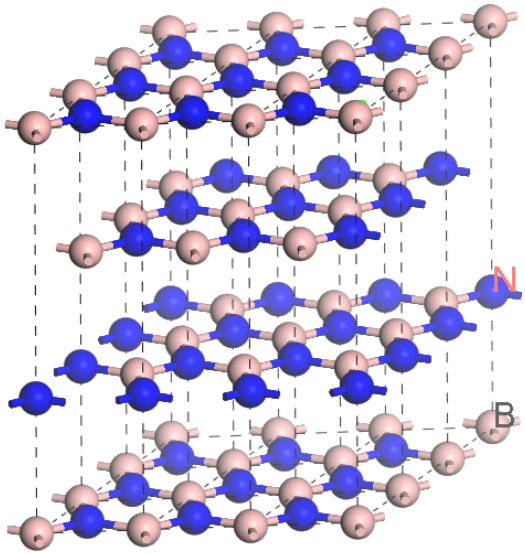

(A) $3 \times 3 \times 1$ replica of the unit cell for r-BN. Three different monolayers are shown.

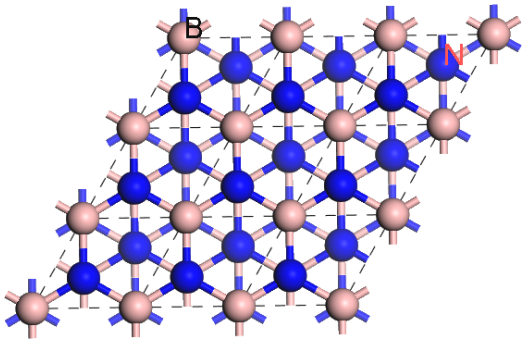

(B) Top view of the r-BN structure. The formed hexagons lie on a plane and the coordination number for each B and N is three.

FIGURE 1.3. Sphere and stick representation of the structure of rhombohedral boron nitride (r-BN). Pink spheres are boron atoms and blue spheres are nitrogen atoms.

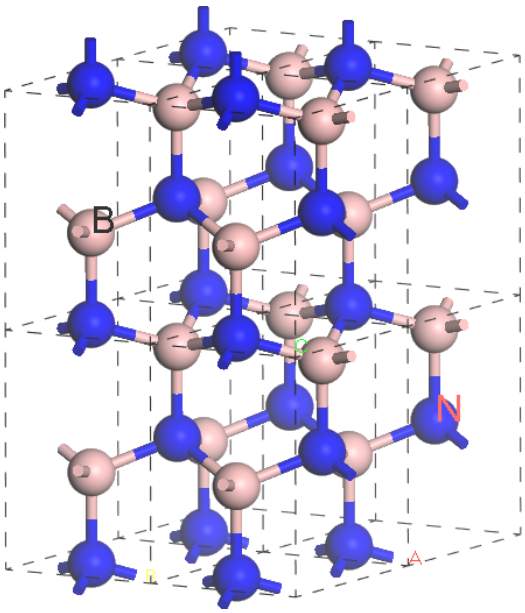

(A) $2 \times 2 \times 2$ unit cell repetition.

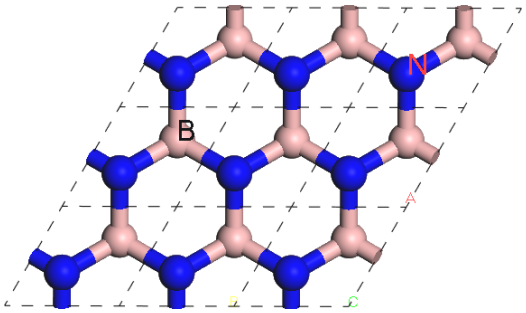

(B) Top view of the w-BN structure from a unit cell repeated 3×3 times. The hexagonal structure does not lie on a plane and the coordination number for each atom is four.

FIGURE 1.4. Sphere and stick representation of the structure of boron nitride in its wurtzite structure (w-BN). Pink spheres are boron atoms and blue spheres are nitrogen atoms.

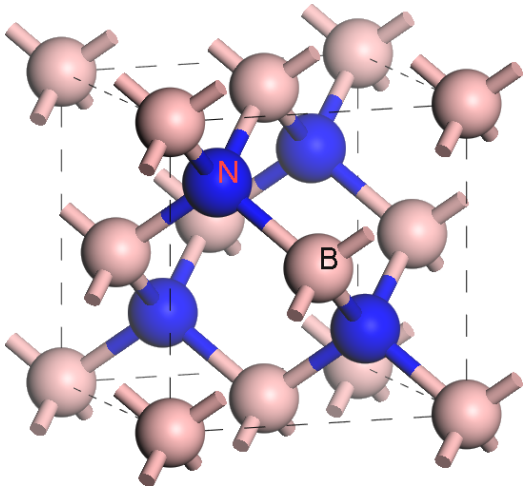

FIGURE 1.5. c-BN structure. The coordination number for each atom is four, leading to a diamond-like structure.

Continuing with the carbon analogy, h-BN (Figs. 1.2) and c-BN (Fig. 1.5) are expected to have physical properties analogous to graphite and diamond, respectively, this is why the first phase diagrams for BN [72] reported h-BN as the stable phase at ambient pressure and temperature conditions. However, later investigations [73, 74] reported c-BN as the stable phase. This dilemma has prevailed over the years but it has not stopped the experimental and theoretical research for these two modifications of BN, since it is a promising material for industrial applications [75–80].

With respect to the amorphous BN, a-BN, not much has been experimentally explored. The first attempts, back in 1968, reported vitreous films reminiscent of disordered materials [81–83]. Only recently, some papers analyzed the possible use of amorphous BN as an ultralow-dielectric-constant material which can be used as dielectric diffusion barriers in low-scale electronics [78, 84, 85]. Moreover, a-BN has been used as a precursor material to synthesize one crystalline BN modification [86–88].

In the context of practical applications, it is necessary to study the relation between the macroscopic properties and the hybridization of the electronic states so that BN can be effectively employed as the promising material it is claimed to be. So, several theoretical simulations have centered on studying the electronic structure of crystalline, amorphous and liquid BN [89–92]. Nevertheless, the lattice vibrational problem has not received much of attention either theoretical or experimental.

1.3.2 State of the art

Rand and Roberts, 1968 [81].

They produced vitreous films of boron nitride up to $6000\,\text{Å}$ thick by chemical vapour deposition (CVD) and performed a complete physico-chemical characterization of their samples. Among other features, they reported observation of crystallites near the surface of the film with estimated sizes from $1000\,\text{Å}$ to $6000\,\text{Å}$, depending on the deposition temperature ($600\,\text{C}$ to $950\,\text{C}$). Also, they estimated a band gap of $3.8\,\text{eV}$ and measured a dielectric constant κ of 3.7 for a $800\,\text{Å}$-$1800\,\text{Å}$ film.

Hirayama and Shohno, 1975 [82].

They studied amorphous and polycrystalline boron nitride films deposited on Si substrates. The polycrystalline films, having hexagonal structure, were obtained at temperatures near $1000\,^\circ\text{C}$, maintaining stable up to temperatures of $1250\,^\circ\text{C}$ in a hydrogen and nitrogen atmosphere. The amorphous films were produced when deposited below $1000\,^\circ\text{C}$ and are unstable and decomposed after a heat treatment in nitrogen and hydrogen atmospheres.

Arya and D'Amico, 1988 [83].

They reviewed the collected experimental data concerning boron nitride thin films to look for better experimental techniques to obtain them. They concluded that "the structure of BN thin films is amorphous or polycrystalline (hexagonal or cubic)) depending on the experimental technique" and reported that the density for BN films ranges from $1.7\,\text{g}\,\text{cm}^{-3}$ to $2.1\,\text{g}\,\text{cm}^{-3}$.

Zedlitz, Heintze, and Schubert, 1996 [93].

They prepared boron nitride thin films, measuring a band gap of $5\,\text{eV}$ and determining that the amorphous phase consists almost entirely of sp^2 bonding. However, the formation of a crystalline phase in some samples, with sp^3 bonding, was also observed.

Sekkal *et al.*, 1998 [89].

They employed classical molecular dynamics within the NVT ensemble to investigate the thermal expansion coefficient and heat capacity of c-BN, simulating 216 atoms interacting via the Tersoff potential. Also, they studied structural features of liquid BN at various densities.

McCulloch, McKenzie, and Goringe, 2000 [90].

They performed plane-wave *ab initio* calculations to study structural and elastic properties for BN, AlN, and AlBN_2 amorphous alloys by means of the *liquid quench* method. They simulated BN at two

densities ($2\,\mathrm{g\,cm^{-3}}$ and $3\,\mathrm{g\,cm^{-3}}$) using a 64-atom model, predicting that tetrahedral bonding (sp^3) of amorphous BN does not form under the *liquid quench* method.

Durandurdu, 2016 [91].

He studied, by means of *ab initio* calculations, the hexagonal-to-wurtzite and amorphous-to-amorphous pressure-induced phase transformation of BN. He proposed that a-BN might be a candidate to be a precursor to synthesize an intermediate structure from h-BN to w-BN.

Durandurdu, 2020 [92].

He generated a tetrahedrally coordinated amorphous BN sample by *ab initio* calculations and reported its mechanical and electrical properties, finding a it can serve as a hard material with a band gap of $2.0\,\mathrm{eV}$.

This page intentionally left blank

2 Theoretical Framework

The theoretical framework which supports the calculations and results reported in Part I is explained in this chapter. First, Hohenberg and Kohn's Density Functional Theory (DFT) formulation and Kohn and Sham's approach for the problem are described in Section 2.1. Also, the application of the DFT framework on the description of nuclei dynamics at finite temperatures and the implementation of DFT into the DMol^3 code is discussed within this section. Then, a description of the pair correlation functions employed in Part I of this thesis is presented in Section 2.2. Finally, the calculated properties for the reported systems in Part I (namely, the electronic specific heat (Section 2.3), the lattice-vibrations' contributions to some thermodynamics quantities (Section 2.4), and the BCS theory of superconductivity (Section 2.5)), are briefly discussed. The contents in Sections 2.1 and 2.5 are also employed in Part II of this thesis.

2.1 Density Functional Theory

The physical description of materials using quantum-mechanical calculations is known as a first-principles or *ab initio* approach, in which the many-body hamiltonian $\hat{H}$ for $i = 1, \ldots, N$ electrons of mass m located at $\boldsymbol{r}_i$, and $I = 1, \ldots, M$ nuclei of mass M_I and charge Z_I located at $\boldsymbol{R}_I$, is given by:

$$\begin{aligned}\hat{H} = &-\sum_i \frac{\hbar^2}{2m}\nabla_i^2 - \sum_{i,I} k\frac{Z_I e^2}{|\boldsymbol{r}_i - \boldsymbol{R}_I|} + \frac{1}{2}\sum_{i\neq j} k\frac{e^2}{|\boldsymbol{r}_i - \boldsymbol{r}_j|} \\ &-\sum_I \frac{\hbar^2}{2M_I}\nabla_I^2 + \frac{1}{2}\sum_{I\neq J} k\frac{Z_I Z_J e^2}{|\boldsymbol{R}_I - \boldsymbol{R}_J|},\end{aligned} \tag{2.1}$$

where $k = 1/(4\pi\epsilon_0)$, is employed to solve the time-independent Schrödinger equation:

$$\hat{H}\Psi_j(\{\boldsymbol{r}\};\{\boldsymbol{R}\}) = E_j\Psi_j(\{\boldsymbol{r}\};\{\boldsymbol{R}\}), \tag{2.2}$$

for the many-body wavefunction that describes the state j of the system:

$$\Psi_j(\{\boldsymbol{r}\};\{\boldsymbol{R}\}) = \Psi_j(\boldsymbol{r}_1, \cdots, \boldsymbol{r}_N; \boldsymbol{R}_1, \cdots, \boldsymbol{R}_M) \tag{2.3}$$

In particular, the ground-state wavefunction is labeled with $j = 0$: $\Psi_0(\{\boldsymbol{r}\}\,;\{\boldsymbol{R}\})$.

The importance of finding the solution of the Schrödinger equation (2.2) relies on the fact that by knowing the full wavefunction (2.3) one can understand from first-principles the macroscopic properties of materials such as electronic, thermodynamic, optical, and transport phenomena. Also, these calculations serve as a basis to the construction of interatomic potentials which can be used to efficiently perform simulations on large complex systems. However, since the number of variables for the wavefunction (2.3) ranges up to the order of 10^{23} for condensed systems, the task to find it becomes nowadays impossible since the computing power needed exceeds the most powerful supercomputer.

In order to circumvent the problem of the explicit determination of the $3(N+M)$-variable wavefunction (eq. (2.3)) while keeping the accurate and predictive power of Schrödinger equation (eq. (2.2)), a theory which relies on the 3-variable ground-state electronic density function:

$$n_0(\boldsymbol{r}) = N \int |\Psi_0(\boldsymbol{r}, \boldsymbol{r}_2, \cdots, \boldsymbol{r}_N; \boldsymbol{R}_1, \cdots, \boldsymbol{R}_M)|^2 d\boldsymbol{r}_2 \cdots d\boldsymbol{r}_N d\boldsymbol{R}_1 \cdots d\boldsymbol{R}_M, \tag{2.4}$$

has been the method of choice to find material's properties from an *ab initio* approach. This theory, known as Density Functional Theory (DFT), postulates that any property of a system of interacting particles is determined from a functional of the ground-state density function n_0, and is based in two theorems postulated and proved by Hohenberg and Kohn in 1964 [94]. Following Martin [96], the two theorems are stated next:

- **Theorem I.** For any system of interacting particles in an external potential $V_{\text{ext}}(\boldsymbol{r})$, the potential $V_{\text{ext}}(\boldsymbol{r})$ is determined uniquely, except for a constant, by the ground state particle density $n_0(\boldsymbol{r})$.
- **Theorem II.** A universal functional for the energy $E[n]$ in terms of the density $n_0(\boldsymbol{r})$ can be defined, valid for any external potential $V_{\text{ext}}(\boldsymbol{r})$. For any particular $V_{\text{ext}}(\boldsymbol{r})$ the exact ground state energy of the system is the global minimum value of this functional, and the density $n(\boldsymbol{r})$ that minimizes the functional is the exact ground state density $n_0(\boldsymbol{r})$.

The schematic representation of the first theorem is depicted in Figure 2.1 where single arrows ($\Rightarrow$) represent the solution of the many-body Schrödinger equation within the Born-Oppenheimer approximation [2, 97] (dropping out the explicit dependence on the set $\{\boldsymbol{R}\}$ of nuclei coordinates). Starting from the external potential $V_{\text{ext}}(\boldsymbol{r})$ that acts upon the electrons, the eigenfunctions $\Psi_j(\{\boldsymbol{r}\})$ for the system's j state are in principle obtained by solving the Schrödinger equation (2.2) (a task impossible to do in practice); in particular, from the ground-state solution $\Psi_0(\{\boldsymbol{r}\})$, $n_0(\boldsymbol{r})$ is constructed. The Hohenberg-Kohn's Theorem I (indicated as $\overset{\text{H-K}}{\Longleftrightarrow}$ in Fig. 2.1) guarantee the relation between $V_{\text{ext}}(\boldsymbol{r})$ and $n_0(\boldsymbol{r})$.

$$\begin{array}{ccc} V_{\text{ext}}(\boldsymbol{r}) & \overset{\text{H-K}}{\Longleftrightarrow} & n_0(\boldsymbol{r}) \\ \Downarrow & & \Uparrow \\ \Psi_j(\{\boldsymbol{r}\}) & \Rightarrow & \Psi_0(\{\boldsymbol{r}\}) \end{array}$$

FIGURE 2.1. Scheme for the Hohenberg and Kohn Theorem I. From the external potential for the interacting electrons $V_{\text{ext}}(\boldsymbol{r})$, the set $\Psi_j(\{\boldsymbol{r}\})$ correspond to the eigenfunctions of the Schrödinger equation, impossible to obtain by practical means. The ground-state density $n_0(\boldsymbol{r})$ is constructed from the ground-state wavefunction of the system $\Psi_0(\{\boldsymbol{r}\})$. The relation between $V_{\text{ext}}(\boldsymbol{r})$ and $n_0(\boldsymbol{r})$ is supported by Theorem I. Adapted from Martin [96].

Although very powerful, Hohenberg and Kohn formulation of DFT as an exact theory of many-body particles does not provide an explicit expression for the functional of the density needed to determine the properties of interest. However, the 1965 approach of Kohn and Sham [95, 98] to DFT revolutionized its application to diverse systems with remarkable success, currently making DFT the principal method for calculating the electronic structure of materials.

Loosely outlined and depicted in Figure 2.2, the Kohn-Sham approach reformulates the DFT problem of finding the ground state density by assuming that $n_0(\boldsymbol{r})$ for the interacting system, described by the many-body wavefunction $\Psi_0(\{\boldsymbol{r}\})$, is equivalent to the density produced by the N lowest-energy occupied single-particle states: $\psi_{i=1,N}(\boldsymbol{r})$. These lowest-energy wavefunctions are chosen from the set of wavefunctions $\psi_i(\boldsymbol{r})$ which is the solution to Schrödinger-like equations for some non-interacting system described by the potential $V_{\text{KS}}(\boldsymbol{r})$.

$$\begin{array}{ccccccc} V_{\text{ext}}(\boldsymbol{r}) & \overset{\text{H-K}}{\Longleftrightarrow} & n_0(\boldsymbol{r}) & \overset{\text{K-S}}{\Longleftrightarrow} & n_0(\boldsymbol{r}) & \overset{\text{H-K}_0}{\Longleftrightarrow} & V_{\text{KS}}(\boldsymbol{r}) \\ \Downarrow & & \Uparrow & & \Uparrow & & \Downarrow \\ \Psi_j(\{\boldsymbol{r}\}) & \Rightarrow & \Psi_0(\{\boldsymbol{r}\}) & & \psi_{i=1,N}(\boldsymbol{r}) & \Leftarrow & \psi_i(\boldsymbol{r}) \end{array}$$

FIGURE 2.2. Schematic representation of the Kohn and Sham approach. The Hohenberg-Kohn theorem (see Fig. 2.1) applied to an interacting system of particles is depicted at the left side of the K-S arrow ($\overset{\text{K-S}}{\Longleftrightarrow}$), whereas its application to a non-interacting system described by an effective potential $V_{\text{KS}}(\boldsymbol{r})$ (eq. (2.11)) is depicted at the right side (notice the notation H-K_0). The Kohn-Sham approach postulates that $n_0(\boldsymbol{r})$ of the system can be obtained from the independent-particle wavefunctions ψ_i obtained from Schrödinger-like single-particle equations (eq. (2.8)). Adapted from Martin [96]

Specifically, in the Kohn-Sham approach the energy functional $E[n]$ stated in Hohenberg-Kohn's Theorem II is expressed as [96, 99]:

$$E_{\text{KS}}[n] = \overbrace{\underbrace{T_s[n]}_{\text{Kinetic energy}} + \underbrace{\int \mathrm{d}\boldsymbol{r} V_{\text{ext}}(\boldsymbol{r}) n(\boldsymbol{r})}_{\text{External potential energy}} + \underbrace{\frac{1}{2}\iint \mathrm{d}\boldsymbol{r}\mathrm{d}\boldsymbol{r'} \frac{n(\boldsymbol{r})n(\boldsymbol{r'})}{|\boldsymbol{r}-\boldsymbol{r'}|}}_{\text{Hartree energy}}}^{\text{Energy in the non-correlated-particle scheme}} + \underbrace{E_{\text{XC}}[n]}_{\text{XC energy}}. \tag{2.5}$$

The first three terms describe the total energy in the non-correlated-particle scheme whereas the difficult-to-calculate many-body interactions are incorporated into the *exchange-correlation* energy functional: $E_{\text{XC}}[n]$.

Also following Hohenberg-Kohn's Theorem II, the density $n(\boldsymbol{r})$ that yields the ground-state energy of the system and consequently the minimum value of the Kohn-Sham functional (eq. (2.5)) is the ground-state density. Thus, the functional derivative of $E_{\text{KS}}[n]$ must vanish for $n_0(\boldsymbol{r})$:

$$\left.\frac{\delta E_{\text{KS}}}{\delta n}\right|_{n_0} = 0. \tag{2.6}$$

Then, from equations (2.5) and (2.6), and requiring that the single-particle wavefunctions $\psi_i(\boldsymbol{r})$ be orthonormal:

$$\int \mathrm{d}\boldsymbol{r} \psi_i^*(\boldsymbol{r})\psi_j(\boldsymbol{r}) = \delta_{ij}, \tag{2.7}$$

the celebrated *Kohn-Sham equations* [95, 96, 98] are obtained:

$$\hat{H}_{\text{KS}}\, \psi_i(\boldsymbol{r}) = \varepsilon_i \psi_i(\boldsymbol{r}). \tag{2.8}$$

These are a set of Schrödinger-like equations for the single-particle eigenfunctions $\psi_i(\boldsymbol{r})$ of a non-interacting system described by the Kohn-Sham hamiltonian $\hat{H}_{\text{KS}}$:

$$\hat{H}_{\text{KS}} = -\frac{\hbar^2}{2m}\nabla^2 + V_{\text{KS}}(\boldsymbol{r}) \tag{2.9}$$

and where the ground-state electronic density was postulated by Kohn-Sham to be calculated through the N lowest-energy occupied states (recall Fig. 2.2):

$$n_0(\boldsymbol{r}) = \sum_{i=1}^{N} |\psi_i(\boldsymbol{r})|^2 \tag{2.10}$$

In equation (2.9), the Kohn-Sham potential $V_{\text{KS}}(\boldsymbol{r})$ is defined as:

$$V_{\text{KS}}(\boldsymbol{r}) = V_{\text{ext}}(\boldsymbol{r}) + V_{\text{H}}(\boldsymbol{r}) + V_{\text{XC}}(\boldsymbol{r}), \tag{2.11}$$

where $V_{\text{ext}}(\boldsymbol{r})$ is the external potential produced by the fixed-position nuclei:

$$V_{\text{ext}}(\boldsymbol{r}) = -\sum_I k\frac{Z_I e^2}{|\boldsymbol{r} - \boldsymbol{R}_I|}, \tag{2.12}$$

$V_{\text{H}}(\boldsymbol{r})$ is the potential produced by the electronic density $n(\boldsymbol{r})$ and is known as the Hartree potential:

$$V_{\text{H}}(\boldsymbol{r}) = \int \mathrm{d}\boldsymbol{r'}\frac{n(\boldsymbol{r'})}{|\boldsymbol{r} - \boldsymbol{r'}|}, \tag{2.13}$$

and $V_{\text{XC}}(\boldsymbol{r})$, known as the exchange-correlation potential, is derived from the exchange-correlation energy of equation (2.5) as:

$$V_{\text{XC}}(\boldsymbol{r}) = \frac{\delta E_{\text{XC}}}{\delta n(\boldsymbol{r})}. \tag{2.14}$$

So far, two issues have emerged in the Kohn-Sham approach:

1. To calculate $V_{\text{H}}(\boldsymbol{r})$, the knowledge of $n(\boldsymbol{r})$ is needed (see eq. (2.13)). However, the Kohn-Sham equations which depend on $V_{\text{H}}(\boldsymbol{r})$, must be solved to determine $\psi_i(\boldsymbol{r})$ and consequently $n(\boldsymbol{r})$ (see eqs. (2.8) and (2.10)); thus involving a circular argument.

2. The many-body interactions collected in E_{XC} (eq. (2.5)) are still needed to solve Kohn-Sham equations (see eqs. (2.8), (2.9), (2.11), and (2.14)). However, the Kohn-Sham approach does not provide an explicit expression for it nor a manner to find it.

To solve issue 1, a self-consistent calculation is performed [96, 99]. Here, an initial guess for $n_0(\boldsymbol{r})$ is made through skillfully chosen $\psi_i(\boldsymbol{r})$ into what is known as the *basis set*, and its types include localized atomic-like or extended plane-wave functions [96]. Then, from the chosen basis set, $V_{\text{KS}}(\boldsymbol{r})$ (eq. (2.11)) is calculated and the Kohn-Sham equations (eqs. (2.8)) are solved to find a new set of functions $\psi_i(\boldsymbol{r})$ that yield a new electron density $n_0^{\text{new}}(\boldsymbol{r})$. If $n_0^{\text{new}}(\boldsymbol{r})$ is equal to the initial guess, the self-consistent cycle stops and properties such as total energy, forces, and eigenvalues can be calculated from it. If it is not equal, a mixing scheme for the two densities is applied, generating a *mixed* density that is used as a new guess and the cycle is repeated until convergence is achieved and calculation of properties can be done. By far, this cyclical calculations are the most time-consuming process when implementing DFT into computational codes.

The solution for issue 2 is more complicated and is one of the major research topics in the development and the implementation of DFT. Since the explicit form of E_{XC} is not known, it is useful to express it in the form [96]:

$$E_{\mathrm{XC}}\left[n\right] = \int \mathrm{d}\boldsymbol{r}\; n(\boldsymbol{r})\epsilon_{\mathrm{XC}}([n]\,,\boldsymbol{r}) \tag{2.15}$$

where $\epsilon_{\mathrm{XC}}([n]\,,\boldsymbol{r})$ is an exchange-correlation energy density per electron at point $\boldsymbol{r}$ that depends on the density n at some neighborhood of point $\boldsymbol{r}$ and for which several approximations have arisen with remarkable success; two of the most relevant being the Local Density Approximation (LDA) and the Generalized-Gradient Approximation (GGA) [96, 99–101].

In the LDA, a *homogeneous electron gas*, in which the nuclei are replaced by a uniform positively charged background, is taken as a model to produce a calculation for $\epsilon_{\mathrm{XC}}([n]\,,\boldsymbol{r})$ of eq. (2.15) that solely depends on n:

$$E_{\mathrm{XC}}^{\mathrm{LDA}}\left[n\right] = \int \mathrm{d}\boldsymbol{r}\; n(\boldsymbol{r})\;\epsilon_{\mathrm{XC}}^{\mathrm{LDA}}(n(\boldsymbol{r})), \tag{2.16}$$

whereas in the GGA, $\epsilon_{\mathrm{XC}}([n]\,,\boldsymbol{r})$ of eq. (2.15) depends on n and on the magnitude of the gradients of the density $|\nabla n|$:

$$E_{\mathrm{XC}}^{\mathrm{GGA}}\left[n\right] = \int \mathrm{d}\boldsymbol{r}\; n(\boldsymbol{r})\;\epsilon_{\mathrm{XC}}^{\mathrm{GGA}}(n(\boldsymbol{r}),|\nabla n|). \tag{2.17}$$

Several different parametrizations for $\epsilon_{\mathrm{XC}}^{\mathrm{LDA}}$ and $\epsilon_{\mathrm{XC}}^{\mathrm{GGA}}$ have led to successful applications of DFT to a wide range of insulating, semiconducting, and metallic materials, whether pure or alloyed [99, 100]. And when the LDA or GGA have failed in correctly describing the electronic structure of a particular material, more complex approximations to $E_{\mathrm{XC}}\left[n\right]$ such as meta-GGA, hybrid, or non-local functionals have appeared to improve the calculation's accuracy [96, 101]. However, it is important to be aware that there exists a broad class of materials for which their strongly-correlated electrons are not yet well described by DFT, requiring to go beyond the independent-particle scheme [102].

Pseudopotentials

Recalling the above discussion about the self-consistent calculation within the Kohn-Sham approach, it was stated that one must guess an initial density through some chosen basis set of functions $\psi_i(\boldsymbol{r})$ in order to solve equations (2.8). In principle, one must include wavefunctions for all the electrons of each atom to obtain a good initial guess; nevertheless, for must purposes the outermost *valence* electrons are solely responsible for the interactions among atoms, thereby not requiring to explicitly include the innermost *core* electronic states into the calculations. However, if the core electronic states are simply ignored, the valence electronic states would not be correctly described since valence

wavefunctions heavy oscillate near the atomic nucleus due to the orthogonality requirement for the eigenfunctions of the atomic hamiltonian.

The solution to this problem is brought by the construction of a pseudo-wavefunction that, given certain radial cutoff r_c from the nucleus, identically behaves as the real valence state for $r > r_c$ and is a smooth and nodeless function that yields the same electronic density of the real valence wavefunction for $r < r_c$. The procedure to construct the pseudo-wavefunctions is done by replacing the true nuclear and core-electrons potential for an effective interaction, known as pseudopotential, which is defined up to a specific radial cutoff and acts on the valence electrons yielding the correct electronic density for the atom [96].

The usefulness of the pseudopotential cannot be overemphasized. Since it effectively represent the core electronic states, the pseudopotential can readily be employed for the description of the atomic core electronic density when the atom is placed under any environment, property known as *transferability*. Moreover, the relativistic effects that some heavy-element's core electrons experience can be included in the pseudopotential, giving an accurate description of the full electronic density [96, 99].

Ab initio Molecular Dynamics (AIMD)

Molecular Dynamics (MD) is a well known classical simulation method for describing the movement of particles subjected to external forces through the solution of Newton's equations of motion [103]. In this sense, the adequate election for the timestep of the simulation is of great relevance for the success of the simulation. The MD extension to the quantum regime was done by Car and Parrinello [104]. In this method, the external forces responsible to move the ions are determined by the on-the-fly calculated ground-state electronic density by means of a DFT calculation [96, 99, 105], giving rise to the method known as *Ab initio* Molecular Dynamics (AIMD), which nowadays is a very important tool to study complex molecules, solids, and liquids at temperatures and pressures not easily achievable due to laboratory physical conditions.

When performing MD simulations, several ensembles may be employed according to the specific situation we need to describe [96, 103, 106–108]. Two of the most common are: the microcanonical ensemble (NVE), in which the total energy E, the volume of the system V, and the number of particles N remain constant throughout the whole simulation; and the canonical ensemble (NVT) in which V, N, and the temperature T are the constants of the simulation. When performing MD simulations within the NVT ensemble, a method to control the desired temperature is needed [103, 105]. This method was devised by Nosé [109, 110] and Hoover [111] by means of an extended Lagrangian function [103, 105].

DMol^3. Materials Studio *ab initio code*

DMol^3 [112–115], is an *ab initio* code developed by B. Delley and is included in the Dassault Systèmes BIOVIA - Materials Studio suite of codes. In this code, the basis functions are the independent-electron wavefunctions $\psi_i(\boldsymbol{r})$ which are numerically calculated for each atom-centered orbital. Nevertheless the code includes LDA, GGA, and meta-GGA exchange-correlation functionals, in the present work two of the most common will be used: the Vosko, Wilk, and Nusair [116] (VWN) LDA functional and the Perdew, Burke, and Ernzerhof [117] (PBE) GGA functional. Relativistic corrections for the core electronic states [118] are also included through the pseudopotentials *vpsr* [119] and *dspp* [120].

Ab initio MD calculations are readily done within the NVE and the NVT ensembles. For the latter, the temperature control can be made by a single Nosé-Hoover thermostat with the possibility of performing heating and cooling ramps of several simulation steps.

2.2 Correlation Functions

It is common to describe the spatial distribution of atoms within the material with the pair correlation functions [4, 121–123]. These can be obtained through diffraction experiments and are one of the fundamental tools for the structural characterization of condensed matter, since with them, one may identify several phases of the material, or whether it has an amorphous or crystalline structure.

The so called Correlation Function of Atomic Pairs, $\rho(r)$, reaches maximum values for distances r in which it is more possible to find one atom given the position of another one. Moreover, in a structurally disordered solid, for large interatomic distances $\rho(r)$ tends to its numerical density: $\rho_0 = N/V$, with N the number of atoms within the volume V.

One of the most common functions to structurally describe disordered solids is the Pair Distribution Function (PDF), $g(r)$, which is related to $\rho(r)$ by:

$$g(r) = \frac{\rho(r)}{\rho_0} \tag{2.18}$$

As a visual reference of $g(r)$, this function for an amorphous material is schematically shown in Figure 2.3 [4, 121–123].

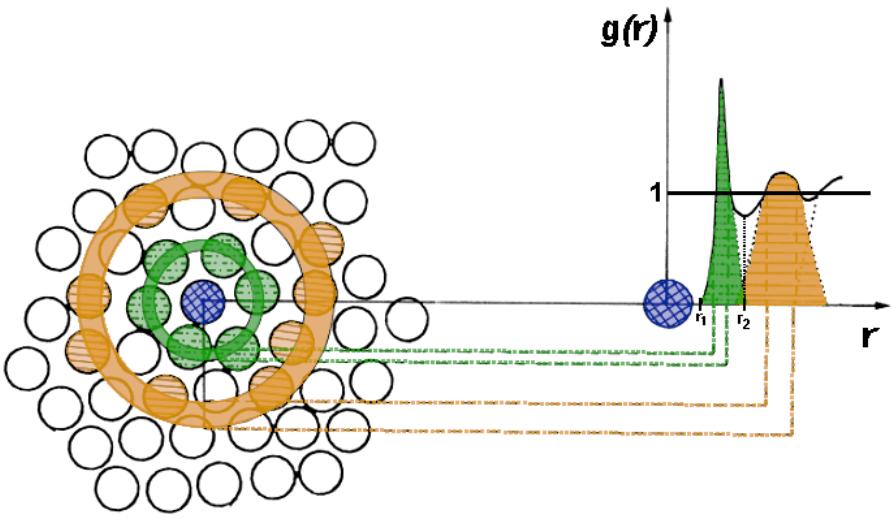

FIGURE 2.3. Scheme of the PDF, $g(r)$, for a hypothetical amorphous material. Notice the tendency to a constant value 1. Adapted from Ziman [4].

Another common correlation function is the Radial Distribution Function (RDF), $J(r)$, which is defined in terms of $g(r)$ as follows [121]:

$$J(r) = 4\pi\rho_0 r^2 g(r) \tag{2.19}$$

The importance of the RDF lies on the fact that it is used to calculate the average coordination number, $N_{\text{n-n}}$ (that is the number of nearest-neighbors, n-n, around a specific atom), for the material by integrating it over the first coordination shell, defined within the interval $[r_1, r_2]$, where r_1 is the lowest value for which $g(r) \neq 0$, and r_2 is the first minimum of $g(r)$ after the first peak (see Figure 2.3) [121]:

$$N_{\text{n-n}} = \int_{r_1}^{r_2} \mathrm{d}r J(r) \tag{2.20}$$

Finally, another useful correlation function is the reduced Pair Distribution Function (rPDF), $G(r)$ [34], which is frequently obtained from x-ray diffraction studies and is defined by:

$$G(r) = 4\pi r\rho_0 \left[g(r) - 1\right]. \tag{2.21}$$

These correlation functions, among others, can be calculated with the `Correlation` code, which was developed in our group by Rodríguez *et al.* [124] and is used throughout this investigation.

2.3 Electronic Specific Heat

From a thermodynamic point of view [125], the second derivatives of a system's thermodynamic potential, such as the Helmoltz or Gibbs energies, describe its macroscopic properties such as the specific heat (eq. (1.1)). These quantities are frequently measured in experiments and give insight into the manner the atoms that constitute the material interact with each other and with their surroundings.

A fact of classical theory of atomic vibrations in solids is that the specific heat at high temperatures approximates a constant value of $3N_Ak_B$, where N_A is Avogadro's number and k_B is the Boltzmann constant, a result known as the *Dulong-Petit Law* [2]. Whereas for low to intermediate temperatures, where the quantum-mechanical effects are not negligible, the specific heat consists of two contributions: one linear and another cubic with temperature [2]:

$$c = \gamma T + \alpha T^3 \tag{2.22}$$

The γ and α coefficients correspond, respectively, to the electronic and vibrational contributions to the specific heat in the range of low to intermediate temperatures, and both can be expressed in terms of intrinsic properties of the material: the eDoS at the Fermi level, $N(E_F)$, and the Debye temperature, Θ_D.

$$\gamma = \frac{\pi^2}{3} k_B^2 N(E_F) \tag{2.23}$$

$$\alpha = \frac{12\pi^4 k_B}{5\Theta_D^3} \tag{2.24}$$

where k_B is the Boltzmann constant.

Both quantities, $N(E_F)$ and Θ_D respectively emerge from the quantum-mechanical description of the electrons and nuclei vibrations within a solid. $N(E_F)$ is a measure of the number of the highest-energy electrons which are prone to be excited by external influences and Θ_D is "a measure of the temperature above which all [vibrational] modes begin to be excited, and below which modes begin to be 'frozen out' " [2]. Fortunately, $N(E_F)$ and Θ_D are two quantities that can be obtained through DFT calculations (subsections 3.3.4 and 3.3.5). Once more, the predictive power of quantum-mechanical calculations cannot be underestimated.

2.4 Phonons and Thermodynamic Functions

As was stated in Section 2.3, the measurement of thermodynamic functions give an insight into the physics of the condensed matter. The vibrational, or phonon, contributions to the energy of the system at any temperature are of great relevance besides the calculation of the low temperature specific heat stated in the previous section. Thus, one of the principal applications of the vibrational energy spectra ($g(\omega)$ or $F(\omega)$, subsection 3.3.5), is the determination of several thermodynamic functions that provide information about the local environment of the nuclei within the material [126].

Considering the total energy E_{n_j} of a collection of quantum harmonic oscillators in the state n_j which oscillate with frequency ω_j:

$$E_{n_j} = \sum_j \left(n_j + \frac{1}{2} \right) \hbar\omega_j \tag{2.25}$$

where $\hbar$ is Planck's constant divided by 2π, the partition function Z of the system can be constructed:

$$Z = \sum_j \exp\left(-\beta E_{n_j}\right) \tag{2.26}$$

where $\beta = 1/k_B T$. And from Z, the Helmoltz energy F is obtained [106, 126, 127]:

$$F = -k_B T \ln Z = k_B T \sum_j \ln\left\{ 2\sinh \frac{\hbar\omega_j}{2k_B T} \right\} \tag{2.27}$$

Now, when considering a model consisting of N unit cells, each one containing n atoms, that has an energy spectrum $g(\omega)$ with ω_L the highest phonon frequency, equation (2.27) becomes [126]:

$$F = 3nNk_B T \int_0^{\omega_L} \ln\left\{ 2\sinh \frac{\hbar\omega}{2k_B T} \right\} g(\omega)\, d\omega, \tag{2.28}$$

Then, from equation (2.28) one can derive two important thermodynamic functions for the internal energy [126]:

$$\Delta E = 3nN\frac{\hbar}{2} \int_0^{\omega_L} \omega \coth \frac{\hbar\omega}{2k_B T}\, g(\omega)\, d\omega, \tag{2.29}$$

and the constant volume specific heat [126]:

$$C_v = 3nNk_B \int_0^{\omega_L} \left[\frac{\hbar\omega}{2k_B T} \right]^2 \operatorname{csch}^2 \frac{\hbar\omega}{2k_B T}\, g(\omega)\, d\omega, \tag{2.30}$$

2.5 BCS Theory of Superconductivity

The phenomenon of superconductivity, in which electrical currents flow without resistance and magnetic fields are excluded from entering the superconductor, has attracted much attention from scientists since its discovery in 1911 by H. Kamerling Onnes [54]. Back in 1935, constitutive relations among the superconducting current and the electromagnetic fields inside a superconductor where proposed [128]. Later in 1950, a phenomenological model that characterizes the superconducting state by an order parameter was put forth [129]. However, it was not until 1957 that a satisfying microscopic theory of superconductivity was created: the Bardeen-Cooper-Schrieffer (BCS) theory [55], in which an attractive interaction between electrons mediated by phonons is responsible of the superconducting state.

One of the greatest achievements of the BCS theory is the prediction of a critical temperature T_c such that the metallic solid behave as a normal metal when above that temperature, and superconducts below it.

$$T_c = 1.13\Theta_D \exp\left(\frac{-1}{N(E_F)\, V_0}\right) \tag{2.31}$$

where V_0 is the electron-electron phonon-mediated attractive potential and, again, Θ_D is the Debye temperature and $N(E_F)$ is the eDoS at the Fermi level.

The importance of this result is that the critical temperature can be calculated from intrinsic material properties determined by $N(E)$, Θ_D and V_0. In principle, all three can be obtained from DFT calculations: $N(E)$ and Θ_D are readily obtained for ordered and disordered systems, however a higher computational cost is involved in the calculation from first-principles of V_0; even though there exist some codes and software which claim to calculate it, as far as we know, they do so only for crystalline perfect systems and on supercells containing low number of atoms, not applicable to our amorphous structures. In this manner, assumptions regarding V_0 will be done and explained in the corresponding section for this work.

3 Methods

This chapter is divided into three sections which describe the methodology followed in this Part I of the thesis. In section 3.1, the software and codes employed in the investigation are reported; in section 3.2, the processes followed to construct the samples for each ordered and disordered alloy are detailed; and in section 3.3, features needed to describe some physical properties of the studied systems are briefly discussed.

Contents from subsections (s.s.) that addressed the Materials studio software (s.s 3.1.1), the electronic parameters for the DMol^3 code (s.s. 3.3.1), the electronic (s.s. 3.3.4) and phononic (s.s. 3.3.5) energy spectra, and the *à la* Mata-Pinzón *et al.* approach (s.s. 3.3.6), are also employed in Part II of this thesis.

3.1 Software and codes

3.1.1 Materials Studio

The software used was Materials Studio 2016, a suite of codes provided by Biovia Dassault Systèmes [130] which incorporates several modules oriented to materials research. Specifically, the modules utilized for this investigation were DMol^3 [112–114] and Forcite.

DMol^3 is an *ab initio* code which employs numerical atomic orbitals as the basis set to find the ground-state electronic density through the Density Functional Theory framework [131]. In this work, DMol^3 was employed to perform the entire DFT-based calculations, including the *ab initio* Molecular Dynamics (AIMD) and Geometry Optimization (GO) procedures, and the determination of the electronic (eDoS) and vibrational Densities of States (vDoS).

Forcite is a module that "allows you to perform a wide range of molecular mechanics calculations on both molecular and periodic systems using classical forcefield-based simulation techniques" [132]. However, since the present investigation is based on a first-principles approach, the majority of Forcite's simulation features were not exploited and only the structural characterization tool which calculates the Pair Distribution Functions (PDFs) was employed.

3.1.2 `Correlation` Code by Rodríguez *et al.*

As a complement and an improvement to not only calculate the Pair Distribution Functions but several other correlation functions such as the Reduced Distribution Function ($G(r)$) and the Plane Angle Distribution Function (PAD), the code `Correlation` [124], published by Rodríguez *et al.* in 2021, was employed to analyze the amorphous structure of the BN alloy.

3.2 Processes

Disordered substitutional alloy

Substitutional disorder in binary alloys is the simplest type of disorder studied [4, 6]. As was previously explained, the most common theoretical approaches to the study of these materials (e.g. CPA or SQS) lack the local atomic description which may be responsible of the peculiar macroscopic behavior of the alloy. Recognizing that the local environment needs to be incorporated in the simulation of alloys in order to improve the existing models, our approach begins with the construction of a supercell in which the atoms randomly occupy lattice sites which either

1. yield a stable atomic spatial distribution such that it is possible to observe the real alloy with that underlying periodic structure regardless the atomic species occupying each site, or
2. yield an unstable structure, impossible to observe in the real alloy.

The atomic arrangement of case 1 is chosen when studying solid solutions that need to be modeled by periodic supercells, constructing several of them by changing the atomic arrangement but not the underlying structure aiming to average their calculated properties. The atomic arrangement of case 2 is chosen when studying structurally disordered alloys, in which our amorphization procedure, detailed below these lines, is performed.

Amorphization process: the *Undermelt-quench* method

The amorphization process developed in our workgroup is known as the *undermelt-quench* method [133] and it has been employed to simulate amorphous and porous semiconductors [134–136] and amorphous alloys [40, 137–140]. This computational method has given good results in obtaining disordered structural atomic arrangements when compared to experimentally-obtained PDFs as well as to other theoretical calculations found in the literature. The agreement has given us the certainty that the disordered structures obtained in this manner are representative of a bulk macroscopic amorphous sample, allowing us to study their electronic and vibrational properties so that macroscopic features

like the optical behavior [141] and superconducting transition temperatures [63] can be adequately studied, compared and validated, and on this ground, even try to predict new interesting behaviors for the amorphous system.

The *undermelt-quench* method considers an initial unstable supercell in order to propitiate the amorphization process. This instability can be achieved in two manners: 1) changing the mass density by expanding the volume of the supercell whereas conserving the crystalline stable structure, or 2) maintaining the same mass density but using a different periodic structure which is unstable for the crystalline system. Both approaches have been proven to give structurally appropriate amorphous structures.

By means of AIMD, the unstable supercell is linearly heated in 100 steps from $300\,\mathrm{K}$ up to a temperature below the solidus temperature for multiatomic systems (or the melting temperature for pure systems) followed immediately by a cooling ramp which takes the system down to a temperature near $0\,\mathrm{K}$, diminishing the temperature in each step at the same rate as the heating ramp. In Figure 3.1 the entire *undermelt-quench* process is depicted.

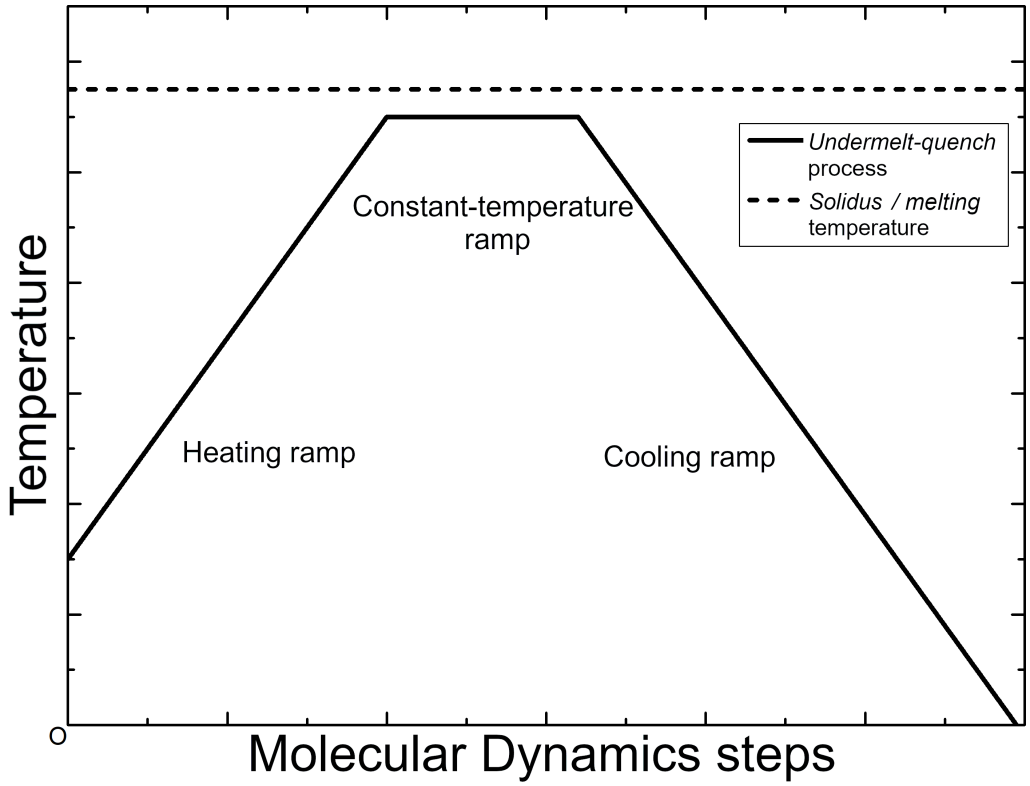

FIGURE 3.1. Scheme of the *undermelt-quench* process. This version of the process depicts the heating, constant, and cooling ramps. In other versions, the constant ramp is omitted and the cooling ramp immediately follows the heating ramp. The horizontal dashed line represents the solidus/melting temperature.

Since after the *undermelt-quench* process the atoms within the supercell may not be in a local minimum energy configuration according to an amorphous metastable structure (the global energy minimum corresponds to a perfectly ordered crystalline state), a Geometry Optimization (GO) procedure is performed. In this sense, in each step of the GO process the total energy of the system and the forces acting upon each atom are calculated, then an energy minimization algorithm leads the system into a metastable one which corresponds to a local energy minimum in which the internal forces are practically null. Finally, the amorphous supercell obtained after the GO is structurally described by its correlation functions and compared to experiments if any.

It is important to state that the amorphization process followed here does not try to mimic the actual experimental quenching procedures to generate amorphous samples; typical MD simulation times are of the order of picoseconds, giving quenching rates of the order of $10^{15}\,\mathrm{K/s}$, whereas experiments concerning metallic amorphous alloys require quenching rates anywhere from $10^{3}\,\mathrm{K/s}$ to $10^{9}\,\mathrm{K/s}$, depending on the system [34, 142, 143]. So the objective of this approach is to find, with our supercells, an amorphous structure which can be taken as a representative one of the bulk amorphous material.

3.3 Parameters, properties and characterizations

3.3.1 Electronic parameters for DFT calculations

The electronic problem treated by DFT in DMol^3 requires the specification of some parameters.

Unless otherwise stated,

- all the *ab initio* calculations were done with DMol^3 code [112–115] employing unrestricted spin-polarized wavefunctions;
- the chosen wavefunctions basis set consisted in double-numerical plus d-polarization functions (DND basis) atom-centered orbitals [131];
- the wavefunctions' real-space cutoffs were set to $4.5\,\text{Å}$;
- LDA was the chosen approximation for the exchange-correlation functional (see Section 2.1 and Ref. [96]), in the Vosko, Wilk, and Nusair [116] parametrization.
- the employed pseudopotentials were the norm-conserving [96] Density functional Semi-core PseudoPotentials (DSPPs) [120], which are generated by fitting the pseudo-wavefunctions to all-electron relativistic DFT results and are specifically designed to reproduce accurate DMol^3 calculations [131];

- an electronic density convergence threshold of 1×10^{-6} was employed for the self-consistent Kohn-Sham calculations (see Section 2.1 and Refs. [96, 131]); and
- a linear mixing scheme (see Section 2.1 and Refs. [96, 131]) was used to update the electronic charge and spin densities in the self-consistent calculation. For the charge mixing a value of 0.1 was chosen, for the spin mixing a value of 0.5 was chosen.

3.3.2 AIMD and GO parameters

The *undermelt-quench* processes by AIMD and the GOs that followed them were done with the `DMol`^{3} code.

Unless otherwise stated, for the AIMD:

- the chosen timestep, t_s, was the triple of the default one, t_d:

$$t_s = 3t_d = 3\left(\frac{M_s}{5}\right)^{1/2} \text{fs}$$

  where M_s is the mass of the lightest element in the supercell;
- the ensemble used was NVT with the Simple Nosé-Hoover thermostat with a Q parameter of 0.5 (see Section 2.1 and Refs. [109–111, 131]; and
- the initial atomic velocities were randomly assigned to each atom such that the velocities followed a Maxwell-Boltzmann distribution at a temperature of $300\,\text{K}$;

and for the GO, the threshold values were:

- $1 \times 10^{-5}\,\text{Ha}$ for the energy criterion of convergence,
- $2 \times 10^{-3}\,\text{Ha}\,\text{Å}^{-1}$ for the gradient criterion of convergence, and
- $5 \times 10^{-3}\,\text{Å}$ for the displacement criterion for convergence.

3.3.3 Structural Description

The structural information concerning the spatial distribution of the atoms is described by means of the correlation functions discussed in Section 2.2.

Unless otherwise stated,

- histograms of $0.5\,\text{Å}$ width were employed to determine the correlation functions $g(r)$, $J(r)$, and $G(r)$, regardless of the used software (`Forcite` or `Correlation`), and

- a 3-point Fast Fourier Transform (FFT) algorithm was employed to smooth the histograms and report the corresponding correlation functions.

3.3.4 Electronic Structure

When the perfect periodicity of a material is lost (e.g. when trying to simulate complex materials such as disordered alloys or amorphous solids), some mathematical constructions which rely on these assumptions, such as the band structure or Brillouin zones, become hard to give a satisfactory interpretation within the theory of disordered systems. However, a concept that maintains its valid interpretation whether analyzing ordered or disordered materials, is the electronic Density of States (eDoS or $N(E)$), defined to be the sum over all electronic states labeled by k with energy E_k within an energy interval $(E, E + dE)$ that are present in the supercell model [32, 144]:

$$N(E) = \sum_{\text{all} E_k} \delta\left(E - E_k\right). \tag{3.1}$$

Therefore, the eDoS is the tool we shall employ throughout this work to study the electronic structure of all our ordered and disordered samples.

Unless otherwise stated,

- the δ functions in equation (3.1) are smeared by Gaussian functions of $0.2\,\mathrm{eV}$ width,
- the smeared eDoS functions are normalized by the total number of atoms present in the corresponding supercell, such that their units are $\mathrm{electrons}/(\mathrm{eV\,atom})$.

3.3.5 Phononic Structure

To study the vibrational or phononic energy spectra, the eigenvalues of the dynamical matrix ($3N \times 3N$ square matrix formed by the second-order partial derivatives of the N-atom supercell's energy with respect to atomic coordinates) [2] were calculated by finite differences. The square root of the $3N$ calculated eigenvalues, labeled by k, correspond to the vibrational modes of frequency ω_k and energy $\hbar\omega_k$, and these are used to determine the phonon or vibrational Density of States (vDoS, $F(\omega)$, or $g(\omega)$).

Unless otherwise stated,

- a step size of $0.005\,\text{Å}$ was used for the finite-differences algorithm,
- histograms of width $1.5\,\mathrm{meV}$ were employed to count the number of vibrational modes within that interval for the whole energy spectrum and

- those histograms were smoothed by a 3-point FFT algorithm to find the corresponding vDoS.
- The smoothed vDoS functions are normalized such that the area under the curve es equal to one, allowing the direct comparison of the vibrational spectra among supercells with different number of atoms.

3.3.6 Superconducting Critical Temperature, T_c, *à la* Mata-Pinzón *et al.*

In order to estimate the superconducting transition temperatures (T_c, equation (2.31)) within the BCS framework, values for the eDoS at the Fermi level ($N(E_F)$, subsection 3.3.4) and the Debye temperature (Θ_D) are required; $N(E_F)$ is determined from DFT calculations, whereas Θ_D is calculated from the vDoS (s.s. 3.3.5) as follows [145]:

$$\Theta_D = \frac{\hbar}{k_B} \exp\left[\frac{1}{3} + \frac{\int_0^{\omega_{\max}} \ln(\omega) g(\omega) d\omega}{\int_0^{\omega_{\max}} g(\omega) d\omega}\right] \tag{3.2}$$

where $\hbar$ is Planck's constant divided by 2π, k_B is the Boltzmann constant, and $\omega_{\max}$ is the maximum vibration frequency from the vDoS.

Back in 2016, Mata-Pinzón *et al.* [63] developed a method to predict an upper limit for the T_c of crystalline bismuth (Wyckoff structure) based on the already measured T_c for the amorphous phase and the eDoS and vDoS calculations. Their predicted limit of $1.3\,\mathrm{mK}$ was experimentally validated one year later: Prakash *et al.* [64] measured a T_c of $0.53\,\mathrm{mK}$ for crystalline bismuth at ambient pressure. In this work, the Mata-Pinzón *et al.* approach is adapted to study superconductivity in other structures and phases of bismuth such as the layered and the under-pressure pure-bismuth crystalline structures, as well as the copper-bismuth amorphous structure as an example of a bismuth-based binary alloy. The *á la* Mata-Pinzón *et al.* method is described next for two arbitrary systems labeled as Q and R; when analyzing a specific phase or structure, these labels will change accordingly and will be specified in the corresponding section.

Let R be a material which is a superconductor below the critical temperature T_c^R and has an electronic density of states at the Fermi level of $N^R(E_F)$ and a Debye temperature of Θ_D^R. Let Q be a material for which we want to calculate its critical superconducting temperature T_c^Q, provided we know its eDoS at the Fermi level: $N^Q(E_F)$, and its Debye temperature: Θ_D^Q. We postulate one can get system Q by doping, alloying, or applying external pressure to system R.

Two suppositions are of central importance for the method to be applied in our cases:

- The superconducting materials Q and R can be described by the BCS equation for the superconducting transition temperature T_c (same as equation (2.31)):

$$T_c = 1.13\ \Theta_D \exp\left(\frac{-1}{N(E_F)\ V_0}\right) \tag{3.3}$$

- The Cooper pairing potential V_0 is the same for both Q and R systems no matter the phase or structure studied.

From these suppositions, the critical temperature (3.3) for material R is given by:

$$T_c^R = 1.13\ \Theta_D^R \exp\left(\frac{-1}{N^R(E_F)\ V_0}\right) \tag{3.4}$$

whereas for material Q is:

$$T_c^Q = 1.13\ \Theta_D^Q \exp\left(\frac{-1}{N^Q(E_F)\ V_0}\right) \tag{3.5}$$

Now, $N^Q(E_F)$ and $N^R(E_F)$ are related themselves by the proportionality factor η:

$$N^Q(E_F) = \eta\ N^R(E_F) \tag{3.6}$$

while Θ_D^Q is related to Θ_D^R by the factor μ:

$$\Theta_D^Q = \mu\ \Theta_D^R, \tag{3.7}$$

From equations (3.4), (3.5), (3.6), and (3.7) and taking the ratio $\dfrac{T_c^Q}{T_c^R}$, one can solve for T_c^Q to finally obtain:

$$T_c^Q = \mu\ \left[T_c^R\right]^{1/\eta}\ \left[1.13\ \Theta_D^R\right]^{(\eta-1)/\eta} \tag{3.8}$$

Equation (3.8) shall be used in what follows.

3.3.7 Thermodynamic Functions

The thermodynamic functions studied in this work are the lattice contributions to the internal energy (eq. (2.29)) and to the constant volume specific heat (eq. (2.30)); to determine both functions the knowledge of $g(\omega)$ is required. For clarity, those equations are reproduced next:

Internal Energy:

$$\Delta E = 3nN\frac{\hbar}{2}\int_0^{\omega_L} \omega \coth \frac{\hbar\omega}{2k_BT} g(\omega)d\omega, \tag{3.9}$$

Constant Volume Specific Heat:

$$C_v = 3nNk_B \int_0^{\omega_L} \left(\frac{\hbar\omega}{2k_BT}\right)^2 \operatorname{csch}^2 \frac{\hbar\omega}{2k_BT}\, g(\omega)d\omega, \tag{3.10}$$

This page intentionally left blank

4 Results

As was mentioned throughout the text, the principal objective of this work is the theoretical study of binary alloys by their simulation and modeling. This chapter is divided into three sections corresponding to each studied alloy. The first section is about the substitutionally disordered Au_xAg_{100-x} alloys and their electronic specific heats as a function of the atomic concentration, the second section reports the calculated superconducting transition temperature for the amorphous CuBi amorphous $Cu_{61}Bi_{39}$ alloy, and thermodynamic functions of the amorphous BN system are reported in the third section.

4.1 Au_xAg_{100-x} (Hinojosa-Romero *et al.* To be published)

4.1.1 Construction

Recalling the discussion of Chapter 1 on alloy models, without invoking symmetry arguments, the number of different substitutionally disordered supercells that can be constructed containing N atoms is 2^N. For $N = 108$, this number is higher than 3.2×10^{32}, making it impossible to analyze all of them from an *ab initio* approach. Even if symmetries are considered, that number does not reduce considerably for doing practical calculations.

Therefore, our approach for the simulation of the substitutionally disordered Au_xAg_{100-x} alloys consists of constructing four different 108-atom supercell models for each of the atomic concentrations: $x = 0$, 4, 13, 20, 30, 40, 50, 75, 90 and 100 and then averaging the calculated eDoS over the four configurations, in the understanding that the local atomic environment is well described by the *ab initio* calculations. The 108 atoms within our supercell models randomly occupied fixed positions located at FCC-lattice sites and the densities of the samples were adjusted to that reported in the literature [146] by changing the size of the supercells edges while preserving the fractional coordinates.

In order to determine the adequate exchange-correlation functional (Section 2.1) for these calculations, a sample structure of $Au_{50}Ag_{50}$ was chosen to perform total energy calculations as a function of the lattice parameter with two functionals: LDA-VWN, and GGA-PBE. Then, the binding energy (difference between the energy of the alloyed system and the energy of all the atoms considered isolated from each other [32]) for each supercell was employed to compare both functionals. The

results for these calculations are shown in Figure 4.1, where quadratic fits are depicted as the solid black and red curves for the LDA-VWN and GGA-PBE functionals, respectively.

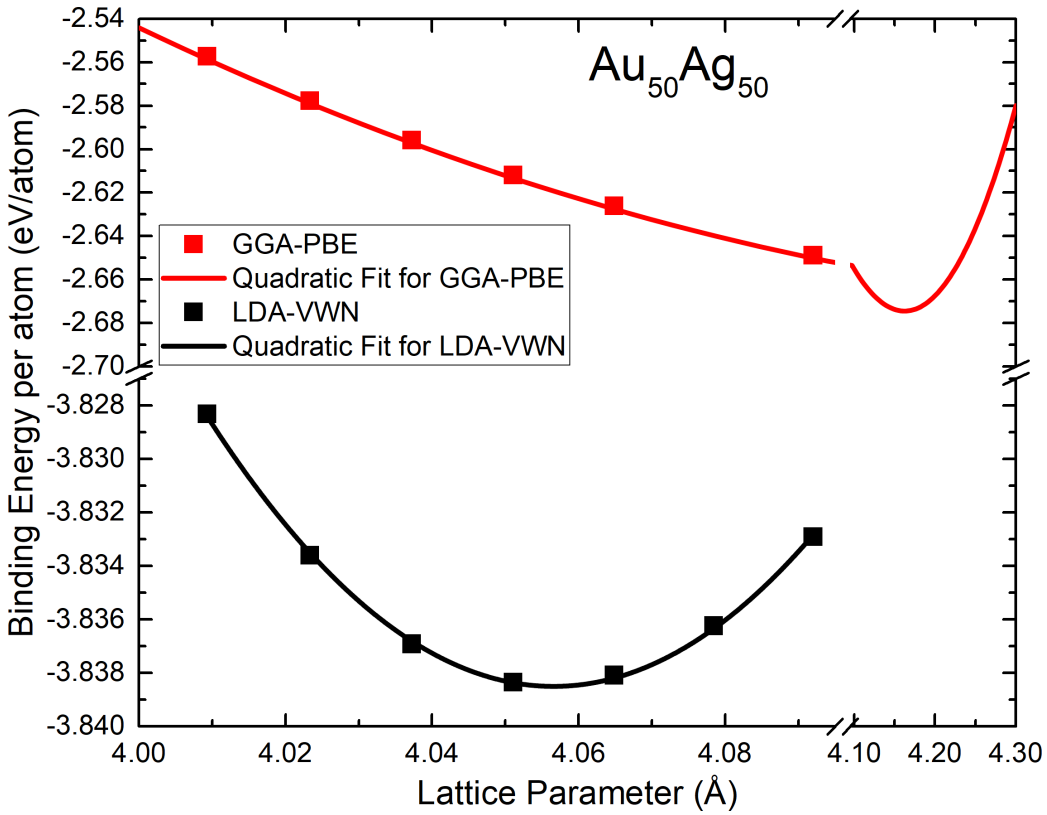

FIGURE 4.1. Calculated Binding Energy per atom as a function of the lattice parameter for a $Au_{50}Ag_{50}$ sample structure. Calculations were done using the LDA-VWN functional (black squares) and GGA-PBE functional (red squares). The black and red solid curves are quadratic adjustments for the calculated data of both functionals. The horizontal axis is extended to explicitly shown the minimum values of our adjustments.

The parameters of the quadratic adjustment $y = y_0 + B_1 x + B_2 x^2$ for the LDA-VWN-functional curve are presented in the top row of Table 4.1, whereas those for the GGA-functional curve are presented in the middle row. In this way, the lattice parameter (last column of Table 4.1) that yields a minimum binding energy is estimated by locating the point at which the binding energy curve is minimum. The adequate exchange-correlation functional for the Au_xAg_{100-x} alloy is chosen such that the minimum value done as the one whose binding energy curve has a minimum for the extrapolated-to-$0\,\mathrm{K}$ measurement of the lattice parameter.

TABLE 4.1. Fitting parameters for the quadratic adjustments, $y = y_0 + B_1x + B_2x^2$, of LDA-VWN (black solid) and GGA-PBE (red solid) curves of Figure 4.1, and the measured lattice parameter (green solid) curve of $Au_{50}Ag_{50}$ of Figure 4.2.

	y_o	B_1	B_2	R^2	Lattice parameter Å
LDA-VWN	70.50361	-9.16317	0.28236	0.99924	4.0565
GGA-PBE	83.36361	-10.33611	0.31043	0.99999	4.1620
Measured [147]	4.057	5.780×10^{-5}	1.385×10^{-8}	0.99979	4.057

Now, the measured lattice parameter for $Ag_{50}Au_{50}$ as a function of temperature [147] is shown in Figure 4.2. The parameters for our quadratic fit ($y = y_0 + B_1x + B_2x^2$), shown as the green solid line, give a value of 4.057 Å for the lattice parameter at $T = 0\,\mathrm{K}$. Then, from Figure 4.2 and the functional comparison in Table 4.1, we conclude that the adequate functional to study the Au_xAg_{100-x} system is the LDA-VWN.

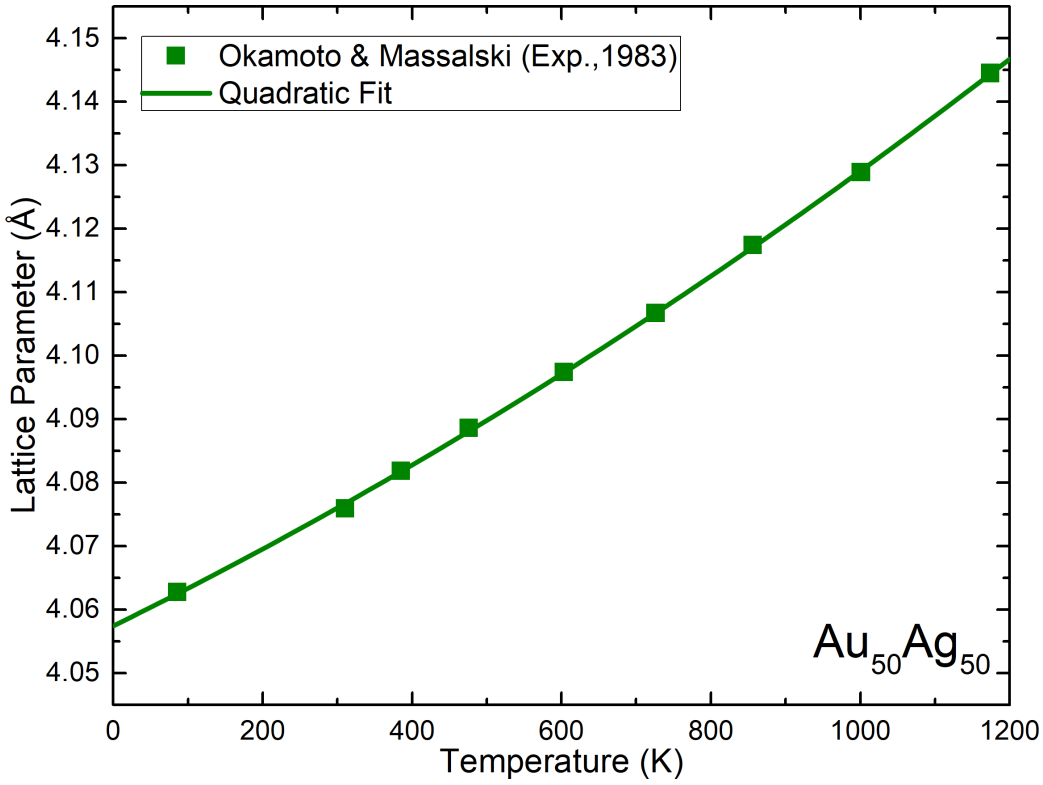

FIGURE 4.2. $Ag_{50}Au_{50}$ Lattice parameter dependence on temperature as reported by Okamoto and Massalski [147] (green squares). Green solid curve is our quadratic fit to experimental data; the fitting parameters are reported in Table 4.1.

4.1.2 eDoS

The eDoS functions were calculated for our four different substitutionally disordered Au_xAg_{100-x} supercells for each of our ten analyzed concentrations ($x = 0$, 4, 13, 20, 30, 40, 50, 75, 90 and 100). The four $N(E_F)$-per-atom curves obtained for each concentration were point-by-point summed and then divided by four (the number of curves) to obtained the averaged curves shown in Figure 4.3.

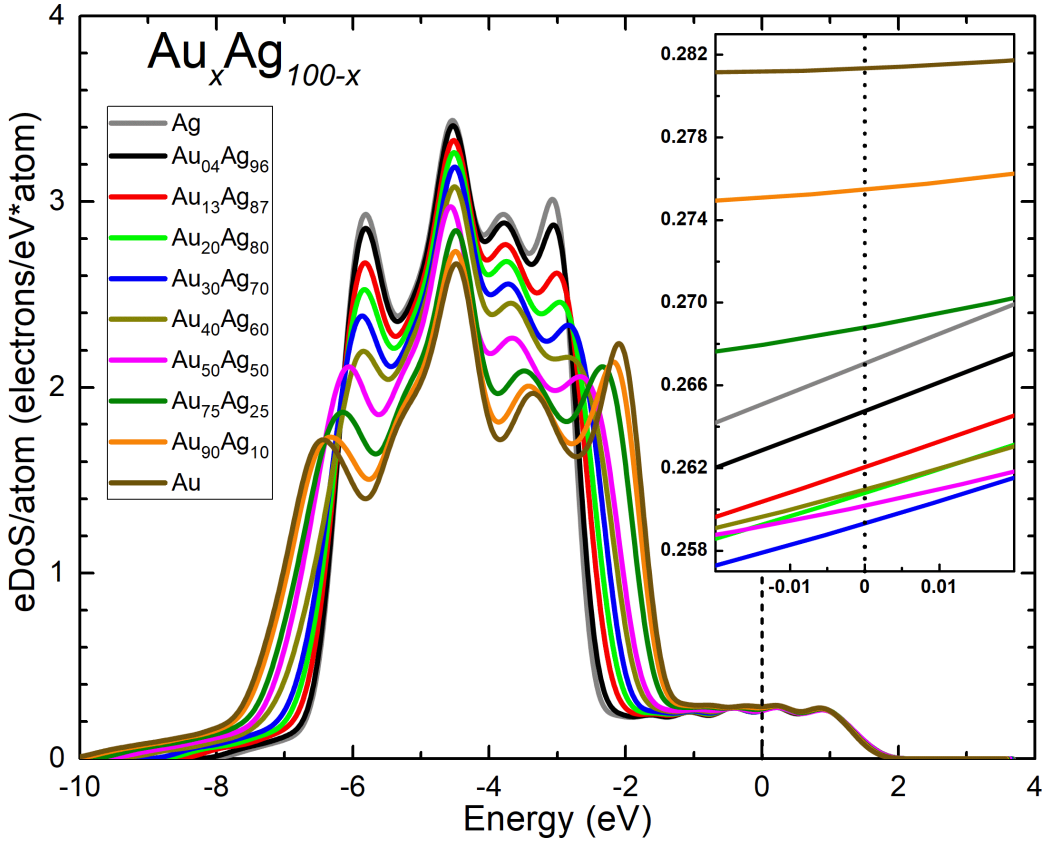

FIGURE 4.3. Averaged eDoS for our four Au_xAg_{100-x} supercells for each studied concentration. The inset shows a zoomed-in view around the Fermi level which is indicated with a black vertical dashed line.

The zoomed-in view for $N(E)$ around the Fermi level, $N(E_F)$ is shown in the inset of Figure 4.3. Its variation with the alloy's gold concentration is shown in Figure 4.4, where the averaged $N(E_F)$ are represented by black squares. Error bars of Figure 4.4 represent the standard deviation from the calculated average value and the parabolic solid line is the quadratic fit to our calculated values; the parameters of the fit are reported in Table 4.2.

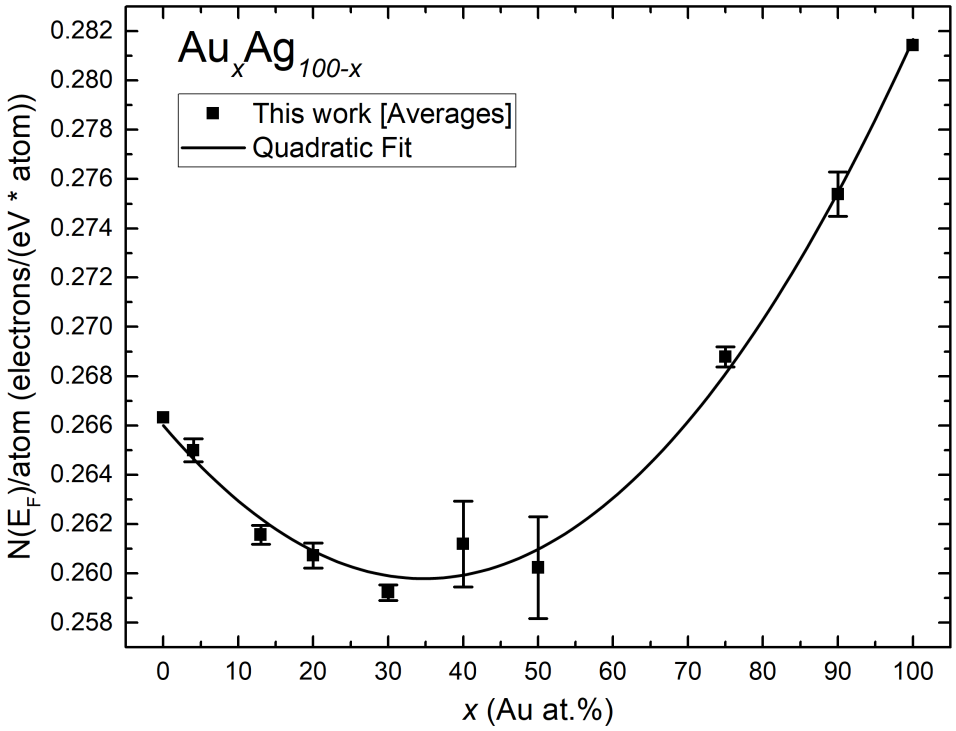

FIGURE 4.4. The averaged values for $N(E_F)$ depicted in the inset of Fig 4.3 are shown as a function of the gold atomic concentration. Error bars are the standard deviations from the calculated average for the four supercells analyzed. The parameters for the quadratic fit are reported in Table 4.2

4.1.3 Specific Heat

By the estimation of an averaged $N(E_F)$ value for the four constructed supercells for all the studied concentrations, the coefficient γ of the electronic specific heat as a function of concentration is readily obtained by equation (2.23):

$$\gamma = \frac{\pi^2}{3} k_B^2 N(E_F) \tag{2.23}$$

The results of this work, the experimental measurements due to Green and Valladares [35], Martin [44], and Davis and Rayne [45]; and the theoretical calculations of Stern [50], Haga [51], and Kokko, Ojala, and Mansikka [52], are reported in Figure 4.5.

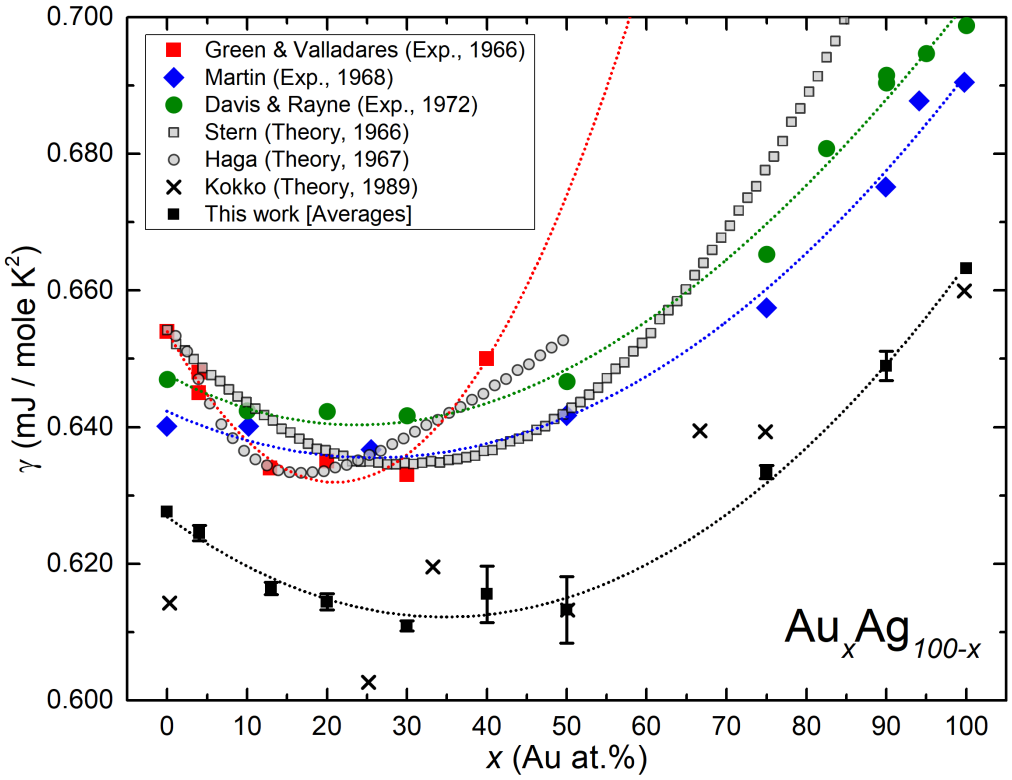

FIGURE 4.5. Measured and calculated γ coefficient of the electronic specific heat for the Au_xAg_{100-x} alloy. The results of the present work are indicated by black squares and dotted black curve. The reported fitting curves of the experimental measurements are shown by dotted red, blue, and green curves. The parameters for all the fitted curves are reported in Table 4.2

The parameters of the fitted curves of this work and the reported in Refs. [35, 44, 45], shown in Figure 4.5, are replicated in Table 4.2

TABLE 4.2. Parameters to the cubic equation that fits the measured and our calculated values for γ shown in Figure 4.5.

Reference	$y = B_0 + B_1x + B_2x^2 + B_3x^3$			
	B_0	$B_1\,(10^{-4})$	$B_2\,(10^{-5})$	$B_3\,(10^{-8})$
Green & Valladares	0.6540	−21	5.0	0
Martin	0.6423	−5.2558	1.0195	0
Davis & Rayne	0.6477	−6.2882	1.4018	−2.3005
This work	0.6269	−8.4199	1.2112	0

4.1.4 Discussion

The agreement of the qualitative parabolic behavior of our curve with that of the experimental results is remarkable given the relative low number of atoms (108) within the supercells employed in these calculations. A possible explanation for the discrepancies with experiments is that the specific heat, according to equation (2.22), depends from the lattice vibrations through Θ_D, moreover, the electron and phonon dynamics in Au_xAg_{100-x} alloys may be related by a non-negligible electron-phonon interaction. This characteristic was not considered in our calculations.

However, modifications due to electron-phonon interactions were considered in the Haga's description of the alloy through a modified $N(E_F)$:

$$N(E_F) = N_0 \left\{1 + \lambda_{\text{ep}}\, G(y)\right\} \tag{4.1}$$

where λ_{ep} is the coupling parameter for electrons and phonons, $G(y)$ is a function that measures the electron scattering due to phonons, and N_0 is the eDoS at the Fermi level of the system with no electron-phonon interactions. A more detailed study that incorporates the phonon contributions in our Au_xAg_{100-x} disordered alloys is underway.

4.2 $Cu_{61}Bi_{39}$ (Hinojosa-Romero *et al.* [148])

4.2.1 Amorphization Process and Correlation Functions

For the study of the crystalline $Cu_{61}Bi_{39}$ alloy, x-$Cu_{61}Bi_{39}$, a 144-atom supercell was constructed with the same crystalline structure reported by Clarke *et al.* [67] for their representative ordered structure at ambient pressure and temperature. So our supercell, which is shown in Figure 4.6a, consists of 88 copper atoms and 56 bismuth atoms arranged in a monoclinic structure with the space group C2/m and a density of $10.29\,\mathrm{g\,cm^{-3}}$.

The structures shown in Figure 4.6b and Figures 4.7 evidence that the x-$Cu_{61}Bi_{39}$ structure of Figure 4.6a contains two sublattices: one sublattice is formed by copper atoms distributed in chained elongated triangular bipyramids in which tree copper atoms, appearing halfway every other bipyramid in the chain (drawn as unlinked orange spheres in Fig 4.7b), alternate their location with a single bismuth atom (drawn as a purple sphere in Fig 4.7b); the other sublattice is formed by bismuth atoms arranged in a pseudo-hexagonal chained structure (see Fig. 4.7c).

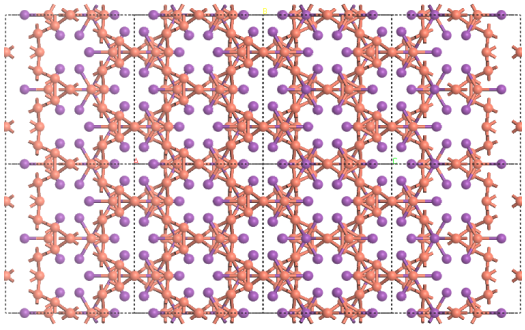

(A) x-$Cu_{61}Bi_{39}$ sphere-and-stick model structure constructed form data of ref. [67]. Sticks between atoms are a guide to independently visualize the copper and bismuth networks.

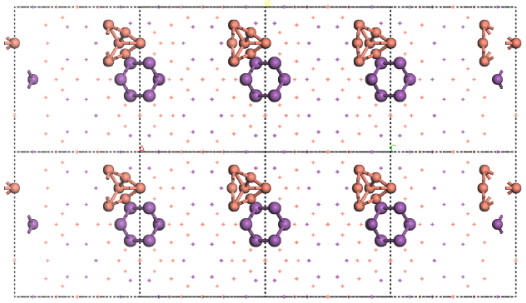

(B) Visualization of the triangular copper (orange spheres) and the pseudo-hexagonal bismuth (purple spheres) sublattices. The remaining copper and bismuth atoms are indicated by orange and purple crosses, respectively.

FIGURE 4.6. Top view of a $2 \times 2 \times 2$ multiplication of our 144-atom x-$Cu_{61}Bi_{39}$ supercell. Copper atoms are represented by orange spheres and orange crosses, bismuth atoms are represented by purple spheres and purple crosses. Lattice edges are indicated by dashed black lines. The spatial orientation is the same for both figures.

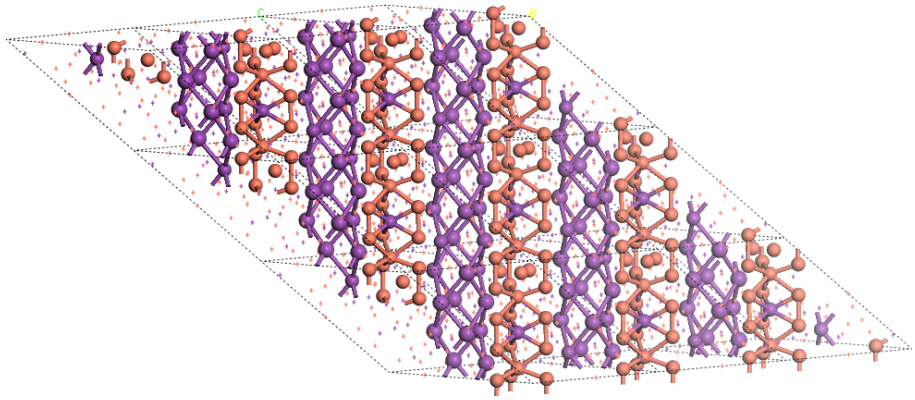

(A) Lateral view of our constructed x-$Cu_{61}Bi_{39}$ supercell. Emphasis is done in the copper and bismuth sublattices through element-colored linked spheres.

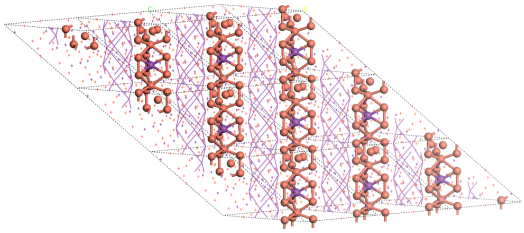

(B) The Copper sublattice within the x-$Cu_{61}Bi_{39}$ structure is indicated by orange spheres. Links between copper atoms are drawn as a guide to visualize the elongated-triangular-bipyramid chained structure. The bismuth sublattice is indicated with purple lines.

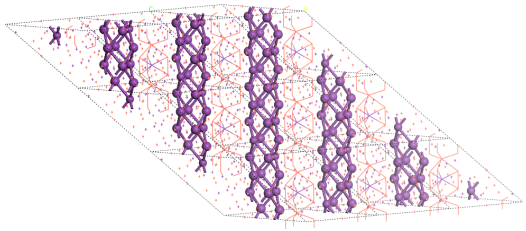

(C) The Bismuth sublattice within the x-$Cu_{61}Bi_{39}$ structure is indicated by purple spheres. Links between bismuth atoms are drawn as a guide to visualize the pseudo-hexagonal chained structure. The copper sublattice is indicated with orange lines.

FIGURE 4.7. Lateral view of a $3\times1\times3$ replication of our 144-atom x-$Cu_{61}Bi_{39}$ supercell, emphasizing the copper and the bismuth sublattices. Copper atoms are represented by orange spheres and orange crosses; bismuth atoms are represented by purple spheres and purple crosses. Sticks between atoms are drawn as a guide to the eye. Lattice edges are indicated by dashed black lines. The spatial orientation is the same for the three figures.

For the generation of the amorphous structure, a-$Cu_{61}Bi_{39}$, a 144-atom supercell underwent an *undermelt-quench* AIMD calculation (see section 3.2 and subsection 3.3.2). The supercell contains 88 copper atoms and 56 bismuth atoms randomly occupying positions that yield an FCC structure with the same density and composition of x-$Cu_{61}Bi_{39}$. The AIMD calculation consisted in a 100-step heating ramp that takes the FCC supercell from $300\,\mathrm{K}$ to $1080\,\mathrm{K}$ at a rate of $7.8\,\mathrm{K/step}$, followed by a 138-step cooling-ramp from $1080\,\mathrm{K}$ to $\approx 8\,\mathrm{K}$ at the same rate. The AIMD timestep was $10.7\,\mathrm{fs}$, producing a total simulation time of $2.547\,\mathrm{ps}$. The resulting structure was then optimized so that the atoms accommodate in their metastable equilibrium position, leading to the optimized structures shown in Figures 4.8). Finally, to determine the amorphous character of the generated supercells, the PDF of the structure was calculated and is shown in Figure 4.9.

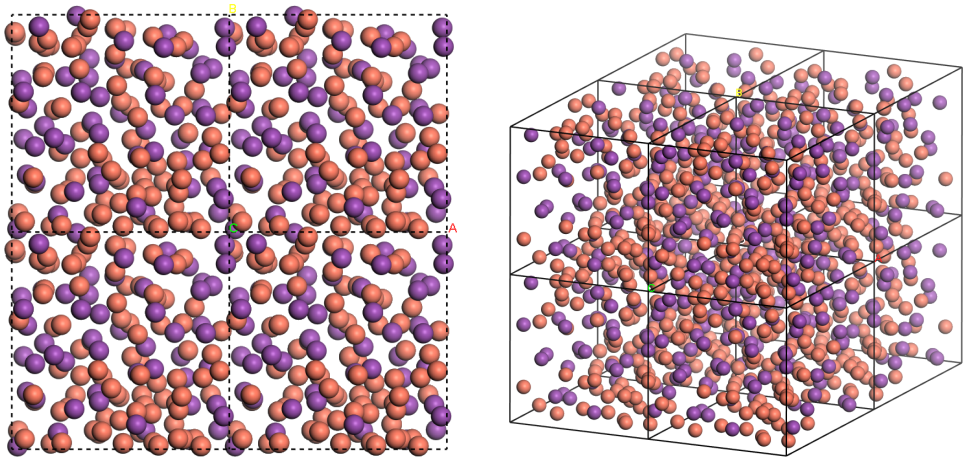

(A) Lateral view. (B) Top side view.

FIGURE 4.8. $2 \times 2 \times 2$ multiplication of the geometry-optimized 144-atom a-$Cu_{61}Bi_{39}$ supercell obtained after the AIMD *undermelt-quench* process. Orange spheres represent copper atoms and purple spheres represent bismuth atoms.

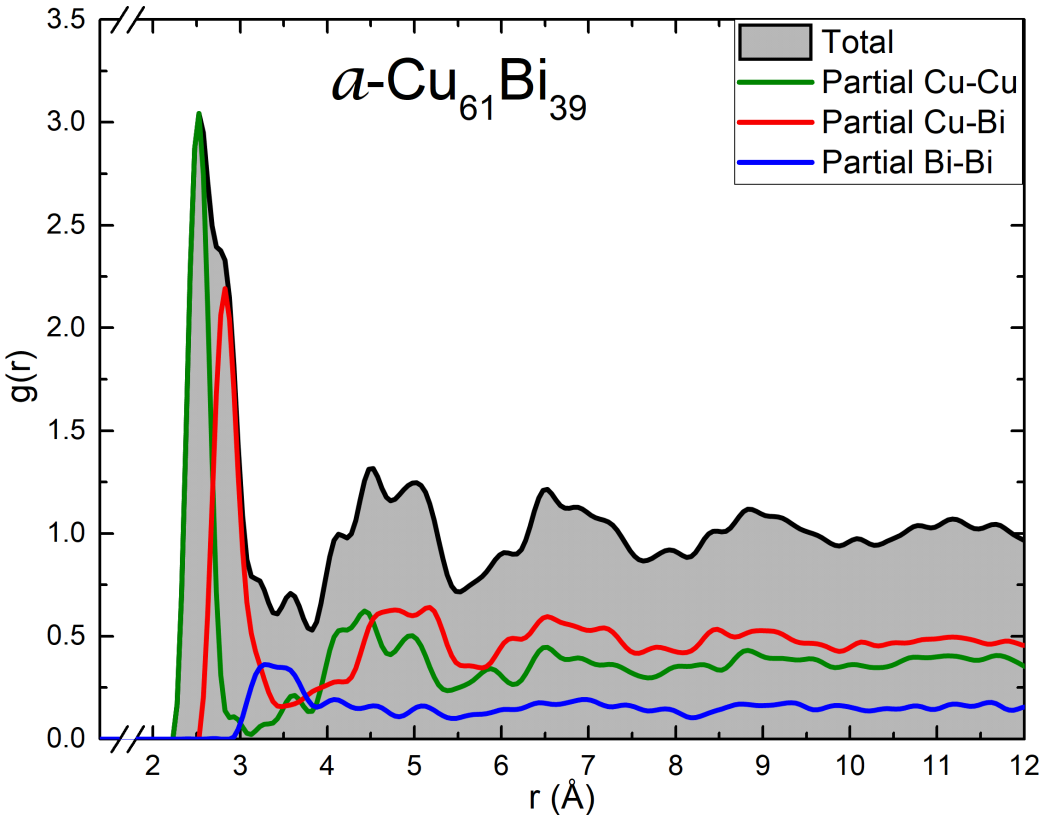

FIGURE 4.9. PDF of the a-$Cu_{61}Bi_{39}$ alloy. The total PDF (black line with shaded area) is obtained from the sum of the Cu-Cu (green line), Cu-Bi (red line), and Bi-Bi (blue line) partial PDFs.

As can be seen in Figure 4.9, several features of the obtained structure's PDF are consistent with an amorphous structure for the $Cu_{61}Bi_{39}$ alloy: the global form of the total PDF, which tends to a constant value for large distances, corresponds to an structure with no long-range-order; the characteristic second-peak bimodality of the great majority of amorphous metallic systems is visible on the Cu-Cu partial PDF around 4 to $5\,$Å; and the peculiar liquid-like form of the PDF for some amorphous metals [63, 149, 150] manifests in the Bi-Bi partial PDF. These facts validate, at least qualitatively, the applicability of the *undermelt-quench* method for the construction of an amorphous structure for this alloy.

On the other side, remnants of the short-range-order, which are inherent in the crystalline structures of the pure constituents, are also present in the obtained amorphous structure. The first peak's position ($2.53\,$Å) of the Cu-Cu partial PDF in a-$Cu_{61}Bi_{39}$ compares satisfactorily with the nearest-neighbor distance in pure crystalline copper ($2.56\,$Å [34]). Although not very well defined, there are two peaks ($\approx 3.28\,$Å and $\approx 3.53\,$Å) located within the first coordination shell in the Bi-Bi partial PDF for a-$Cu_{61}Bi_{39}$; the observed broadening around $3\,$Å and $4\,$Å is a consequence of the coalescence of the first ($3.11\,$Å) and second ($3.45\,$Å) crystalline peaks , as was shown by Mata-Pinzón *et al.* [63] for pure amorphous bismuth (see also Section 6.1).

4.2.2 Electronic Density of States, eDoS

The comparison between the calculated a-$Cu_{61}Bi_{39}$ and x-$Cu_{61}Bi_{39}$ eDoS is shown in Figure 4.10. It is remarkable that despite the different atomic arrangement between them, the general shape for the eDoS is almost the same for both systems, being the softening of the peaks for the amorphous structure the most appreciable difference. This could mean that the electronic structure is not very sensitive to the structural arrangement, in the sense that our amorphous model, just as for the crystalline structure, is composed of two independent amorphous "sub-lattices" originated by the known segregation of the constituents.

Another feature of interest is the fact that the $N(E_F)$ is higher for the amorphous structure ($N^a(E_F) = 0.38$) than for the crystalline structure ($N^x(E_F) = 0.30$), a behavior that is also present in pure bismuth [63].

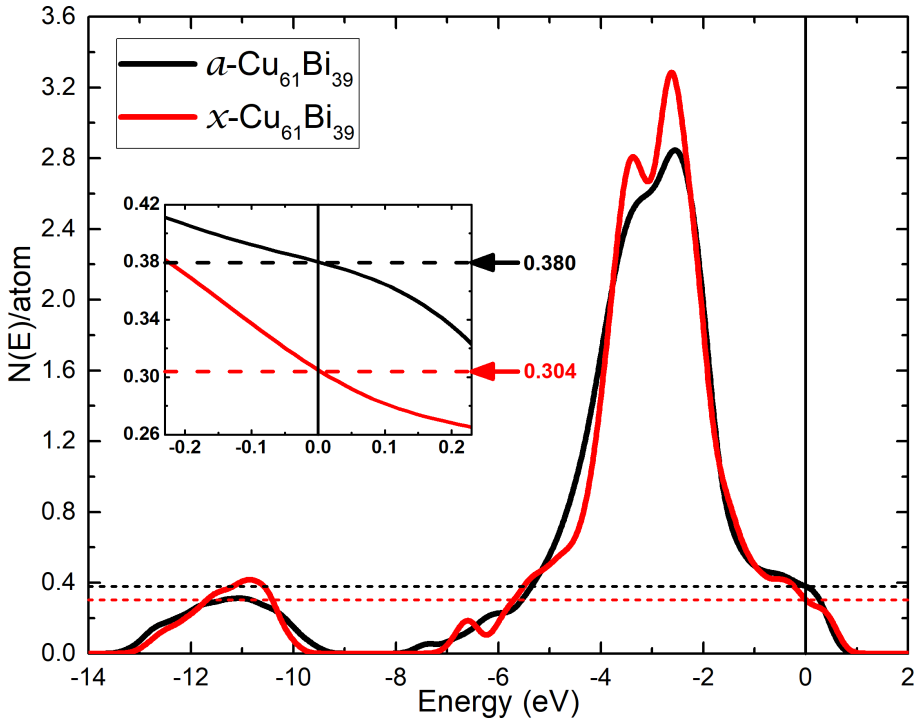

FIGURE 4.10. Comparison between the a-$Cu_{61}Bi_{39}$ (black curve) and x-$Cu_{61}Bi_{39}$ (red curve) eDoS per atom. The vertical solid black line at $E = 0\,\mathrm{eV}$ indicates the Fermi level. The inset shows a zoomed view around the Fermi level in which $N(E_F)$ is higher for the amorphous structure than for the crystalline structure.

4.2.3 Vibrational Density of States, vDoS

The comparison between the vibrational spectra of the amorphous and crystalline structures is shown in Figure 4.11. Since imaginary frequencies did not appear in our calculations, the vDoS does not present negative vibrational energies, indicating that the obtained amorphous structure as well as the crystalline constructed supercell are in a local energy minimum. Also, the x-$Cu_{61}Bi_{39}$ spectrum is more localized than the a-$Cu_{61}Bi_{39}$ spectrum; the broadening of vibrational spectra and specially the increment of low-frequency vibrational modes, is a common feature in amorphous solids that provide them some interesting transport and conducting properties.

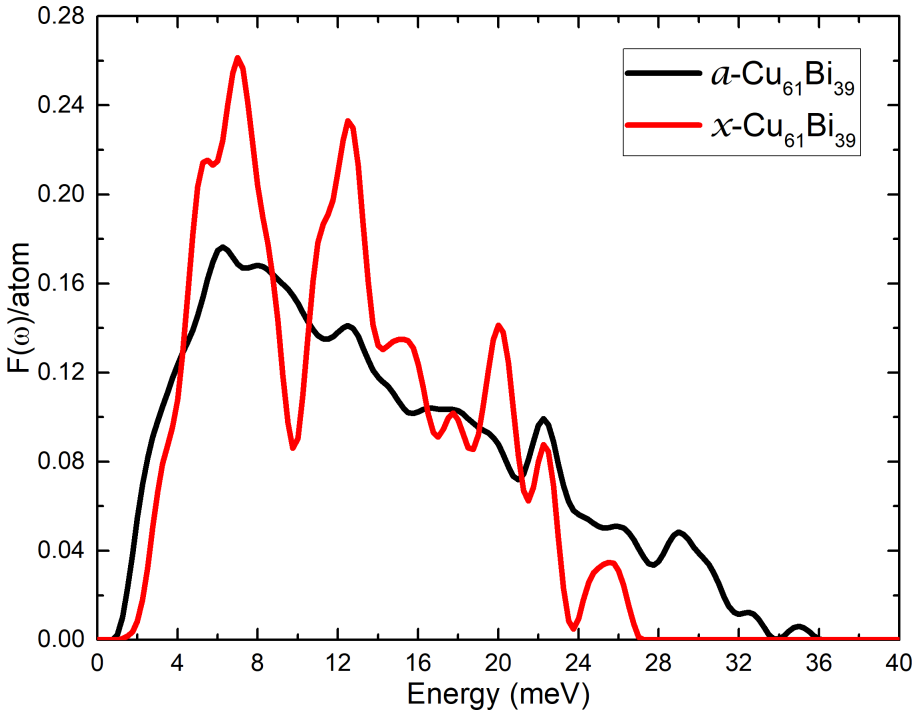

FIGURE 4.11. Comparison between the a-$Cu_{61}Bi_{39}$ (black curve) and x-$Cu_{61}Bi_{39}$ (red curve) vDoS per atom. Vibrational energies are more localized for the crystalline than for the amorphous structure, leading to a lower Debye temperature for x-$Cu_{61}Bi_{39}$.

From the calculated vDoS, the Debye temperatures can be obtained for both structures by means of equation (3.2) with the corresponding $g(\omega)$ for a-$Cu_{61}Bi_{39}$ and x-$Cu_{61}Bi_{39}$, this gives $\Theta_D^a = 182.62\,\mathrm{K}$ and $\Theta_D^x = 170.07\,\mathrm{K}$ for the amorphous and crystalline structures, respectively.

4.2.4 Superconducting Critical Temperature, T_c

Following the method of Mata-Pinzón *et al.* [63] described in subsection 3.3.6, we identify the material R as the x-$Cu_{61}Bi_{39}$ alloy, and the material Q as the a-$Cu_{61}Bi_{39}$. Thus, the identifications: $R \to x$ and $Q \to a$ in equations (3.4) to (3.8) produce:

$$\eta = \frac{N^a(E_F)}{N^x(E_F)} = 1.27 \tag{4.2}$$

from equation (3.6), for an amorphous-to-crystalline ratio of $N(E_F)$, and

$$\mu = \frac{\Theta_D^a}{\Theta_D^x} = 1.07 \tag{4.3}$$

from equation (3.7) for an amorphous-to-crystalline ratio of Θ_D.

Taking the reference value of $T_c^R \rightarrow T_c^x = 1.36\,\mathrm{K}$ as measured by Clarke *et al.* [67], the superconducting critical temperature for the amorphous phase $T_c^Q \rightarrow T_c^a$ is determined by equation (3.8),

$$T_c^Q = \mu \left[T_c^R\right]^{1/\eta} \left[1.13\,\Theta_D^R\right]^{(\eta-1)/\eta}, \tag{3.8}$$

obtaining a critical temperature of:

$$T_c^a = 4.2\,\mathrm{K} \tag{4.4}$$

4.2.5 Discussion

The rough features of the calculated PDF are those expected for an amorphous material, showing that the *undermelt-quench* method is adequate to generate amorphous structures for binary systems that do not form solid solutions, besides the so-far studied metallic and semiconduting systems. By exclusively analyzing the partial PDFs at the end of the GO process it cannot be determined if atomic segregation or clustering happened during our simulation procedures. Moreover, the almost identical eDoS for both structures subsumes for this segregation question. The investigations for the structure evolution during the AIMD and GO processes in $Cu_{61}Bi_{39}$ and other concentrations is underway.

The fact that the eDoS at the Fermi level is higher for the amorphous than for the crystalline alloys reflects the importance of bismuth's contribution to the electronic structure of the alloy since this behavior is also seen in its pure form. The calculated superconducting temperature of $4.2\,\mathrm{K}$ satisfactory compares within the range of the measured values for bismuth-based alloys.

4.3 BN (Hinojosa-Romero *et al.* Under review)

4.3.1 Amorphization Process and Correlation Functions

As happens with other semiconductors, their macroscopic properties may be a direct consequence of the hybridization of the atomic states of its constituents, and this highly depends on the density of the material. Since we do not want to impose a specific hybridization *a priori*, we decided to explore three different densities under an *ab initio* scheme. The chosen densities were 2.04, 2.80, and $3.48\,\mathrm{g\,cm^{-3}}$, which are within the crystalline's systems reported ranges [83].

Since the c-BN and w-BN systems, both having an approximate density of $3.6\,\mathrm{g\,cm^{-3}}$ [83], crystallize in diamond-like structures, it was necessary to use different starting supercells for the generation of our amorphous structures *via* the *undermelt-quench* method. In this manner, the starting supercells for the 2.04 and the $2.80\,\mathrm{g\,cm^{-3}}$ systems contained 108 boron atoms and 108 nitrogen atoms randomly occupying the lattice sites of a diamond-like structure with edges lengths of $12.96\,\text{Å}$ and $11.67\,\text{Å}$ for both densities, respectively. The starting supercell for the $3.48\,\mathrm{g\,cm^{-3}}$ system was a 256-atom FCC supercell with an edge length of $11.48\,\text{Å}$.

In order to compare our *undermelt-quench* (U-Q) method with the commonly used *melt-quench* (M-Q) method, both amorphization processes were performed and the resulting PDFs were compared. The AIMD calculations (see section 3.2 and subsection 3.3.2) consisted in a heating ramp from $300\,\mathrm{K}$ to a temperature below $2000\,\mathrm{K}$ for the U-Q method, and to a temperature of $4000\,\mathrm{K}$ for the M-Q method. Cooling ramps immediately followed until a temperature as close to $0\,\mathrm{K}$ as possible was reached. The usual geometry optimization processes were carried out after both MD calculations. It is important to stress out that the M-Q method frequently produces structures which maintain structural information of the liquid phase [133]; this is why the reduced PDFs' analysis is done exclusively for the U-Q method.

The total PDFs for the three densities and both U-Q and M-Q processes were calculated by the `Correlation` code are shown in Figures 4.12. The almost equal position for the first peaks around $1.5\,\text{Å}$ for the three densities, regardless the U-Q or the M-Q method, is a clear evidence of the conservation of the short-range order throughout both simulation processes. This method-independent feature is extrapolated to the long-range order but only for the $2.80\,\mathrm{g\,cm^{-3}}$-density supercell (Figure 4.12 b)), for which there are almost no variations between U-Q and M-Q beyond $4\,\text{Å}$.

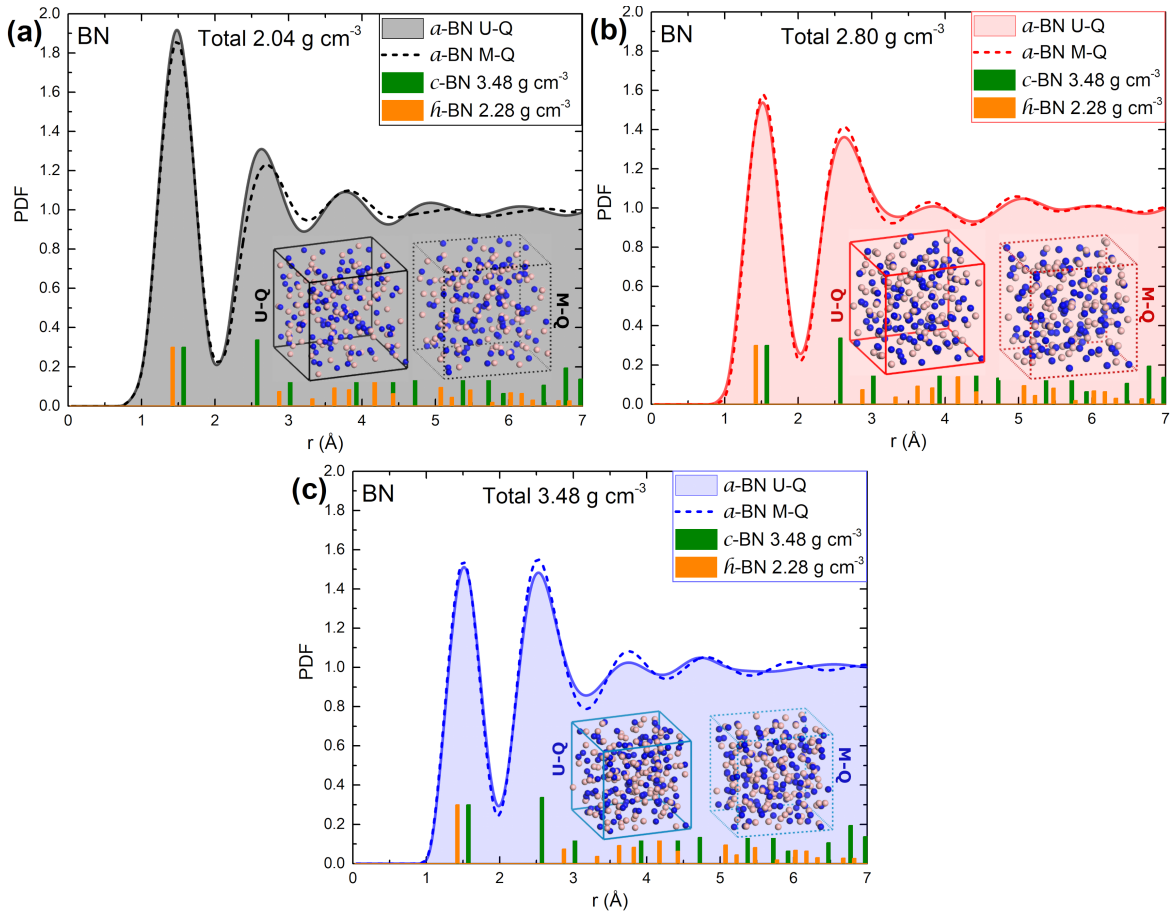

FIGURE 4.12. PDF for a-BN corresponding to the densities a) $2.04\,\mathrm{g\,cm^{-3}}$, b) $2.80\,\mathrm{g\,cm^{-3}}$, and c) $3.48\,\mathrm{g\,cm^{-3}}$ studied. The insets depict the amorphous structures obtained through the *undermelt-quench* (U-Q) and the *melt-quench* (M-Q) methods. Crystalline PDFs for c-BN and h-BN are also shown as the green and orange histograms, respectively.

Discrepancies among U-Q and M-Q are only noticeable for the $2.04\,\mathrm{g\,cm^{-3}}$ and the $3.48\,\mathrm{g\,cm^{-3}}$ systems from $4\,\text{Å}$ and beyond. Of these two, the lower-density system (Figure 4.12 a)) seems to have a more liquid-like PDF for the M-Q process than for the U-Q process, contrary to the PDF for the higher-density system (Figure 4.12 c)) which seems to be more liquid like for the U-Q proces. A detailed study of liquid-like structures for boron nitride is beyond the scope of this work since our particular interest resides in the determination of thermodynamic functions for the amorphous state. Therefore, we shall stick with our U-Q approach to simulate the boron-nitrogen system.

In order to compare our obtained supercells with those reported by the experimental works of Hong *et al.* [78] and Grigoriew and Leciejewicz [151] and the simulation results of McCulloch, McKenzie, and Goringe [90], the reduced Pair Distribution Function (rPDF or $G(r)$) was calculated and is shown in Figures 4.13. It is important to stress out that density determination of the samples is not reported in neither experimental works of Figure 4.13a and this may be one possible reason for the discrepancies between our $G(r)$'s and theirs.

Moreover, Grigoriew and Leciejewicz [151] reported there existed crystalline admixtures in their samples, making the $G(r)$'s comparison even harder to interpret. The reported rPDF for the amorphous structure of McCulloch, McKenzie, and Goringe [90] is shown Figures 4.13b; the discrepancies between our simulation and theirs are possibly due to their M-Q approach and a relatively small sized supercell (64 total number of atoms).

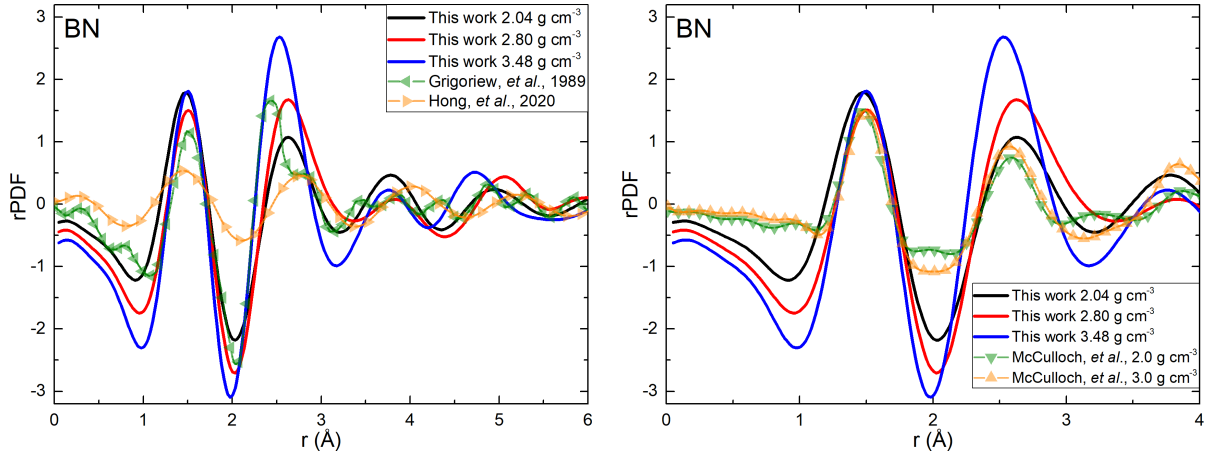

(A) rPDF for our three samples of a-BN compared to the reported by the experiments of Hong *et al.* [78] and Grigoriew and Leciejewicz [151]. Crystalline admixtures were reported to be contained in the samples of Ref. [151]. The experimental densities are not reported in neither work.

(B) rPDF for a-BN compared to the one reported by the simulations due to McCulloch, McKenzie, and Goringe [90]. Their M-Q method does not produce significant changes between their two studied densities. Our U-Q method does reflect structural differences for distances beyond 2 Å.

FIGURE 4.13. Reduced Pair Distribution Function, rPDF for our three amorphous BN densities studied and those reported a) experimentally in Refs. [78, 151] and b) simulationally in Ref. [90]

The partial PDFs of Durandurdu [92, 152] are shown respectively in Figures 4.14. Comparing Durandurdu's results for the N-N and B-B partial PDFs of his samples, it can be noted that in his simulated structures there are less N-N and B-B bonds than in ours. One possible explanation of this is that he performed molecular dynamics up to temperatures ranging from $5500\,\mathrm{K}$ [152] to $8500\,\mathrm{K}$ [92], reducing the possibility for the formation of these bonds due to the extremely high reached temperatures that caused the breaking of the diatomic molecules.

Moreover, traces of ordered phases are presented as sharp peaks beyond $3\,\text{Å}$ in Durandurdu's results. One possible explanation is that he used a crystalline stable atomic arrangement as the beginning structure for his simulation, leading to a deficient production of a fully amorphous phase throughout the sample, even the high temperatures reached. This is why we believe our U-Q method produces better amorphous structures than the traditional M-Q methods.

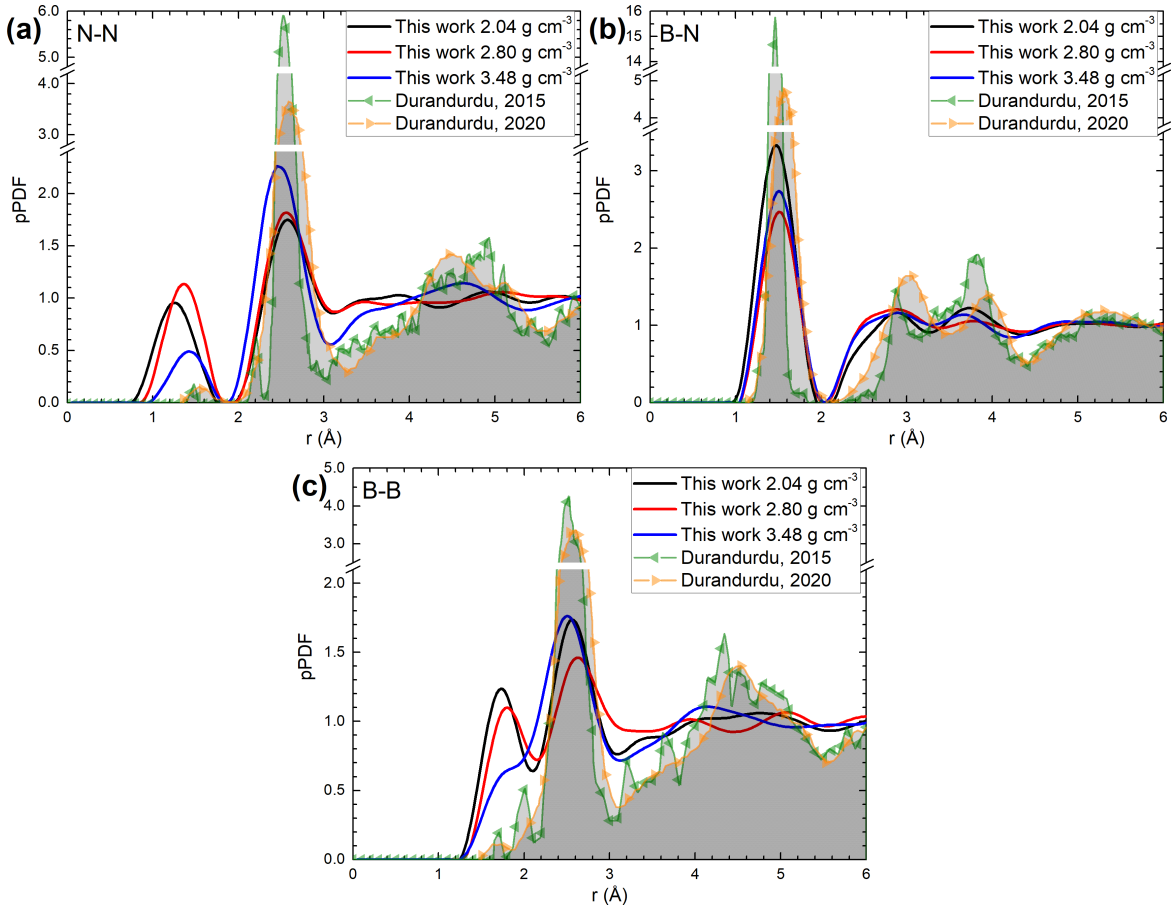

FIGURE 4.14. a) N-N, b) B-N, and c) B-B partial PDFs for a-BN compared to the ones reported by Durandurdu [92, 152]. The tall first peaks and the general sharply form of his partial PDFs indicate that the initial structure for his MD process may not be the adequate to generate amorphous samples.

4.3.2 Vibrational Density of States

The next step was to determine the vDoS for the three amorphous samples, these results are shown in Figure 4.15.

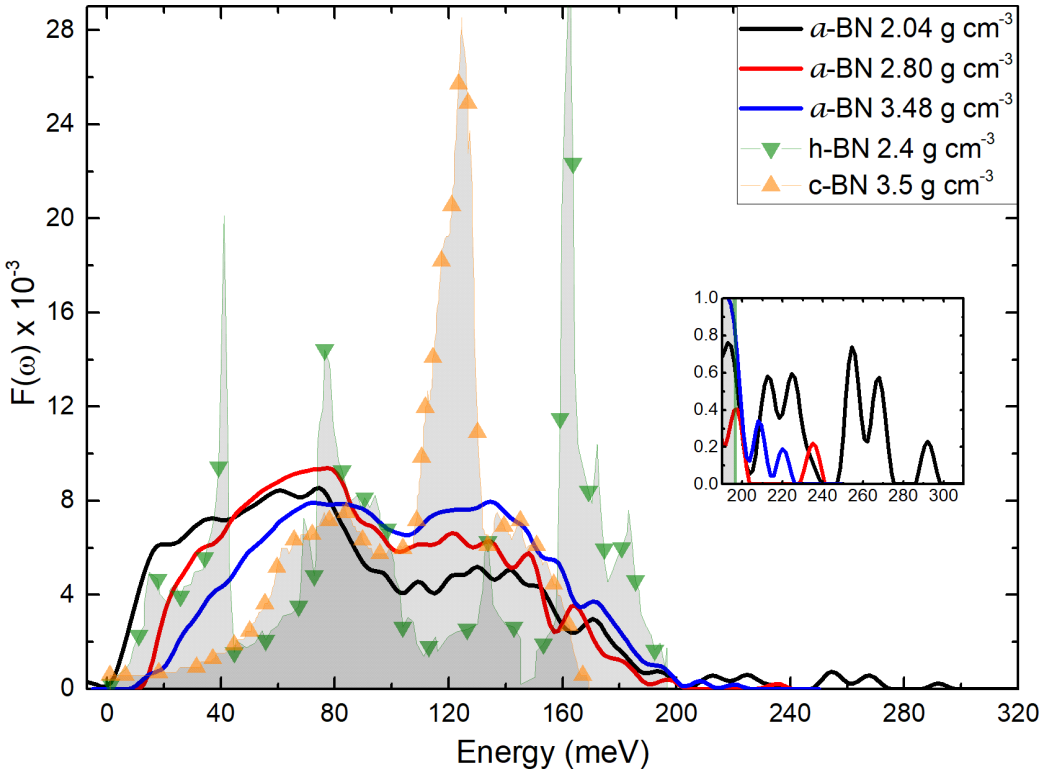

FIGURE 4.15. vDoS for generated a-BN for the three densities and a comparison to those calculated for the crystalline structures h-BN [153] and c-BN [154]. The inset shows a zoomed-in vision of the interval $200\,\mathrm{meV}$ to $300\,\mathrm{meV}$; in such range vibrational modes for the crystalline structures are absent, whereas there are some high-frequency modes for the three amorphous structures.

The vDoS of the three amorphous samples develop a larger concentration of low-frequency modes whereas the high frequency modes almost disappear. Those low frequency modes are located around $80\,\mathrm{meV}$ with a timid attempt to rescue some of the high frequency modes of the material at about $140\,\mathrm{meV}$; nowadays it is believed that this is a common occurrence in the transition from crystalline to amorphous. The frequency modes above $240\,\mathrm{meV}$ are present for the $2.04\,\mathrm{g\,cm^{-3}}$ but absent for the $2.80\,\mathrm{g\,cm^{-3}}$ and $3.48\,\mathrm{g\,cm^{-3}}$ densities (see inset of Figure 4.15). This is a consequence of the difference in the interatomic N-N and B-B distances (see Figures 4.14 a) and c)), shorter for the $2.04\,\mathrm{g\,cm^{-3}}$ system than for the $3.48\,\mathrm{g\,cm^{-3}}$ system; the shorter the distance the higher the vibration energy.

4.3.3 Thermodynamic functions

Once the vDoS is calculated, the thermodynamic functions of internal energy (eq. (3.9)) and constant volume specific heat (eq. (3.10)) may be determined. Both thermodynamic functions are shown in Figure 4.16. Because of the extensive nature of these properties, an intensive alternative was used in order to compare the three samples: the internal energy was divided by the number of atoms, n, in each cell (216 atoms for $2.04\,\mathrm{g\,cm^{-3}}$ and $2.80\,\mathrm{g\,cm^{-3}}$, and 256 atoms for $3.48\,\mathrm{g\,cm^{-3}}$); and the specific heat was divided by the Dulong-Petit law ($3N_Ak_B$). As is shown in the inset of Figure 4.16(b), the c_v behavior of our amorphous samples at low-intermediate temperatures does not follow the Debye T^3 law, just as expected for an amorphous material.

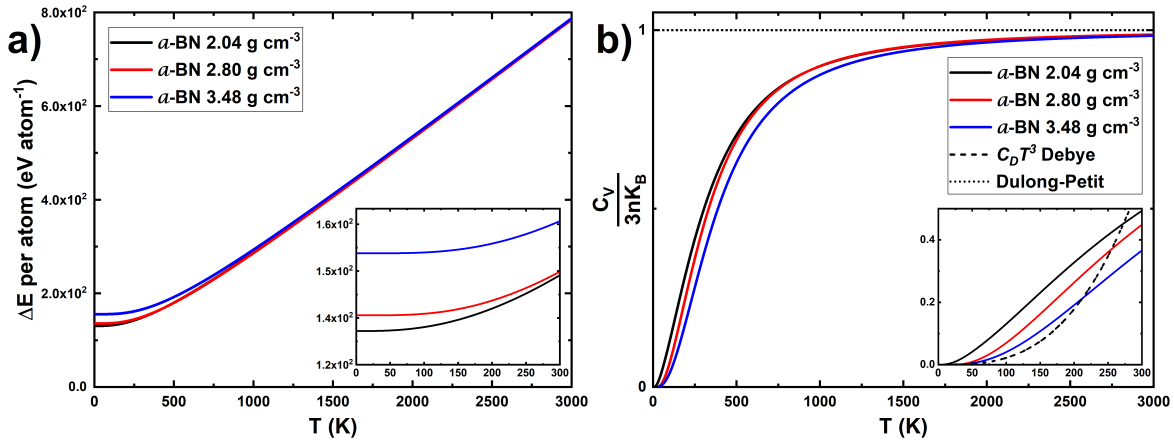

FIGURE 4.16. a) Calculated ΔE and b) C_v for the three a-BN samples. The results in b) for the C_v are scaled by the Dulong-Petit law ($3N_Ak_B$) such that $C_D = C_v/3N_Ak_B$. The inset shows the (0 K, 300 K) interval in both a) and b). As expected, the non-Debye T^3 behavior for the amorphous samples is shown in the inset in b)

4.3.4 Discussion

According to the PDFs, the amorphous samples constructed by the U-Q approach yield similar local distributions for the first coordination shell compared to our M-Q method, discrepancies however begin to occur from the second coordination shell at about 2.5 Å. Moreover, our U-Q simulations show important discrepancies in the atomic arrangement of the generated structures by M-Q approaches followed by other authors. Both theoretical and experimental studies are required to elucidate the existence for liquid-like features in the structure of amorphous boron nitride systems.

Nevertheless the vibrational spectra for the amorphous phase of the three samples are localized almost entirely within the same energy range as two of the crystalline phases, the existing high-energy modes for the amorphous structures are indicative for the intrinsically different local atomic arrangements and therefore different types of hybridization of boron and nitrogen. On the other side, the increment in the low-frequency modes for the lowest-density ($2.04\,\mathrm{g\,cm^{-3}}$) amorphous structure produces an increment in the intermediate-temperature-range specific heat. A more detailed study of the electronic structure of these amorphous systems that helps elucidate the density-hybridization-properties relation is underway.

This page intentionally left blank

5 Conclusions to Part I and Future work

In this work, a metallic solid solution (gold-silver), a metallic compound (copper-bismuth), and a semiconducting alloy (boron-nitrogen) were studied by means of first-principles calculations and some important properties were determined for each one. As was mentioned in the introduction, the three alloys do not have anything in common, however the main objective of this work was to explore different methods in the simulation of alloys in the quest to find one method which incorporates the atomic local environment within the material, bearing the supposition that this plays an important role in determining the macroscopic properties of condensed matter.

In particular, for the Au_xAg_{100-x} alloy, our approach to simulate alloyed supercells produced a very good approximation to the description of a thermodynamic property such as the electronic contribution to the specific heat without the necessity of invoking new concepts; our results may be improved by taking into account phononic contributions, however this gives hope that a simple but efficient method for the simulation of alloys is plausible. For the CuBi alloy, the increase of the electronic density of states at the Fermi level for the amorphous system with respect to the crystalline one has the consequence of the increment of the critical superconducting temperature, this phenomenon is also observed in pure bismuth but more work is needed for the study of superconducting amorphous materials from first-principles. Finally, for the BN system it was shown that the structural arrangement for the amorphous structure strongly depends on the maximum reached temperature in the simulation processes to obtain those disordered systems, although more simulations are needed, our amorphization method correctly describes the well-known deviations for the lattice specific heat of crystalline systems.

The quest for the proposal of a better methodology to simulate alloys is far from being completed. However, the knowledge acquired during this work by including intrinsically different systems has set some bases in which a new methodology may be formulated in the future.

This page intentionally left blank

Part II

Bismuth

This page intentionally left blank.

6 Introduction

It was already stated in Section 1.2 that bismuth has intriguing superconducting properties, whether alloyed or in its elemental form. Following the brief discussion of that Section, Part II of this thesis reports our *ab initio* investigations of superconductivity in pure crystalline bismuth under three different circumstances: i) the compressed Bi-I structure, ii) the bilayered structure, and iii) the under-pressure phases.

The work reported in this Part II was carried out within the DFT framework (Section 2.1) using the DMol^3 code from the Materials Studio software (subsection 3.1.1). Superconductivity in pure bismuth is studied under the BCS theory (Section 2.5) by means of the *à la* Mata-Pinzón *et al.* approach (subsection 3.3.6) and our calculated eDoS (subsection 3.3.4) and vDoS (subsection 3.3.5).

6.1 Bismuth

Bismuth is a semimetal with the electronic configuration $[\mathrm{Xe}]\,4\mathrm{f}^{14}5\mathrm{d}^{10}6\mathrm{s}^{2}6\mathrm{p}^{3}$ that crystallizes in a rhombohedral structure which is known as the Bi-I or the Wyckoff structure [155], (named after R. W. G. Wyckoff who first determined the currently accepted lattice parameters). The Wyckoff structure, stable at ambient temperature and pressure, almost has a simple cubic symmetry but ends up having bilayered structures, stacked in a ABCABC. . . pattern lying perpendicular to the $[1\ 1\ 1]$ crystallographic direction and hold together by van der Waals forces (see Figure 6.1a).

Superconductivity is present in a vast number of bismuth-based alloys (Section 1.2) and it has been hypothesized that "the electron configuration around the Bi atom itself is of prime importance" [66], becoming necessary to study Bi in its pure form in order to also understand the superconducting mechanisms bismuth contribute into the alloys. Since Bi was first predicted to be a superconductor below $1.3\,\mathrm{mK}$ in its pure crystalline form [63] and was later verified to be $0.53\,\mathrm{mK}$ [64], the necessity and relevance of including crystalline Bi in our investigation in Part II of this thesis is evident.

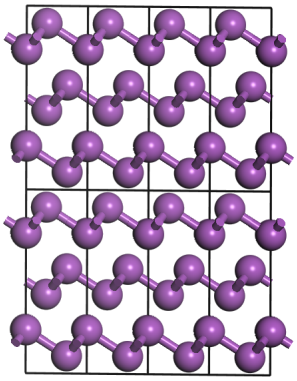

(A) Sphere representation of the Wyckoff structure in which a $4 \times 1 \times 2$ replication of the unit cell is shown. The sticks between some spheres are drawn to emphasize the bilayered structure.

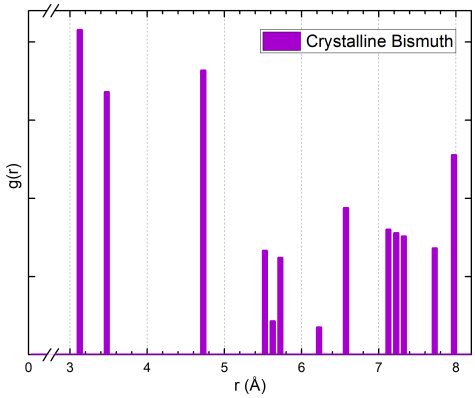

(B) PDF for crystalline Bismuth in the Wyckoff phase. The first two peaks are located at $3.11\,\text{Å}$ and $3.45\,\text{Å}$, which correspond to intra and interlayer nearest-neighbor distances.

FIGURE 6.1. a) Bismuth Wyckoff structure and b) its corresponding PDF.

6.1.1 Phase diagram

The temperature-pressure phase diagram of bismuth has changed since the first studies of Bridgman [156–158]. The current accepted version is that shown in Figure 6.2, which was obtained from linear and quadratic fits to the reported experiments of Klement, Jayaraman, and Kennedy [159].

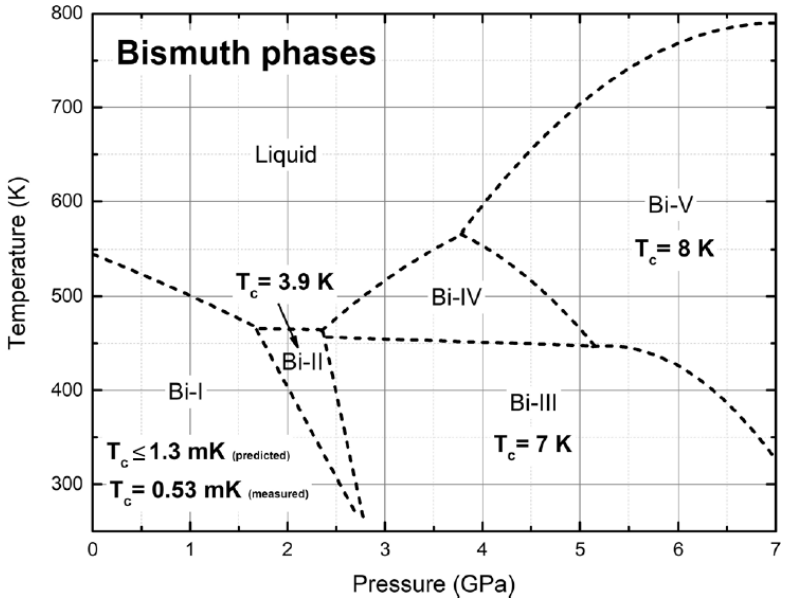

FIGURE 6.2. Bismuth Phase Diagram reported in Ref. [160], adapted from Ref. [159] for which broken lines were obtained by linear and quadratic fits to their experimental data. The measured [64, 65] and predicted [63] critical superconducting temperatures are shown for the phases known to be superconducting.

There has been a lot of controversy around the validity of this phase diagram since some authors [161–163] reported the existence of other phases within the Bi-III region, whereas other authors disproved their existence [159, 164, 165]. Nevertheless, hereinafter we shall consider the phase diagram of Figure 6.2 as valid and use it for our bismuth study.

The difficulties involving an accurate determination for the Bi-III structure rely on its complexity. In the early and mid 1990's, using then unprecedented-quality x-ray diffraction methods on Sb-II and Bi-III [165, 166], Chen, Iwasaki, and Kikegawa proposed a primitive tetragonal cell with 10 atoms and space group P4/n with $a = b = 8.659\,\text{Å}$ and $c = 4.238\,\text{Å}$ for Bi-III at $3.8\,\mathrm{GPa}$. Although this structure provided a good fit to the x-ray positions, it would require an "unphysical" volume increase of approximately 2% at the Bi-II $\rightarrow$ Bi-III transition, suggesting the need for the structure to be more complex [167, 168].

In the late 1990's, a new crystal structure type was discovered for Ba-IV at room temperature and $12.1\,\mathrm{GPa}$ by Nelmes *et al.* [169]. These structures are composed of two interpenetrating cells: a "host" tetragonal structure containing "guest" chains that extend along one axis of the host structure; the host and the guest structures are incommensurate with each other [169]. This type of incommensurate host-guest complex structure [170] was also found in Sr, phase V, above $45\,\mathrm{GPa}$ [171]. In this manner, based on the incommensurate-structure hypothesis, McMahon, Degtyareva, and Nelmes [167] and Degtyareva, McMahon, and Nelmes [168] proposed that Bi-III also present this kind of structure. Since then, several investigations have considered the incommensurate structure a reality for the Bi-III phase [167, 168, 172, 173].

Going back to the under-pressure phases of bismuth, it is seen that at room temperature, Bi manifests a "high-pressure transition sequence" of structural changes [65, 174]: Bi-I $\rightarrow$ Bi-II (monoclinic, $C2/m$) at about $2.5\,\mathrm{GPa}$, Bi-II $\rightarrow$ Bi-III (host-guest structure, $P1$) at about $2.7\,\mathrm{GPa}$, and Bi-III $\rightarrow$ Bi-V (bcc, $Im\overline{3}m$) at about $7.7\,\mathrm{GPa}$. There also exist Bi-IV (orthorhombic, $Cmca$), a high-pressure, high-temperature phase which is above $450\,\mathrm{K}$ and in the $(2.5\,\mathrm{GPa}, 5\,\mathrm{GPa})$ pressure interval. It is important to notice that this transition sequence also is presented for Sb and As at different pressures [174].

This page intentionally left blank

7 Methods and Results

In this chapter, the electronic and phononic energy spectra calculated for compressed, bilayered, and under-pressure strucures of pure bismuth are employed to infer changes its superconducting critical temperature T_c, which is determined *via* the *á la* Mata-Pinzón *et al.* approach (subsection 3.3.6) and the calculation of the eDoS (s.s. 3.3.4) and vDoS (s.s. 3.3.5) for the three mentioned cases. The BCS Theory of Superconductivity (Section 2.5) and the Density Functional Theory (Section 2.1), as implemented in the DMol^3 code (s.s. 3.3.1) of the Materials Studio software (s.s. 3.1.1), are the frameworks in which all the calculations of Part II of this thesis are founded.

Electronic treatment for Bi on DMol^3

The electronic parameters for the *ab initio* calculations on bismuth are the same as those stated in subsection 3.3.1, with the exception that the real-space atomic cutoff radius is $6.0\,$Å for this Part II of the thesis. The parameters and processes for the eDoS and VDoS functions are the same as those stated in subsections 3.3.4 and 3.3.5, respectively.

7.1 Compressed structures (Hinojosa-Romero *et al.* [175])

In this part of the work, the effects of compressed bismuth in its electronic and vibrational densities of states are studied. The important characteristic from this analysis is that the Wyckoff structure was conserved during the compression of the supercell, i.e. our study did not involve phase changes as in Figure 6.2. The procedure was as follows: The original crystalline structure (Fig. 6.1a) is represented in this part of the study by a supercell containing 64 atoms with density $9.81\,\mathrm{g\,cm^{-3}}$ and interatomic distances equal to those of Bi-I (Fig. 6.1a). The supercells needed for this work were obtained by modifying the size of the lattice edges keeping constant the fractional atomic positions; this process was followed to construct 18 different supercells: 14 compressed, 3 expanded, and 1 unaltered. Single-point energies were calculated for all the modified supercells so the pressure at which these structures are simulated can be estimated; the details for these calculations are given below and reported in Table 7.1.

7.1.1 Pressure determination

From the calculated single-point energies, one can determine the binding energy (BE) [32, 100] of each supercell as a function of the volume. These results are shown in Figure 7.1 where a fourth-order polynomial fit to the data points was used:

$$BE(V) = A_0 + A_1 V + A_2 V^2 + A_3 V^3 + A_4 V^4$$

where $A_0 = 2879.507\,78$, $A_1 = -4.990\,92$, $A_2 = 3.076\,80 \times 10^{-3}$, $A_3 = -8.566\,60 \times 10^{-7}$, and $A_4 = 9.1181 \times 10^{-11}$; units for BE are eV and for V, Å^3.

The negative of the slope of the adjusted curve for BE at a given volume V corresponds to the pressure at which the structure with that volume would be [96, 100]:

$$P = -\frac{\partial(BE)}{\partial V}$$

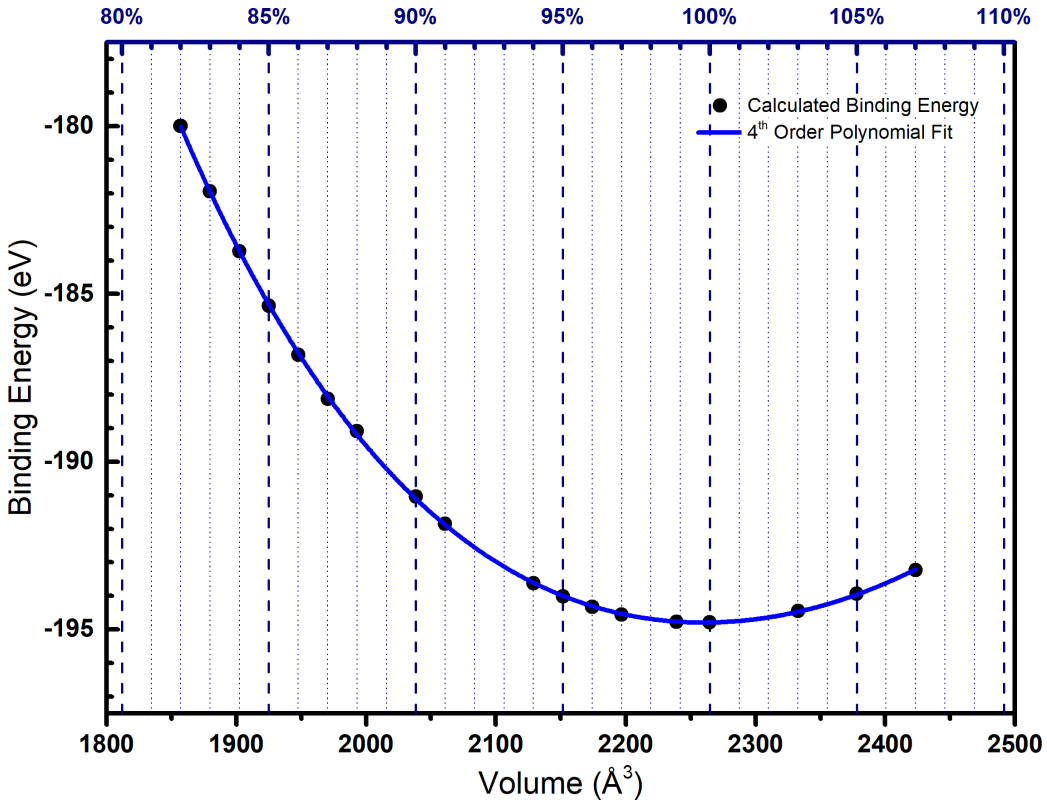

FIGURE 7.1. Binding energy as a function of volume of the 18 supercells constructed (black dots). Solid blue line represents the fourth-order polynomial fit to our results. The percentage values of compression and expansion are shown in the top axis.

It is seen from the fourth-order adjustment that the original supercell with lattice parameter of the Wyckoff structure (labeled as 100%) corresponds to a simulated pressure of $-0.07\,\mathrm{GPa}$. This means that, within the DFT calculation accuracy, the atomic positions do not yield the lowest-energy configuration supercell. However, the supercell's energy is close enough to the *minimum-minimorum* value such that the 100% Bi structure can be chosen as our stable and representative structure for the Bi-I phase.

TABLE 7.1. Binding energy as function of pressure and percentage of volume. The pressure was determined as the tangent to the curve depicted in Figure 7.1.

Volume $\left[\text{Å}^3\right]$	Volume $[\%]$	Binding Energy $[\mathrm{eV}]$	Pressure $[\mathrm{GPa}]$
2423.38	107	-193.23047	-3.11
2378.08	105	-193.93686	-2.23
2332.79	103	-194.44684	-1.38
2264.84	100	-194.79269	-0.07
2239.02	99	-194.77677	0.45
2196.89	97	-194.55493	1.37
2174.23	96	-194.32712	1.90
2151.60	95	-194.01702	2.46
2128.95	94	-193.61881	3.06
2061.00	91	-191.84727	5.11
2038.35	90	-191.04612	5.89
1993.06	88	-189.08644	7.62
1970.42	87	-188.12609	8.58
1947.76	86	-186.81098	9.61
1925.11	85	-185.35005	10.71
1902.46	84	-183.73161	11.89
1879.81	83	-181.94591	13.15
1857.17	82	-179.98491	14.49

Herein after we shall only focus in the Wyckoff and the 15 compressed structures for the calculation of their eDoS and vDoS.

7.1.2 eDoS

The electronic density of states, represented in Figures 7.2 is calculated from the determination of the energies in the DFT calculations. It is observed that the number of states at the Fermi level decreases noticeably in going from a pressure of $7.62\,\mathrm{GPa}$ to a value of $8.58\,\mathrm{GPa}$; this is plotted in Figure 7.3. Since this pressure is close to 7.7GPa associated to the observed experimental phase change Bi-III $\rightarrow$ Bi-V at room temperature (see subsection 6.1.1), we believe that the change in eDoS may be associated to the need of the Wyckoff-like structure to relax to a different, more stable phase.

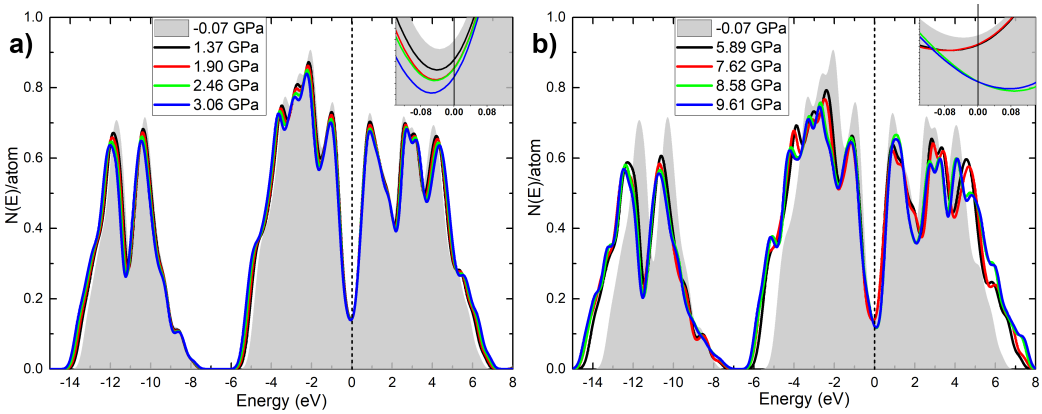

FIGURE 7.2. eDoS for the Wyckoff and 9 selected compressed supercells. Curves for pressures up to $3.06\,\mathrm{GPa}$ are shown in a), whereas curves for pressures from $5.89\,\mathrm{GPa}$ to $9.61\,\mathrm{GPa}$ are shown in b).

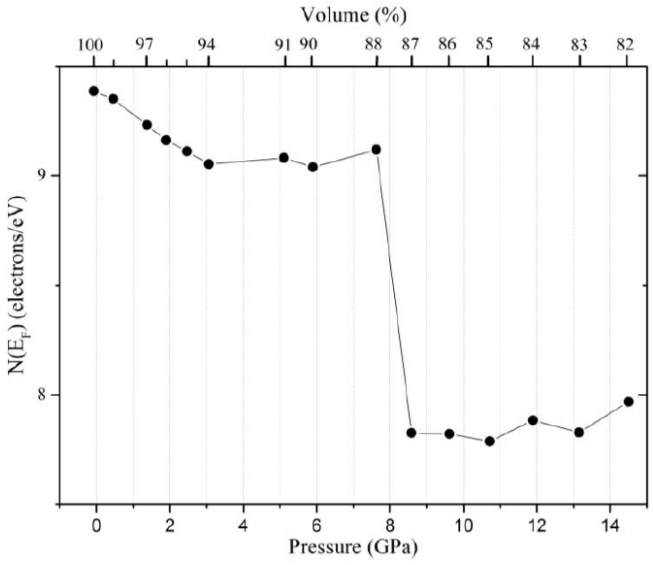

FIGURE 7.3. eDoS at Fermi level as a function of the calculated pressure for the Wyckoff and the 14 compressed supercells.

7.1.3 vDoS

Two interesting and subtle features appear in the vDoS curves (Figures 7.4). The first feature appears around $9\,\mathrm{meV}$, in which the shoulder-like form evolves into a peaked structure when going from the structure at $1.9\,\mathrm{GPa}$ to that at $2.46\,\mathrm{GPa}$ (see inset of Figure 7.4 a)). The second feature appears between $4.0\,\mathrm{meV}$ and $5.5\,\mathrm{meV}$, in which the peaked structure evolves into a bimodal-form when going from the structure at $5.89\,\mathrm{GPa}$ to that at $7.62\,\mathrm{GPa}$ (see inset of Figure 7.4 b)).

Recalling the bismuth phase diagram at ambient temperature (Section 6.1.1 and Ref. [159]), the high-pressure T_cs are: $3.9\,\mathrm{K}$ for Bi-II (at $2.5\,\mathrm{GPa}$), $7.2\,\mathrm{K}$ for Bi-III (at $2.7\,\mathrm{GPa}$), and $8.5\,\mathrm{K}$ for Bi-V (at $7.7\,\mathrm{GPa}$). So, as in the eDoS case, the observed subtle changes in the vDoS at the above-mentioned pressures may be an indication for the need of the Wyckoff structure to change its atomic arrangement and produce a more stable structure.

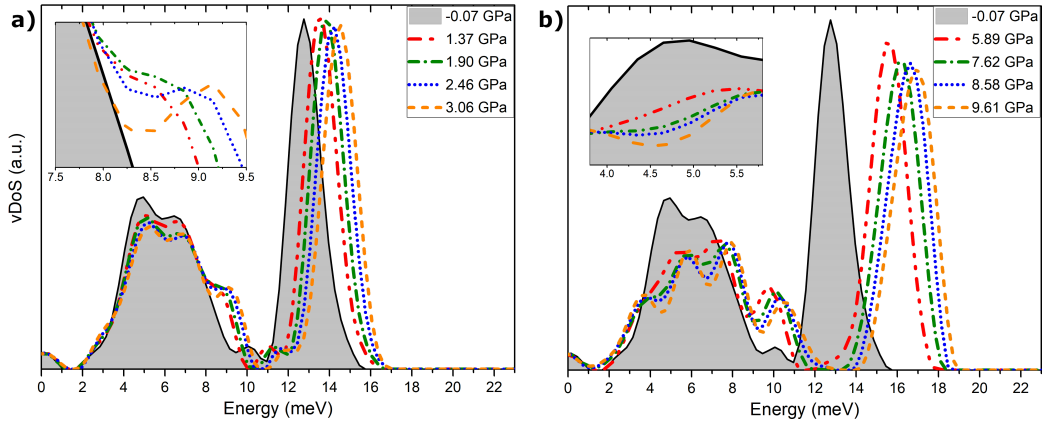

FIGURE 7.4. vDoS for the Wyckoff and 9 selected compressed supercells. Curves for pressures up to $3.06\,\mathrm{GPa}$ are shown in a), whereas curves for pressures from $5.89\,\mathrm{GPa}$ to $9.61\,\mathrm{GPa}$ are shown in b). The curve for the Wyckoff structure is shown as reference in both a) and b). The insets show interesting-feature zones (see text)

7.1.4 Discussion

Our calculations seem to indicate that, for pressures in the vicinity of possible phase transitions, changes in the eDoS and the vDoS may indicate the tendency of the Wyckoff structure to relax into different more stable structures. However, the evidence is not definite since there is no unequivocal way to correlate these changes to structures that may be unstable. Also, the diminishing eDoS at the Fermi level as pressure increases is an indication that the superconducting critical temperature should decrease as well if the Wyckoff structure remained unchanged. This is in clear contradiction with the measured values shown in Figure 6.2; thus the next step is to study the under-pressure phases, as will be done in Section 7.3.

7.2 Bilayers (Hinojosa-Romero *et al.* [176])

As was mentioned in Chapter 6, the bilayers in the Wyckoff structure lie perpendicular to the $[1\ 1\ 1]$ crystallographic direction, thus the usually reported names of Bi(111) surface, Bi bilayers, or bismuthene (in analogy to graphene, the individual layers of carbon). These low-dimensional material has been the subject of recent investigation [177–181] as they are an example of non-carbon low-dimensional material predicted to be a topological insulator [182–185]. However, based on the fact that superconductivity is observed in several bismuth alloys (ref. [66] and Sections 1.2 and 4.2) and phases (Section 7.3), for this investigation it is proposed that Bi(111) bilayers may also display superconductivity.

7.2.1 Supercell construction

The procedure for the construction of the bismuthene supercell is sketched in Figure 7.5. Given a 240-Bi-atom supercell with the Wyckoff structure (Fig. 6.1a), three supercells exclusively formed by the A-labeled bilayers were constructed. The interlayer distance d between these isolated Bi(111) structures in our slab model was set to 5 Å, 10 Å, and 20 Å, one interlayer distance per constructed supercell, each one henceforth respectively named as Bilayer (5), Bilayer (10), and Bilayer (20).

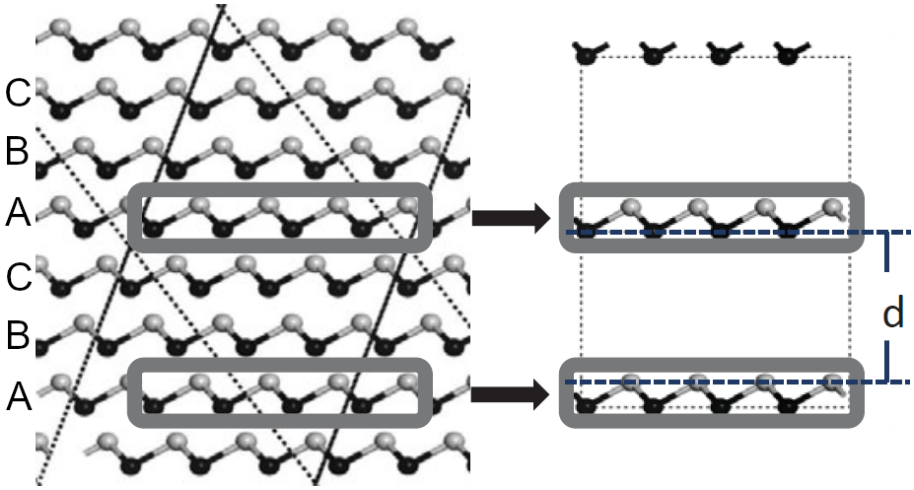

FIGURE 7.5. Wyckoff structure showing the bilayers of bismuth. Notice the ABCA... stacking order. The construction of the supercell for this study is depicted in the image on the right. The distance d corresponds to interlayers' vacuum.

7.2.2 eDoS and vDoS

The calculated eDoS (subsection 3.3.4) for the three bilayers are shown in Figures 7.6 along with the comparison of the eDoS for the bulk Wyckoff phase depicted as the shaded-area curve. The eDoS at the Fermi level values for the Bilayer (10) system: 0.48, and the Bilayer (20) system: 0.47 are almost identical; moreover the general form of the entire eDoS does not shown appreciable changes between both models. This is an expected result since the bilayers are sufficiently far apart for the electronic density of the bottom layer interacts with the top layer. An interesting case is the Bilayer (5) system since, for an interlayer vacuum separation of $5\,$Å, both bilayers within the supercell interact through their electronic density.

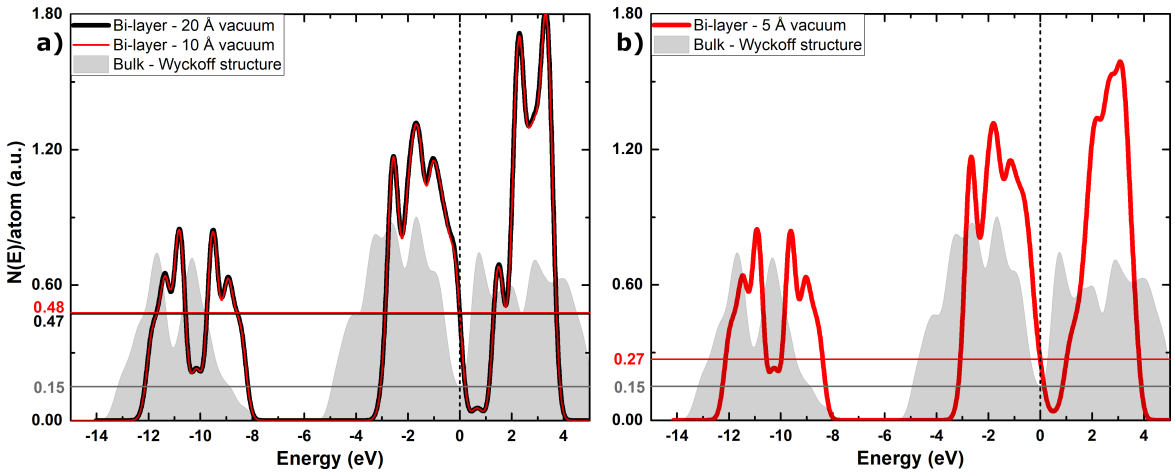

FIGURE 7.6. Comparison between the Wyckoff structure (shaded area) and our slab model with (a) $d = 10\,$Å (solid black line) and $20\,$Å (solid red line), and (b) $d = 5\,$Å (solid red line) of interlayer vacuum. The Fermi level is shown as the vertical dotted black line and horizontal solid lines are a guide to the eye for the eDoS at the Fermi level.

The calculated vDoS (subsection 3.3.5) for the three bilayers are shown in Figures 7.7 along with the comparison with the bulk Wyckoff structure. The energy pseudo-gap at $10\,\mathrm{meV}$ for the bulk structure becomes, for the three bilayers, a real gap of about $6\,\mathrm{meV}$ that separates low-frequency form high-frequency modes. This bimodality in $F(\omega)$ is typical of bilayered structures and the fact that it is almost observed in bulk Wyckoff shows its essential layered structure. An interesting feature of the vDoS for Bilayer (10) and Bilayer (20) structures is the appearance of a shoulder-like form at about $16\,\mathrm{meV}$ that is absent in the Bilayer (5) and the bulk Wyckoff structures; thus, the high-frequency peaks can be identified with principally intralayer atomic vibrations.

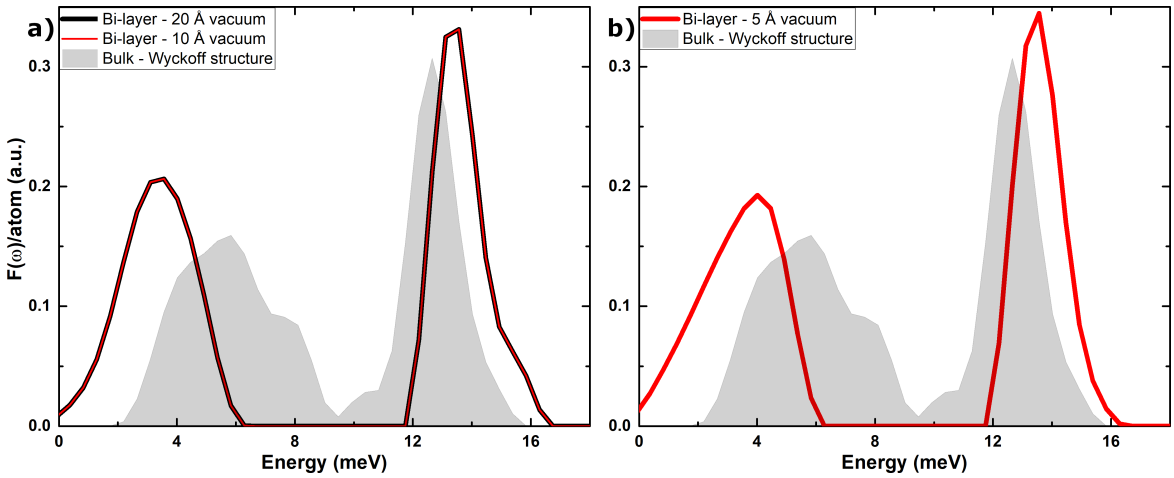

FIGURE 7.7. Comparison between the Wyckoff structure (shaded area) and our slab model with (a) $d = 10\,\text{Å}$ (solid black line) and $20\,\text{Å}$ (solid red line), and (b) $d = 5\,\text{Å}$ (solid red line) of interlayer vacuum.

The eDoS at the Fermi level $N(E_F)$ and Θ_D obtained for the Wyckoff structure and our slabs models are reported in Table 7.2.

TABLE 7.2. $N(E_F)$, Θ_D, η, μ, and T_c (in K) for the Wyckoff and bilayered structures obtained from our constructed # atoms supercells and their calculated eDoS and vDoS.

Structure	# atoms	$N(E_F)$ [a]	Θ_D [b]	η [c]	μ [d]	T_c [e]
Wyckoff	240	0.15	134.2	1.00	1.00	0.0013
Bilayer (5)	72	0.27	104.3	1.80	0.78	0.08
Bilayer (10)	72	0.48	104.3	3.20	0.78	2.61
Bilayer (20)	72	0.47	104.3	3.13	0.78	2.42

[a] Notation: $N^W(E_F)$ for Wyckoff and $N^L(E_F)$ for bilayers.

[b] Notation: Θ_D^W for Wyckoff and Θ_D^L for bilayers.

[c] From eq. (7.1)

[d] From eq. (7.2)

[e] From eq. (7.3). Notation: T_c^W for Wyckoff and T_c^L for bilayers.

7.2.3 Calculation of the T_c

Following the method of Mata-Pinzón *et al.* [63] described in subsection 3.3.6, we identify the material R as the bulk Wyckoff structure W, and the material Q as one bilayered form L. Thus, the identifications: $R \to W$ and $Q \to L$ in equations (3.4) to (3.8) produce:

$$\eta = \frac{N^L(E_F)}{N^W(E_F)} \tag{7.1}$$

from equation (3.6) for a bilayered-to-Wyckoff ratio of $N(E_F)$, and

$$\mu = \frac{\Theta_D^L}{\Theta_D^W} \tag{7.2}$$

from equation (3.7) for a bilayered-to-Wyckoff ratio of Θ_D.

Taking the reference value of $T_c^R \to T_c^W = 1.3\,\mathrm{mK}$, as determined from the calculations of Mata-Pinzón *et al.* [63], the superconducting critical temperature for each one of the bilayered structures is determined by equation (3.8) by changing $T_c^Q \to T_c^L$ as:

$$T_c^Q = T_c^L = \mu \, \left[T_c^W\right]^{1/\eta} \, \left[1.13\,\Theta_D^W\right]^{(\eta-1)/\eta}, \tag{7.3}$$

obtaining the critical temperatures for each Bilayer shown in Table 7.2.

7.2.4 Discussion

The bilayers of bismuth, being the basic structure of bulk bismuth, may display interesting properties when isolated. Here, it is proposed that this form of bismuth may present superconductivity and with the critical temperatures ranging from $0.08\,\mathrm{K}$ to $2\,\mathrm{K}$, depending on the interlayer separation. We find that for interlayer distances higher than $d = 5\,\text{Å}$, the properties of the layers are practically identical, which means that the interaction between them is practically negligible. Assuming that the Cooper pairing potential remains essentially unchanged in going from the bulk structure to the layer structure is a strong supposition; experiments shall prove us rigth or wrong.

7.3 The phases (Rodríguez *et al.* [160] and Valladares *et al.* [186])

Crystallographic data of the lattice parameters of the Bismuth phases considered in the present work are shown in Table 7.3 [160, 186]. For the approximation of McMahon *et al.* to the incommensurate structure of Bi-III, the host structure is indicated by "H", whereas the guest structure by "G".

TABLE 7.3. Lattice parameters for the five bismuth phases. The Bi-III structure, the incommensurate one, is reported from the work of Chen, Iwasaki, and Kikegawa [165], as well from the work of McMahon, Degtyareva, and Nelmes [167] and their proposed host(H)-guest(G) structure.

Phase	Unit Cell Parameters						Space Group	
	a Å	b Å	c Å	α °	β °	γ °	No.	Name
Bi-I [a]	4.55	4.55	11.86	90.00	90.00	120.00	166	$R\bar{3}m$
Bi-II [b]	6.65	6.09	3.29	90.00	110.37	90.00	12	$C2/m$
Bi-III [c]	8.66	8.66	4.24	90.00	90.00	90.00	90	$P4/m$
Bi-III [d]	8.52	8.52	4.16(H), 3.18(G)	90.00	90.00	90.00	1	$P1$
Bi-IV [e]	11.19	6.62	6.61	90.00	90.00	90.00	64	$Cmca$
Bi-V [f]	3.80	3.80	3.80	90.00	90.00	90.00	229	$Im\bar{3}m$

[a] Ambient temperature and pressure [174].

[b] Ambient temperature, pressure of 2.7 GPa, Ref. [174].

[c] Ambient temperature, pressure of 3.8 GPa, Ref. [165].

[d] Ambient temperature, pressure of 4.2 GPa, Ref. [167].

[e] Temperature of 465 K, pressure of 3.2 GPa, Ref. [187].

[f] Ambient temperature, pressure of 8.5 GPa, Ref. [174].

Bi-I

For the Wyckoff structure, Bi-I, we used a 6-atom crystalline cell that we multiply by $5 \times 4 \times 2$ to obtain a supercell with 240 atoms for the calculations of $N(E)$ and of $F(\omega)$. Thus, the supercell has the following lattice parameters: $a = b = 4.55$ Å and $c = 11.86$ Å and with $\alpha = \beta = 90°$ and $\gamma = 120°$, and the space group is R$\hat{3}$m, as reported in Table 7.3. Figure 7.8 is a representation where the bilayers are clearly indicated by white and black spheres.

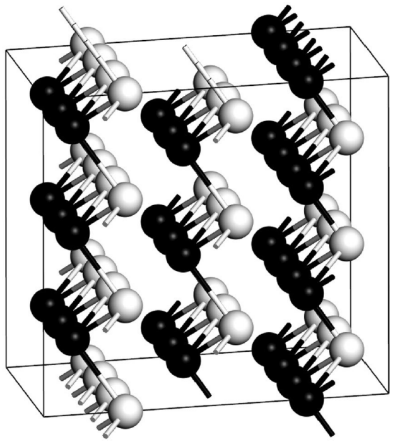

FIGURE 7.8. Spheres and sticks representation of the Wyckoff structure of bismuth as reported in Ref. [160]. Spheres are colored black and white just to show more clearly the bilayered structure. The bonds, represented by the sticks, correspond to a default distance of 3.45 Å.

Bi-II

The supercell used for our calculations of $N(E)$ and $F(\omega)$ has 240 atoms ordered in a C2/m space group with lattice parameters of $a = 6.65$ Å, $b = 6.09$ Å and $c = 3.29$ Å, with $\alpha = 90°, \beta = 110.37°$ and $\gamma = 90°$, consequence of a $4\times3\times5$ multiplication of the 4-atom unit cell. These data are registered in Table 7.3. The corresponding pressure for Bi-II structure is 2.7 GPa [174]. A representation of the corresponding cell is shown in Fig. 7.9 where the monoclinic structure can be observed, together with two (dark and light) distinct monoatomic layers displayed.

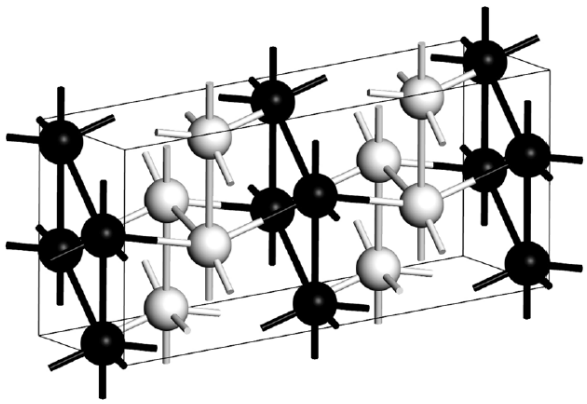

FIGURE 7.9. Spheres and sticks representation of the Bi-II structure as reported in Ref. [160] according to the data in Ref. [174]. Two different monoatomic layers (black and white spheres) can be observed.

Bi-III

Bismuth III is a low temperature phase that extends to pressures higher than 7 GPa, Fig. 6.2. Along with the controversies of the phase diagram in this region (subsection 6.1.1); this phase in particular has also been controversial since it was described first as a regular periodic cell [165], and nowadays it is considered as a host-guest incommensurate structure (see s.s. 6.1.1 and Refs. [167, 174]). Since an incommensurate structure is impossible to represent within a supercell approach, there have been attempts to propose representative commensurate periodic crystalline structures that supposedly would reflect, with some precision, the real structure [188]. This gave rise to two structures, one due to Chen and coworkers [165] (Fig. 7.10), the other due to McMahon and coworkers [167] (Fig 7.11). Later, Häussermann, Söderberg, and Norrestam proposed a commensurate approximation of a 3:4 host-guest ratio [172]. In this work we consider Chen's representation and, based on the 3:4 Häussermann approximation, we construct a commensurate one from McMahon's data and calculate its eDoS, vDoS and superconducting transition temperature. As we shall see, the structure proposed by Chen, Iwasaki, and Kikegawa leads to a T_c closer to experiment than ours.

The Chen supercell has 120 atoms, consequence of a $2 \times 2 \times 3$ multiplication of the 10-atom representative cell. Figure 7.10 is a representation where the tetragonal structure is illustrated. The lattice parameters at a pressure of $3.8\,\mathrm{GPa}$ were: $a = b = 8.66\,\text{Å}, c = 4.24\,\text{Å}$; $\alpha = \beta = \gamma = 90^\circ$ and the space group is P4/n21 (see Table 7.3, row: Bi-III [c]).

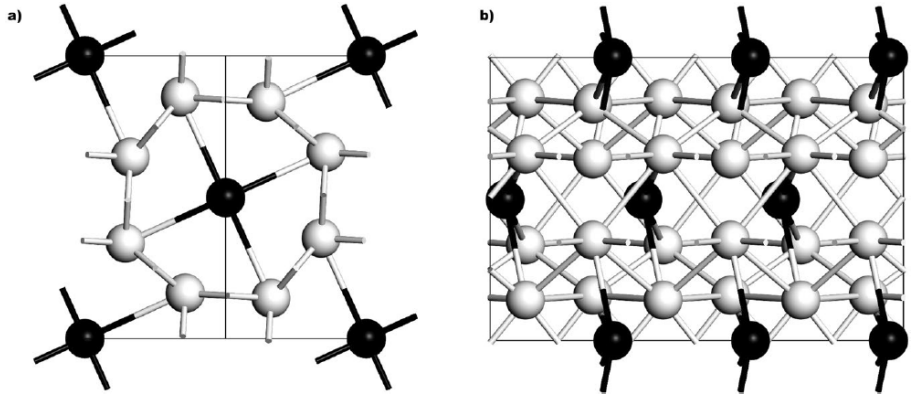

FIGURE 7.10. Spheres and sticks representation of the Bi-III structure as reported in Ref. [160] according to the data reported in Ref. Chen, Iwasaki, and Kikegawa [165]. a) The x-y plane of the structure. b) The horizontal in-the-plane axis is the z-axis of the structure.

Our proposed supercell has 128 atoms, consequence of a $2 \times 2 \times 1$ multiplication of our 32-atom representative cell shown in Fig. 7.11, resulting in the following lattice parameters: $a = b = 8.52\,\text{Å}, c_H = 4.2\,\text{Å}$ and $c_G = 3.1\,\text{Å}$ for the host and guest structures, respectively; $\alpha = \beta = \gamma = 90^\circ$ and the space

group is P1, at a pressure of $4.2\,\mathrm{GPa}$. The host structure is tetragonal with 8 atoms in its own unit cell (white spheres), whereas the guest structure is body centered tetragonal with two atoms in its own unit cell (black spheres) (see row Bi-III [d] of Table 7.3). Our basic 32-atom cell was then obtained from interpenetrating three host unit cells with four guest unit cell along the z-axis.

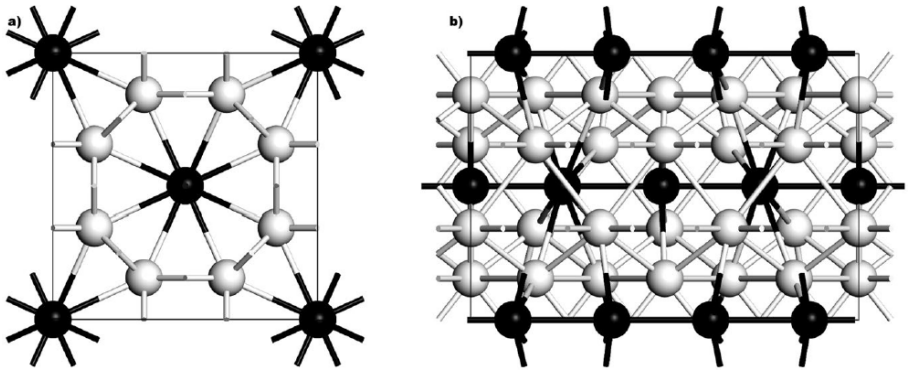

FIGURE 7.11. Our commensurate Bi-III 3:4 host-guest structure as reported in Ref. [160]. It is based on the incommensurate structure reported at $4.2\,\mathrm{GPa}$ in Ref. [167]. Host-structure spheres are colored white, whereas guest-structure spheres are black. a) The x-y plane of the structure. b) The horizontal in-the-plane axis is the z-axis of the structure.

Bi-IV

To construct the Bi-IV supercell, we use the experimental results by Chaimayo *et al.* [187]. They reported that, at 3.2 GPa and 465 K, the structure is orthorhombic (pseudo-tetragonal) with the $Cmce$ space group and the following lattice parameters: $a = 11.19\,\text{Å}, b = 6.62\,\text{Å}$ and $c = 6.61\,\text{Å}$ (see Table 7.3). Figure 7.12 represents this 16-atom structure with bilayers (white spheres) intercalated by gray and black monolayers. We constructed supercells by multiplying this 16-atom cell by the factor $4 \times 2 \times 2$ (256 atoms) to calculate $N(E)$ and $2 \times 2 \times 2$ (128 atoms) to calculate $F(\omega)$.

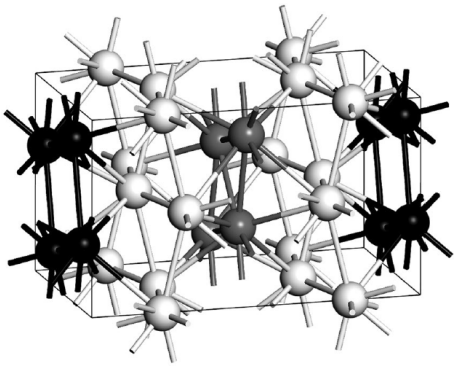

FIGURE 7.12. Crystalline 16-atom cell of Bi-IV as reported in Ref. [160] according to the data reported in Ref. [187]

Bi-V

The structure of Bi-V at $8.5\,\mathrm{GPa}$ is given by lattice parameters: $a = b = c = 3.80\,\text{Å}; \alpha = \beta = \gamma = 90^\circ$ and, as depicted in Figure 7.13, the structure is a body-centered cubic (white spheres) with the space group $Im\bar{3}m$. The supercells used have 250 atoms, consequence of a $5 \times 5 \times 5$ multiplication of the 2-atom unit cell (see Table 7.3).

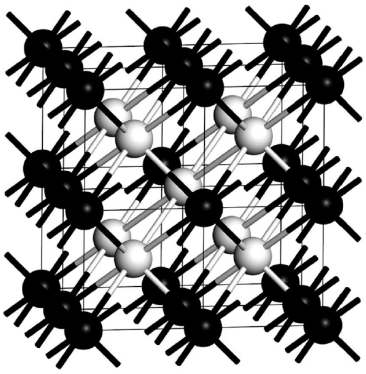

FIGURE 7.13. The body centered cubic structure of the Bi V phase as reported in Ref. [160] according to the data of Ref. [174]. The BCC can be seen with the aid the of white spheres.

Table 7.4 contains a summary of the parameters of the supercells employed for the bismuth phases.

TABLE 7.4. Parameters of the supercells employed for the simulation of the five bismuth phases.

Phase	Pressure [GPa]	Density [g/cm^3]	Supercell Multiplier	# atoms	$N(E_F)$ [a] $\left[\frac{\text{electron states}}{\text{eV * atom}}\right]$	Θ_D [b] [K]
Bi-I	0.0	9.80	$5 \times 4 \times 2$	240	0.15	134.2
Bi-II	2.7	11.6	$4 \times 3 \times 5$	240	0.50	115.5
Bi-III [c]	3.8	10.92	$2 \times 2 \times 3$	120	0.62	96.9
Bi-III [d]	4.2	12.25	$2 \times 2 \times 1$	128	0.45	144.4
Bi-IV	3.2	11.33	$4(2) \times 2 \times 2$	256 (128)	0.53	102.1
Bi-V	8.5	12.64	$5 \times 5 \times 5$	250	0.56	137.8

[a] Notation: $N^W(E_F)$ for Wyckoff and $N^L(E_F)$ for bilayers.

[b] Notation: Θ_D^W for Wyckoff and Θ_D^L for bilayers.

[c] Chen, Iwasaki, and Kikegawa [165].

[d] McMahon, Degtyareva, and Nelmes [167].

7.3.1 eDoS and vDoS

Once the supercells were constructed, the calculations of their eDoS (subsection 3.3.4) and vDoS (s.s. 3.3.5) were done. Our results for each phase studied are presented next.

Bi-I

Since the Bi-I phase is taken as the reference phase, the $N(E)$ and $F(\omega)$ graphs for this phase will be constantly reproduced in the figures where comparisons with the other phases are made. $N(E_F)$ for this phase is 0.15 electrons per atom and the Debye temperature is $134.2\,\mathrm{K}$.

Bi-II

The results obtained for the eDoS are given in Figure 7.14 a) where comparison is made with the results obtained for the Wyckoff phase. $N(E_F)$ is 0.50 electrons per atom. In Figure 7.14 b), a comparison between $F(\omega)$ for Bi-I and Bi-II phases is presented. The calculation for the Debye temperature resulted in $115.5\,\mathrm{K}$ for this phase.

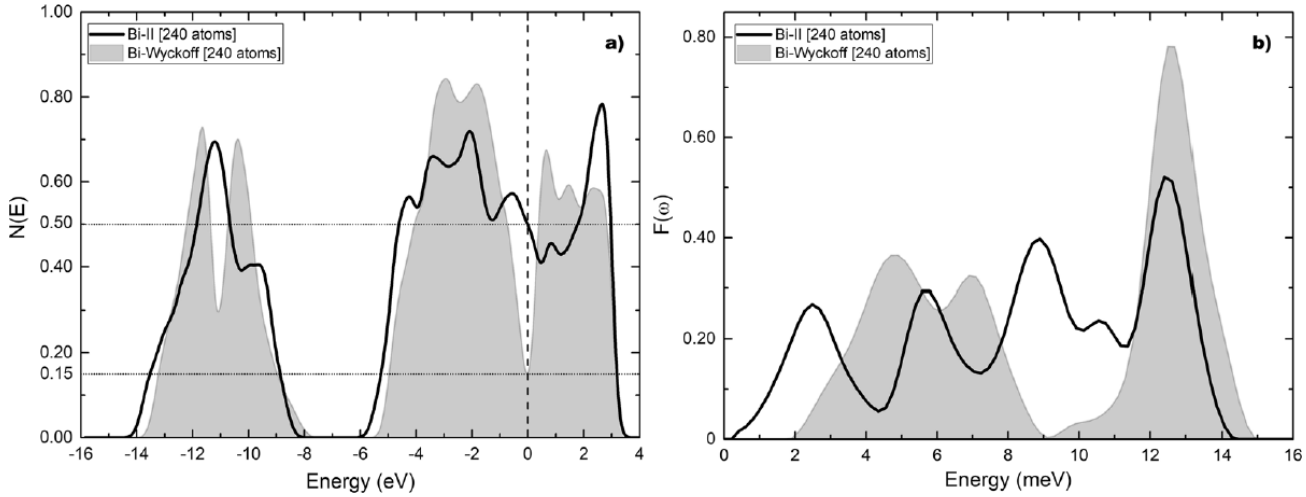

FIGURE 7.14. a) $N(E)$ and b) $F(\omega)$ for Bi-II (black solid line) compared to the results for the Wyckoff structure (grey). Reported in Ref. [160].

Bi-III

The eDoS for the Chen, Iwasaki, and Kikegawa [165] structure is shown in Figure 7.15 a) compared to the Wyckoff phase. $N(E_F)$ is 0.62 electrons per atom. In Figure 7.15 b) comparison for the vDoS is given. The Debye temperature is $96.4\,\mathrm{K}$.

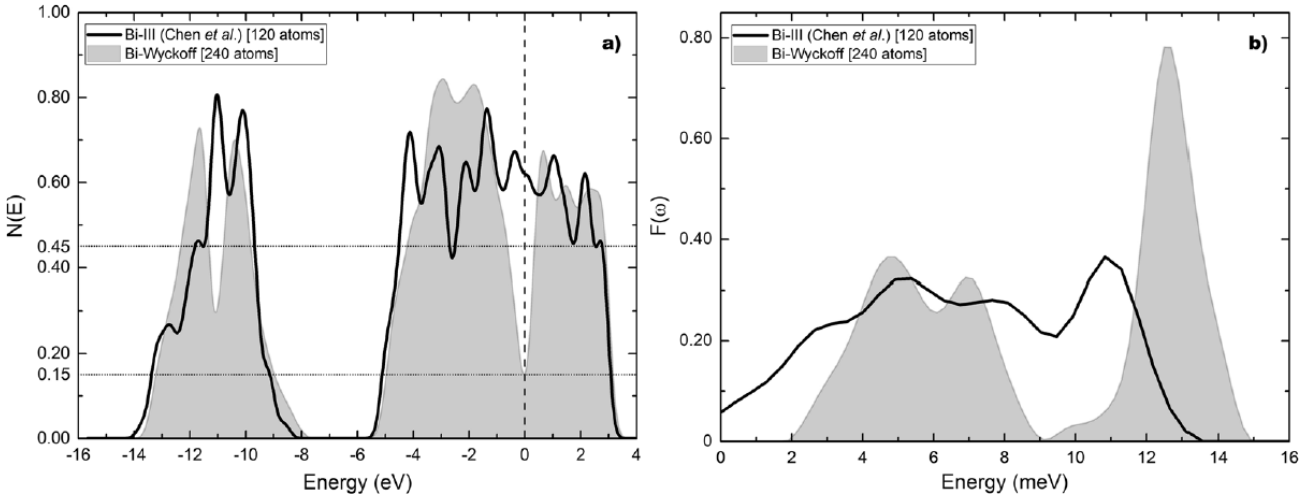

FIGURE 7.15. a) $N(E)$ and b) $F(\omega)$ for Bi-III of Chen *et al.* (black solid line) compared to the results for the Wyckoff structure (grey). Reported in Ref. [160].

Figures 7.16 are comparisons between our structure, *á la* Häussermann (based on the data reported by McMahon *et al.*), compared to Wyckoff's. $N(E_F)$ is 0.45 electrons per atom. The calculated Debye temperature is $144.4\,\mathrm{K}$.

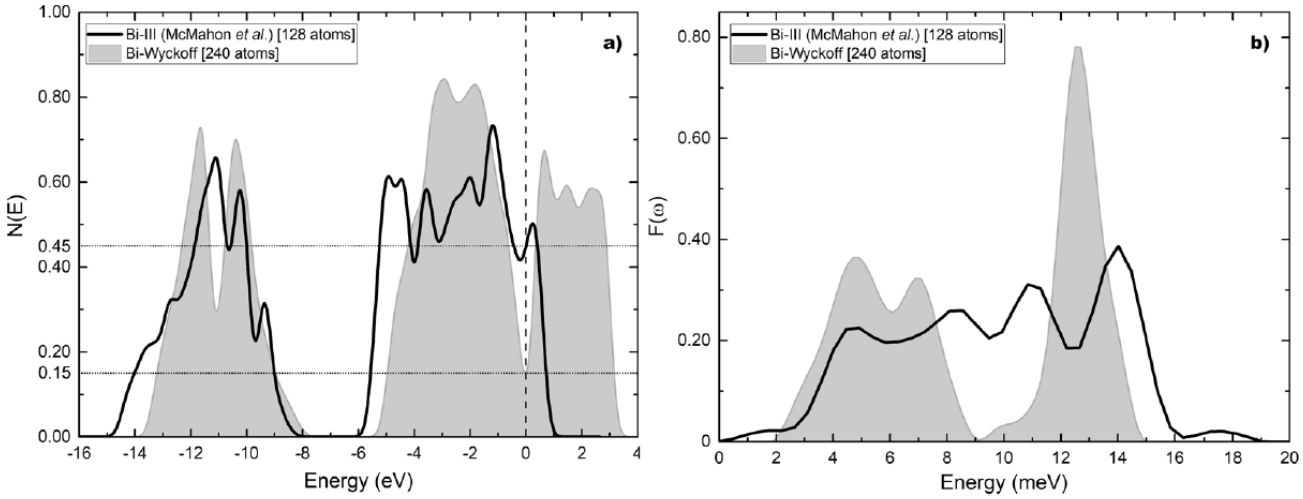

FIGURE 7.16. a) $N(E)$ and b) $F(\omega)$ for our commensurate representation of McMahon results (black solid line) compared to the results for the Wyckoff structure (grey). Reported in Ref. [160].

Bi-IV

The results obtained for the eDoS and the vDoS of the Bi-IV phase are given in Figure 7.17. Figure 7.17 a) shows that $N(E_F)$ is 0.53 electrons per atom for Bi-IV. Figure 7.17 b) presents a comparison of the two vibrational densities of states. The calculation for the Debye temperature leads to $102.1\,\mathrm{K}$.

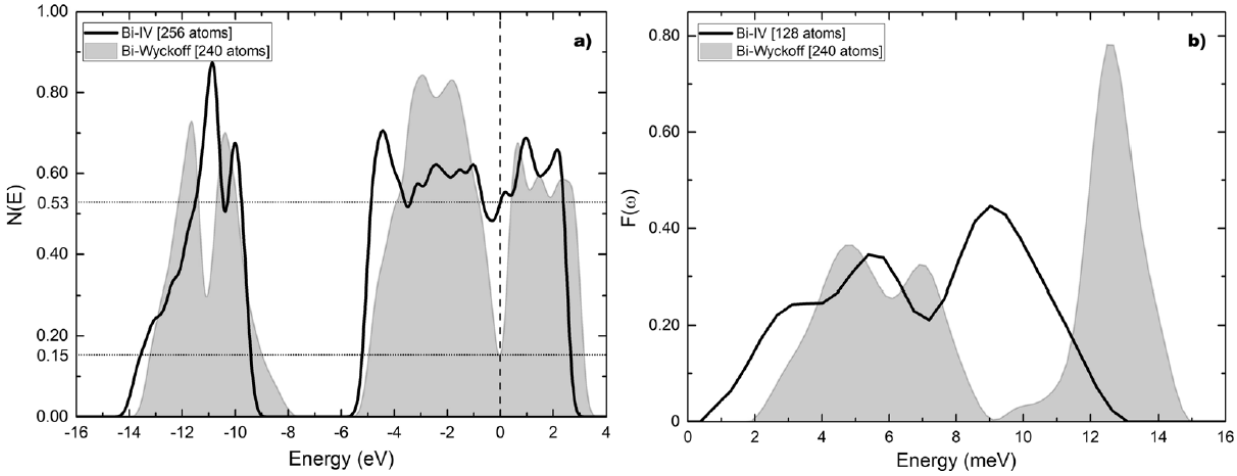

FIGURE 7.17. a) $N(E)$ and b) $F(\omega)$ for Bi-IV (black solid line) compared to the results for the Wyckoff structure (grey). Reported in Ref. [160].

Bi-V

The results for $N(E)$ and $F(\omega)$ for Bi-V and the Wyckoff structure are depicted in Figure 7.18 a) and b), respectively. The calculations give 0.56 electrons per atom for $N(E_F)$. From Figure 7.18 b), the calculated Debye temperature is $137.8\,\mathrm{K}$.

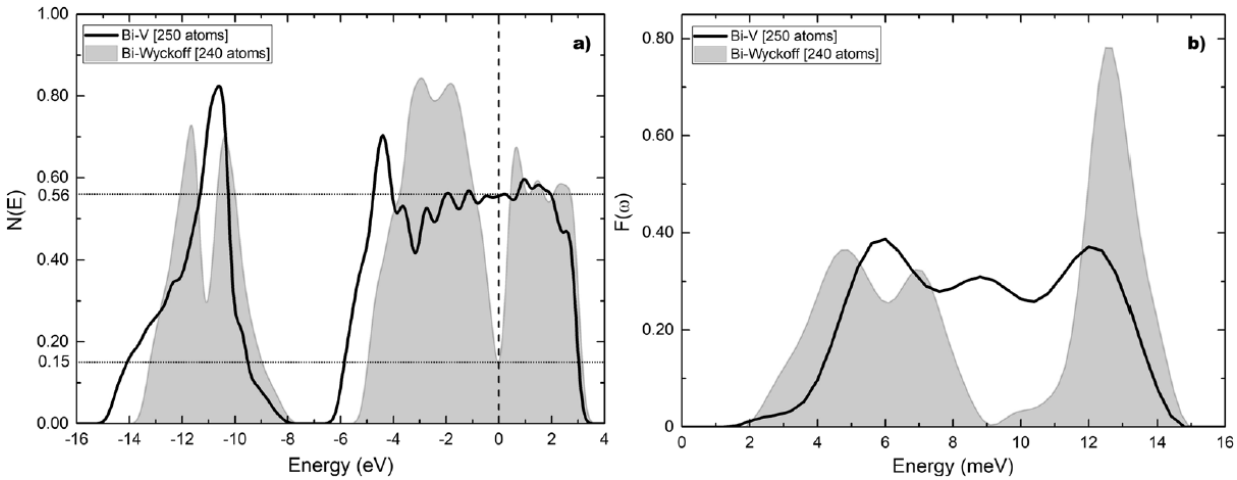

FIGURE 7.18. a) $N(E)$ and b) $F(\omega)$ for Bi-V (black solid line) compared to the results for the Wyckoff structure (grey). Reported in Ref. [160].

7.3.2 Calculation of the T_c

As has became usual in this investigation, in order to estimate the T_c from equation (3.8) in the *á la* Mata-Pinzón *et al.* approach, it is required to known $N(E_F)$ and the Θ_D for each phase. In is important to mention that all but the Bi-IV phase have been experimentally found to superconduct; thus our T_c calculation for the Bi-IV phase is of predictive character.

Thus, following the method in subsection 3.3.6, we identify the material R as the Bi-I (Wyckoff) phase and the material Q as the Bi-II, Bi-III, Bi-IV and Bi-V phases. Thus, the identifications: $R \to W$ and $Q \to Q$ in equations (3.4) to (3.8) lead to:

$$\eta = \frac{N^Q(E_F)}{N^W(E_F)} \tag{7.4}$$

from equation (3.6), for a phase-to-Wyckoff ratio of $N(E_F)$, and

$$\mu = \frac{\Theta_D^Q}{\Theta_D^W} \tag{7.5}$$

from equation (3.7) for a phase-to-Wyckoff ratio of Θ_D.

Taking the reference value of $T_c^R \to T_c^W = 1.3\,\mathrm{mK}$ as determined from the calculations of Mata-Pinzón *et al.* [63], the superconducting critical temperature for each phase T_c^Q is determined by equation (3.8) as follows:

$$T_c^Q = \mu \left[T_c^W\right]^{1/\eta} \left[1.13\,\Theta_D^W\right]^{(\eta-1)/\eta}. \tag{7.6}$$

From the reported data for $N(E_F)$ and Θ_D in Table 7.4 and equations (7.4) and (7.5), the critical temperatures for each phase can be calculated by means or equation (7.6). These results are shown in Table 7.5, where the predicted, the calculated, and the measured T_cs are specified by the notation T_c^p, T_c^c, and T_c^m, respectively.

TABLE 7.5. Values for the parameters η and μ defined in equations (7.4) and (7.5) for the bismuth phases (see Table 7.4 also). The predicted (T_c^p) and the calculated (T_c^c) critical temperatures were obtained by equation (7.6). The measured critical temperature (T_c^m) are also reported for comparison.

Phase	η [a]	μ [b]	T_c^p [K]	T_c^c [K]	T_c^m [K]
Bi-I	1.00	1.00	0.0013	-	0.00053
Bi-II	3.33	0.86	-	3.9	3.9
Bi-III [c]	4.13	0.72	-	6.5	7
Bi-III [d]	3.00	1.8	-	3.5	7
Bi-IV	3.53	0.76	4.25	-	-
Bi-V	3.73	1.03	-	6.8	8

[a] From eq. (7.4)

[b] From eq. (7.5)

[c] Chen, Iwasaki, and Kikegawa [165].

[d] McMahon, Degtyareva, and Nelmes [167].

7.3.3 Discussion

The *á la* Mata-Pinzón *et al.* approach, originally devised to predict a then-unknown superconducting state in the Bi-I phase, shows to also give good results in determining critical superconducting temperatures of its under-pressure phases. Even though the constant-Cooper-piring-potential assumption may be bold, especially because we are dealing with under-pressure caused phase-changes, it is rewarding that our calculations for the critical temperatures agree very well with the experimental measurements.

The Bi-III phase requires a more extended study to determine if a better commensurate representative supercell can be constructed, such that it gives the correct properties observed on experiments. Or even better, to conceive an *ab initio* method to study incommensurate structures. Meanwhile, our contribution to the study of superconductivity in the several phases and structures of bismuth relies on the Mata-Pinzón *et al.* approach and it is encouraging that from the calculation of the material's electronic and vibrational energy spectra, this facile approach may be applied to other phases and alloys of bismuth, as well as to other systems.

This page intentionally left blank

8 Conclusions to Part II and Future work

From this work, we can seek to understand the superconducting features present in this versatile and fascinating material that bismuth is. The fact that Mata-Pinzón *et al.* [63] could predict the superconducting transition temperature of Bi-I, already corroborated by experiment, and the fact that we have predictions for the T_c in bismuth bilayers and for the phase Bi-IV, not experimentally studied yet, gives us confidence that, at least for bismuth, our approach is sound since the calculated superconducting transition temperatures are all very close to experiment, where they exist.

Calculating the pairing potential remains a challenge. However, computational simulations based on current *state-of the-art* codes are helping to accomplish this. With the present approach one can obtain reasonable approximations to the superconducting transition temperatures if one deals with the same material in different phases. Also, computational simulations based on DFT have evolved favorably such that the calculations for the electronic and vibrational densities of states give us confidence so one can infer meaningful conclusions. More tests and predictions on superconductivity awaits for exploration in different materials, pure and alloyed.

This page intentionally left blank

Bibliography

[1] Philip W. Anderson. "More Is Different". *Science* **177** (4047), 1972, 393–396. DOI: 10.1126/science.177.4047.393.

[2] Neil W. Ashcroft and N. David Mermin. *Solid State Physics*. Brooks/Cole, Cengage Learning, 1976.

[3] Spencer R. Weart. "The Birth of the Solid-State Physics Community". *Physics Today* **41** (7), 1988, 38–45. DOI: 10.1063/1.881124.

[4] John M. Ziman. *Models of Disorder*. Cambridge University Press, 1979.

[5] Salvatore Torquato. *Random Heterogeneous Materials*. Springer New York, 2002. DOI: 10.1007/978-1-4757-6355-3.

[6] Kurt Binder and Walter Kob. *Glassy Materials and Disordered Solids: An Introduction to Their Statistical Mechanics*. World Scientific Publishing Company, 2005.

[7] Lothar Nordheim. "Zur Elektronentheorie der Metalle. I". *Ann. Phys. (Leipzig)* **9**, 1931, 607–640. DOI: 10.1002/andp.19314010507.

[8] A. Bansil and M. Pessa. "Surface and Bulk Electronic Structure of Disordered Metallic Alloys". *Physica Scripta* **T4**, 1983, 52–60. DOI: 10.1088/0031-8949/1983/T4/009.

[9] L. Bellaiche and David Vanderbilt. "Virtual crystal approximation revisited: Application to dielectric and piezoelectric properties of perovskites". *Physical Review B* **61** (12), 2000, 7877–7882. DOI: 10.1103/PhysRevB.61.7877.

[10] Stefano de Gironcoli, Paolo Giannozzi, and Stefano Baroni. "Structure and thermodynamics of Si_xGe_{1-x} alloys from ab initio Monte Carlo simulations". *Physical Review Letters* **66** (16), 1991, 2116–2119. DOI: 10.1103/PhysRevLett.66.2116.

[11] P. Slavenburg. "$TiFe_{1-x}Co_x$ alloys and the influence of antistructural atoms". *Physical Review B* **55** (24), 1997, 16110–16121. DOI: 10.1103/PhysRevB.55.16110.

[12] L. Bellaiche, S.-H. Wei, and Alex Zunger. "Band gaps of GaPN and GaAsN alloys". *Applied Physics Letters* **70** (26), 1997, 3558–3560. DOI: 10.1063/1.119232.

[13] Changfeng Chen, E. G. Wang, Y. M. Gu, D. M. Bylander, and Leonard Kleinman. "Unexpected band-gap collapse in quaternary alloys at the group-III-nitride/GaAs interface: GaAlAsN". *Physical Review B* **57** (7), 1998, 3753–3756. DOI: 10.1103/PhysRevB.57.3753.

[14] J. Korringa. “Dispersion theory for electrons in a random lattice with applications to the electronic structure of alloys”. *Journal of Physics and Chemistry of Solids* **7** (2-3), 1958, 252–258. DOI: 10.1016/0022-3697(58)90270-1.

[15] J. L. Beeby. “Electronic Structure of Alloys”. *Physical Review* **135** (1A), 1964, A130–A143. DOI: 10.1103/PhysRev.135.A130.

[16] R. J. Elliott, J. A. Krumhansl, and P. L. Leath. “The theory and properties of randomly disordered crystals and related physical systems”. *Reviews of Modern Physics* **46** (3), 1974, 465–543. DOI: 10.1103/RevModPhys.46.465.

[17] Paul Soven. “Coherent-Potential Model of Substitutional Disordered Alloys”. *Physical Review* **156** (3), 1967, 809–813. DOI: 10.1103/PhysRev.156.809.

[18] D. W. Taylor. “Vibrational Properties of Imperfect Crystals with Large Defect Concentrations”. *Physical Review* **156** (3), 1967, 1017–1029. DOI: 10.1103/PhysRev.156.1017.

[19] I. A. Abrikosov and B. Johansson. “Applicability of the coherent-potential approximation in the theory of random alloys”. *Physical Review B* **57** (22), 1998, 14164–14173. DOI: 10.1103/PhysRevB.57.14164.

[20] Subhradip Ghosh, P. L. Leath, and Morrel H. Cohen. “Phonons in random alloys: The itinerant coherent-potential approximation”. *Physical Review B* **66** (21), 2002, 214206. DOI: 10.1103/PhysRevB.66.214206.

[21] Alex Zunger, S.-H. Wei, L. G. Ferreira, and James E. Bernard. “Special quasirandom structures”. *Physical Review Letters* **65** (3), 1990, 353–356. DOI: 10.1103/PhysRevLett.65.353.

[22] S.-H. Wei, L. G. Ferreira, James E. Bernard, and Alex Zunger. “Electronic properties of random alloys: Special quasirandom structures”. *Physical Review B* **42** (15), 1990, 9622–9649. DOI: 10.1103/PhysRevB.42.9622.

[23] Chao Jiang, C. Wolverton, Jorge Sofo, Long-Qing Chen, and Zi-Kui Liu. “First-principles study of binary bcc alloys using special quasirandom structures”. *Physical Review B* **69** (21), 2004, 214202. DOI: 10.1103/PhysRevB.69.214202.

[24] A. Chroneos, C. Jiang, R. W. Grimes, and U. Schwingenschlögl. “Special quasirandom structures for binary/ternary group IV random alloys”. *Chemical Physics Letters* **493** (1-3), 2010, 97–102. DOI: 10.1016/j.cplett.2010.04.068.

[25] Shen Wang, Jun Xiong, Da Li, Qiang Zeng, Min Xiong, and Xiaosong Chai. “Comparison of two calculation models for high entropy alloys: Virtual crystal approximation and special quasi-random structure”. *Materials Letters* **282**, 2021, 128754. DOI: 10.1016/j.matlet.2020.128754.

[26] V. Sorkin, S. Chen, Teck L. Tan, Z. G. Yu, M. Man, and Y. W. Zhang. "First-principles-based high-throughput computation for high entropy alloys with short range order". *Journal of Alloys and Compounds* **882**, 2021, 160776. DOI: 10.1016/j.jallcom.2021.160776.

[27] A. van de Walle *et al.* "Efficient stochastic generation of special quasirandom structures". *Calphad* **42**, 2013, 13–18. DOI: 10.1016/j.calphad.2013.06.006.

[28] Kohei Shinohara, Atsuto Seko, Takashi Horiyama, and Isao Tanaka. "Finding well-optimized special quasirandom structures with decision diagram". *Physical Review Materials* **5** (11), 2021, 113803. DOI: 10.1103/PhysRevMaterials.5.113803.

[29] Walter A. Harrison. *Solid State Theory*. Dover Publications, Inc., 1980.

[30] Walter A. Harrison. *Electronic Structure and the Properties of Solids: the physics of the chemical bond*. Dover Publications, Inc., 1989.

[31] Harald Ibach and Hans Lüth. *Solid-State Physics. An Introduction to Principles of Materials Science*. 4th ed. Springer-Verlag, 2009.

[32] Adrian P. Sutton. *Electronic Structure of Materials*. Oxford University Press, 1993.

[33] Uichiro Mizutani. *Hume-Rothery Rules for Structurally Complex Alloy Phases*. CRC Press, 2016.

[34] Joel I. Gersten and Frederick W. Smith. *The Physics and Chemistry of Materials*. John Wiley & Sons, Inc., 2001.

[35] Ben A. Green and Ariel A. Valladares. "Low-temperature specific heats of AgAu alloys". *Physical Review* **142** (2), 1966, 379–383. DOI: 10.1103/PhysRev.142.379.

[36] A. J. McAlister, E. A. Stern, and J. C. McGroddy. "Faraday Effect and Fermi Surfaces of the Silver-Gold Alloy System". *Physical Review* **140** (6A), 1965, A2105–A2109. DOI: 10.1103/PhysRev.140.A2105.

[37] James C. McGroddy, Archie J. McAlister, and Edward A. Stern. "Polar Reflection Faraday Effect in Silver and Gold". *Physical Review* **139** (6A), 1965, A1844–A1848. DOI: 10.1103/PhysRev.139.A1844.

[38] Jonah Erlebacher, Michael J Aziz, Alain Karma, Nikolay Dimitrov, and Karl Sieradzki. "Evolution of nanoporosity in dealloying". *Nature* **410** (6827), 2001, 450–453. DOI: 10.1038/35068529.

[39] Jonah Erlebacher. "An Atomistic Description of Dealloying". *Journal of the Electrochemical Society* **151** (10), 2004, C614. DOI: 10.1149/1.1784820.

[40] Ulises Santiago Cortés. "Simulación de sistemas metálicos amorfos y porosos de elementos nobles." PhD thesis. Universidad Nacional Autónoma de México, 2011.

[41] Branko Zugic *et al.* "Dynamic restructuring drives catalytic activity on nanoporous gold–silver alloy catalysts". *Nature Materials* **16** (5), 2016, 558–564. DOI: 10.1038/nmat4824.

[42] Zhu Liu and Peter C. Searson. "Single Nanoporous Gold Nanowire Sensors". *Journal of Physical Chemistry B* **110** (9), 2006, 4318–4322. DOI: 10.1021/jp056940t.

[43] Arne Wittstock, Jürgen Biener, and Marcus Bäumer. "Nanoporous gold: a new material for catalytic and sensor applications". *Physical Chemistry Chemical Physics* **12** (40), 2010, 12919. DOI: 10.1039/c0cp00757a.

[44] Douglas L. Martin. "Specific Heat below 3 K of Silver-Gold Alloys". *Physical Review* **176** (3), 1968, 790–796. DOI: 10.1103/PhysRev.176.790.

[45] Thomas H. Davis and John A Rayne. "Specific Heat and Residual Resistivity of Binary and Ternary Noble-Metal Alloys". *Physical Review B* **6** (8), 1972, 2931–2942. DOI: 10.1103/PhysRevB.6.2931.

[46] Ben A. Green and Harvey V. Culbert. "Low-Temperature Specific Heats of AgSn Alloys". *Physical Review* **137** (4A), 1965, A1168–A1171. DOI: 10.1103/PhysRev.137.A1168.

[47] Lavern C. Clune and Ben A. Green. "Low-Temperature Specific Heats of α-CuSn and α-CuZn Alloys". *Physical Review* **144** (2), 1966, 525–528. DOI: 10.1103/PhysRev.144.525.

[48] Theodore A. Will and Ben A. Green. "Specific Heats of Au and AuSn at Low Temperatures". *Physical Review* **150** (2), 1966, 519–522. DOI: 10.1103/PhysRev.150.519.

[49] Ben A. Green. "Low-Temperature Specific Heats of Silver-Zinc Alloys. The Effect of Lattice Dilatation". *Physical Review* **144** (2), 1966, 528–533. DOI: 10.1103/PhysRev.144.528.

[50] Edward A. Stern. "Charging and the Properties of Alloys". *Physical Review* **144** (2), 1966, 545–552. DOI: 10.1103/PhysRev.144.545.

[51] E. Haga. "Electronic specific heats of silver-gold alloys". *Proceedings of the Physical Society* **91** (1), 1967, 169–176. DOI: 10.1088/0370-1328/91/1/325.

[52] K. Kokko, E. Ojala, and K. Mansikka. "Fermi Level Density of States in AgAu Alloys. Nuclear Magnetic Spin-Lattice Relaxation Rate and Low-Temperature Specific Heat". *Physica status solidi (b)* **153** (1), 1989, 235–241. DOI: 10.1002/pssb.2221530124.

[53] Michael Tinkham. *Introduction to Superconductivity*. Dover Publications, Inc., 2004.

[54] H. Kamerlingh Onnes. "Further Experiments with Liquid Helium. D. On the Change of the Electrical Resistance of Pure Metals at very low Temperatures, etc. V. The Disappearance of the resistance of mercury", 1911, 264–266. DOI: 10.1007/978-94-009-2079-8_16.

[55] J. Bardeen, L. N. Cooper, and J. R. Schrieffer. "Theory of Superconductivity". *Physical Review* **108** (5), 1957, 1175–1204. DOI: 10.1103/PhysRev.108.1175.

[56] U. Gottlieb, J. C. Lasjaunias, J. L. Tholence, O. Laborde, O. Thomas, and R. Madar. "Superconductivity in $TaSi_2$ single crystals". *Physical Review B* **45** (9), 1992, 4803–4806. DOI: 10.1103/PhysRevB.45.4803.

[57] Liang L. Zhao, Stefan Lausberg, H. Kim, M. A. Tanatar, Manuel Brando, R. Prozorov, and E. Morosan. "Type-I superconductivity in $YbSb_2$ single crystals". *Physical Review B* **85** (21), 2012, 214526. DOI: 10.1103/PhysRevB.85.214526.

[58] J. Beare *et al.* "μSR and magnetometry study of the type-I superconductor BeAu". *Physical Review B* **99** (13), 2019, 134510. DOI: 10.1103/PhysRevB.99.134510.

[59] Darren C. Peets, Erjian Cheng, Tianping Ying, Markus Kriener, Xiaoping Shen, Shiyan Li, and Donglai Feng. "Type-I superconductivity in Al_6Re". *Physical Review B* **99** (14), 2019, 144519. DOI: 10.1103/PhysRevB.99.144519.

[60] W. Buckel and R. Hilsch. "Einfluß der Kondensation bei tiefen Temperaturen auf den elektrischen Widerstand und die Supraleitung für verschiedene Metalle". *Zeitschrift für Physik* **138** (2), 1954, 109–120. DOI: 10.1007/BF01337903.

[61] Werner Buckel. "Elektronenbeugungs-Aufnahmen von dünnen Metallschichten bei tiefen Temperaturen". *Zeitschrift für Physik* **138** (2), 1954, 136–150. DOI: 10.1007/BF01337905.

[62] J. S. Shier and D. M. Ginsberg. "Superconducting Transitions of Amorphous Bismuth Alloys". *Physical Review* **147** (1), 1966, 384–391. DOI: 10.1103/PhysRev.147.384.

[63] Zaahel Mata-Pinzón, Ariel A. Valladares, Renela M. Valladares, and Alexander Valladares. "Superconductivity in Bismuth. A New Look at an Old Problem". *PLOS ONE* **11** (1), 2016, e0147645. DOI: 10.1371/journal.pone.0147645.

[64] Om Prakash, Anil Kumar, A. Thamizhavel, and S. Ramakrishnan. "Evidence for bulk superconductivity in pure bismuth single crystals at ambient pressure". *Science* **355** (6320), 2017, 52–55. DOI: 10.1126/science.aaf8227.

[65] Yufeng Li, Enyu Wang, Xiyu Zhu, and Hai-Hu Wen. "Pressure-induced superconductivity in Bi single crystals". *Physical Review B* **95** (2), 2017, 024510. DOI: 10.1103/PhysRevB.95.024510.

[66] B. T. Matthias, A. Jayaraman, T. H. Geballe, K. Andres, and E. Corenzwit. "Many More Superconducting Bismuth Phases". *Physical Review Letters* **17** (12), 1966, 640–643. DOI: 10.1103/PhysRevLett.17.640.

[67] Samantha M. Clarke *et al.* "Creating Binary Cu–Bi Compounds via High-Pressure Synthesis: A Combined Experimental and Theoretical Study". *Chemistry of Materials* **29** (12), 2017, 5276–5285. DOI: 10.1021/acs.chemmater.7b01418.

[68] Kai Guo *et al.* "Weak Interactions under Pressure: *hp*-CuBi and Its Analogues". *Angewandte Chemie International Edition* **56** (20), 2017, 5620–5624. DOI: 10.1002/anie.201700712.

[69] N. E. Alekseevskii, V. V. Bondar, and Yu. M. Polukarov. "The superconductivity of electrolytically deposited copper-bismuth alloys". *JETP* **11** (1), 1960, 213–214.

[70] R. S. Averback, P. R. Okamoto, A. C. Baily, and B. Stritzker. “Ion beam mixing and superconductivity in Cu-Bi”. *Nuclear Instruments and Methods in Physics Research Section B: Beam Interactions with Materials and Atoms* **7-8**, 1985, 556–560. DOI: 10.1016/0168-583X(85)90432-X.

[71] Samantha M. Clarke *et al.* “Discovery of a Superconducting Cu-Bi Intermetallic Compound by High-Pressure Synthesis”. *Angewandte Chemie International Edition* **55** (43), 2016, 13446–13449. DOI: 10.1002/anie.201605902.

[72] F. R. Corrigan and F. P. Bundy. “Direct transitions among the allotropic forms of boron nitride at high pressures and temperatures”. *The Journal of Chemical Physics* **63** (9), 1975, 3812. DOI: 10.1063/1.431874.

[73] V. L. Solozhenko and V. Z. Turkevich. “Thermoanalytical study of the polymorphic transformation of cubic into graphite-like boron nitride”. *Journal of Thermal Analysis* **38** (5), 1992, 1181–1188. DOI: 10.1007/BF01979178.

[74] H. Sachdev, R. Haubner, H. Nöth, and B. Lux. “Investigation of the c-BN/h-BN phase transformation at normal pressure”. *Diamond and Related Materials* **6** (2-4), 1997, 286–292. DOI: 10.1016/S0925-9635(96)00697-8.

[75] R. H. Wentorf. “Cubic Form of Boron Nitride”. *The Journal of Chemical Physics* **26** (4), 1957, 956–956. DOI: 10.1063/1.1745964.

[76] H. R. Philipp and E. A. Taft. “Optical Properties of Diamond in the Vacuum Ultraviolet”. *Physical Review* **127** (1), 1962, 159–161. DOI: 10.1103/PhysRev.127.159.

[77] Joshua D. Caldwell, Igor Aharonovich, Guillaume Cassabois, James H. Edgar, Bernard Gil, and D. N. Basov. “Photonics with hexagonal boron nitride”. *Nature Reviews Materials* **4** (8), 2019, 552–567. DOI: 10.1038/s41578-019-0124-1.

[78] Seokmo Hong *et al.* “Ultralow-dielectric-constant amorphous boron nitride”. *Nature* **582** (7813), 2020, 511–514. DOI: 10.1038/s41586-020-2375-9.

[79] Soumyabrata Roy *et al.* “Structure, Properties and Applications of Two-Dimensional Hexagonal Boron Nitride”. *Advanced Materials* **33** (44), 2021, 2101589. DOI: 10.1002/adma.202101589.

[80] Patel Mayurkumar Revabhai, Rakesh Kumar Singhal, Hirakendu Basu, and Suresh Kumar Kailasa. “Progress on boron nitride nanostructure materials: properties, synthesis and applications in hydrogen storage and analytical chemistry”. *Journal of Nanostructure in Chemistry* **13** (1), 2022, 1–41. DOI: 10.1007/s40097-022-00490-5.

[81] Myron J. Rand and James F. Roberts. “Preparation and Properties of Thin Film Boron Nitride”. *Journal of The Electrochemical Society* **115** (4), 1968, 423. DOI: 10.1149/1.2411238.

[82] Makoto Hirayama and Katsufusa Shohno. "CVD-BN for Boron Diffusion in Si and Its Application to Si Devices". *Journal of The Electrochemical Society* **122** (12), 1975, 1671–1676. DOI: 10.1149/1.2134107.

[83] S. P. S. Arya and A. D'Amico. "Preparation, properties and applications of boron nitride thin films". *Thin Solid Films* **157** (2), 1988, 267–282. DOI: 10.1016/0040-6090(88)90008-9.

[84] Nicholas R. Glavin *et al.* "Amorphous Boron Nitride: A Universal, Ultrathin Dielectric For 2D Nanoelectronics". *Advanced Functional Materials* **26** (16), 2016, 2640–2647. DOI: 10.1002/adfm.201505455.

[85] Yu. N. Novikov and V. A. Gritsenko. "The charge transport mechanism in amorphous boron nitride". *Journal of Non-Crystalline Solids* **544**, 2020, 120213. DOI: 10.1016/j.jnoncrysol.2020.120213.

[86] Takashi Taniguchi, Koji Kimoto, Masataka Tansho, Shigeo Horiuchi, and Shinobu Yamaoka. "Phase Transformation of Amorphous Boron Nitride under High Pressure". *Chemistry of Materials* **15** (14), 2003, 2744–2751. DOI: 10.1021/cm021763j.

[87] H. Lorenz and I. Orgzall. "In situ observation of the crystallization of amorphous boron nitride at high pressures and temperatures". *Scripta Materialia* **52** (6), 2005, 537–540. DOI: 10.1016/j.scriptamat.2004.10.016.

[88] Takahiro Mochizuki, Yusuke Yamamoto, Naokazu Idota, Fumio Kawamura, Takashi Taniguchi, and Yoshiyuki Sugahara. "Crystallization behavior of cubic boron nitride from an amorphous BN precursor via high-pressure, high-temperature treatment with controlled water addition". *Journal of the European Ceramic Society* **36** (15), 2016, 3565–3569. DOI: 10.1016/j.jeurceramsoc.2016.06.027.

[89] W. Sekkal, B. Bouhafs, H. Aourag, and M. Certier. "Molecular-dynamics simulation of structural and thermodynamic properties of boron nitride". *Journal of Physics: Condensed Matter* **10** (23), 1998, 4975–4984. DOI: 10.1088/0953-8984/10/23/006.

[90] D. G. McCulloch, D. R. McKenzie, and C. M. Goringe. "Ab initio study of structure in boron nitride, aluminum nitride and mixed aluminum boron nitride amorphous alloys". *Journal of Applied Physics* **88** (9), 2000, 5028–5032. DOI: 10.1063/1.1316790.

[91] Murat Durandurdu. "Amorphous boron nitride at high pressure". *Philosophical Magazine* **96** (18), 2016, 1950–1964. DOI: 10.1080/14786435.2016.1183830.

[92] Murat Durandurdu. "Tetrahedral amorphous boron nitride: A hard material". *Journal of the American Ceramic Society* **103** (2), 2020, 973–978. DOI: 10.1111/jace.16803.

[93] R. Zedlitz, M. Heintze, and M. B. Schubert. "Properties of amorphous boron nitride thin films". *Journal of Non-Crystalline Solids* **198-200** (PART 1), 1996, 403–406. DOI: 10.1016/0022-3093(95)00748-2.

[94] P. Hohenberg and W. Kohn. "Inhomogeneous Electron Gas". *Physical Review* **136** (3B), 1964, B864–B871. DOI: 10.1103/PhysRev.136.B864.

[95] W. Kohn and L. J. Sham. "Self-Consistent Equations Including Exchange and Correlation Effects". *Physical Review* **140** (4A), 1965, A1133–A1138. DOI: 10.1103/PhysRev.140.A1133.

[96] Richard M. Martin. *Electronic Structure: basic theory and practical methods*. Second edition. Cambridge University Press, 2020.

[97] M. Born and R. Oppenheimer. "Zur Quantentheorie der Molekeln". *Annalen der Physik* **389** (20), 1927, 457–484. DOI: 10.1002/andp.19273892002.

[98] W. Kohn and L. J. Sham. "Quantum Density Oscillations in an Inhomogeneous Electron Gas". *Physical Review* **137** (6A), 1965, A1697–A1705. DOI: 10.1103/PhysRev.137.A1697.

[99] Feliciano Giustino. *Materials Modelling using Density Functional Theory. Properties and Predictions*. 1st ed. Oxford University Press, 2014.

[100] David S. Sholl and Janice A. Steckel. *Density Functional Theory. A Practical Introduction*. John Wiley & Sons, Inc., 2009.

[101] Eberhard Engel and Reiner M. Dreizler. *Density Functional Theory. An Advanced Course*. Springer Berlin Heidelberg, 2011. DOI: 10.1007/978-3-642-14090-7.

[102] Richard M. Martin, Lucia Reining, and David M. Ceperley. *Interacting Electrons. Theory and Computational Approaches*. Cambridge University Press, 2016.

[103] Daan Frenkel and Berend Smit. *Understanding Molecular Simulation*. 2nd ed. Academic Press, 2002.

[104] R. Car and M. Parrinello. "Unified Approach for Molecular Dynamics and Density-Functional Theory". *Physical Review Letters* **55** (22), 1985, 2471–2474. DOI: 10.1103/PhysRevLett.55.2471.

[105] Dominik Marx and Jürg Hutter. *Ab Initio Molecular Dynamics: Basic Theory and Advanced Methods*. Cambridge University Press, 2009.

[106] Robert H. Swendsen. *An Introduction to Statistical Mechanics and Thermodynamics*. Oxford University Press, 2012.

[107] Richard C. Tolman. *The Principles of Statistical Mechanics*. Dover Publications, Inc., 1979.

[108] Terren L. Hill. *An Introduction to Statistical Thermodynamics*. Dover Publications, Inc., 1986.

[109] Shūichi Nosé. "A molecular dynamics method for simulations in the canonical ensemble." *Molecular Physics* **52**, 2 1984. DOI: 10.1080/00268978400101201.

[110] Shūichi Nosé. "A unified formulation of the constant temperature molecular dynamics methods". *Journal of Chemical Physics* **81** (1), 1984, 511–519. DOI: 10.1063/1.447334.

[111] William G. Hoover. "Canonical dynamics: Equilibrium phase-space distributions". *Physical Review A* **31** (3), 1985, 1695–1697. DOI: 10.1103/PhysRevA.31.1695.

[112] B. Delley. "An all-electron numerical method for solving the local density functional for polyatomic molecules". *The Journal of Chemical Physics* **92** (1), 1990, 508–517. DOI: 10.1063/1.458452.

[113] B. Delley. "Modern Density Functional Theory: A Tool for Chemistry." Ed. by J. M. Seminario and P. Politzer. Elsevier Science B.V., 1995. Chap. 7. DMol, a Standard Tool for Density Functional Calculations: Review and Advances. Pp. 221–254.

[114] B. Delley. "Fast Calculation of Electrostatics in Crystals and Large Molecules". *Journal of Physical Chemistry* **100** (15), 1996, 6107–6110. DOI: 10.1021/jp952713n.

[115] B. Delley. "From molecules to solids with the DMol3 approach". *The Journal of Chemical Physics* **113** (18), 2000, 7756–7764. DOI: 10.1063/1.1316015.

[116] S. Vosko, L. Wilk, and M. Nusair. "Accurate spin-dependent electron liquid correlation energies for local spin density calculations: a critical analysis". *Canadian Journal of Physics* **58** (8), 1980, 1200–1211. DOI: 10.1139/p80-159.

[117] John P. Perdew, Kieron Burke, and Matthias Ernzerhof. "Generalized Gradient Approximation Made Simple". *Physical Review Letters* **77** (18), 1996, 3865–3868. DOI: 10.1103/PhysRevLett.77.3865.

[118] D. D. Koelling and B. N. Harmon. "A technique for relativistic spin-polarised calculations". *Journal of Physics C: Solid State Physics* **10** (16), 1977, 3107–3114. DOI: 10.1088/0022-3719/10/16/019.

[119] B. Delley. "A scattering theoretic approach to scalar relativistic corrections on bonding". *International Journal of Quantum Chemistry* **69** (3), 1998, 423–433. DOI: 10/fgjmxq.

[120] B. Delley. "Hardness conserving semilocal pseudopotentials". *Physical Review B* **66** (15), 2002, 155125. DOI: 10.1103/PhysRevB.66.155125.

[121] Yoshio Waseda. *The Structure of Non-Crystalline Materials*. McGraw-Hill Inc., 1980.

[122] S. R. Elliott. *Physics of Amorphous Materials*. Longman Scientific & Technical, 1984.

[123] Paolo M. Ossi. *Disordered Materials. An Introduction*. Springer-Verlag, 2006.

[124] Isaías Rodríguez, Renela Valladares, Alexander Valladares, David Hinojosa-Romero, Ulises Santiago, and Ariel A. Valladares. "Correlation: An Analysis Tool for Liquids and for Amorphous Solids". *Journal of Open Source Software* **6** (65), 2021, 2976. DOI: 10.21105/joss.02976.

[125] Herbert B. Callen. *Thermodynamics and an Introduction to Thermostatistics*. 2nd ed. John Wiley & Sons, 1985.

[126] A. A. Maradudin, E. W. Montroll, G. H. Weiss, and I. P. Ipatova. *Theory of Lattice Dynamics in the Harmonic Approximation*. Ed. by Henry Ehrenreich, Frederick Seitz, and David Turnbull. Second edition. Vol. 3. Solid State Physics. Advances in Research and Applications. Academic Press, Inc., 1971.

[127] Loius A. Girifalco. *Statisticlal Mechanics of Solids*. Oxford University Press, 2000.

[128] F. London and H. London. "The electromagnetic equations of the supraconductor". *Proceedings of the Royal Society of London. Series A - Mathematical and Physical Sciences* **149** (866), 1935, 71–88. DOI: 10.1098/rspa.1935.0048.

[129] V. L. Ginzburg and L. D. Landau. "On the theory of superconductivity". *Zhurnal Eksperimental'noi i Teoreticheskoi Fiziki* **20**, 1950, 1064.

[130] *Dassault Systémes BIOVIA. Materials Studio 2016.* 2015.

[131] *DMol^3 Guide. Materials Studio 2016.* 2015.

[132] *Forcite Guide. Materials Studio 2016.* 2015.

[133] Ariel A. Valladares. "A new approach to the ab initio generation of amorphous semiconducting structures. Electronic and vibrational studies". *Glass Materials Research Progress*. Ed. by Jonas C. Wolf and Luka Lange. Nova Science Publishers, Inc., 2008, pp. 61–123.

[134] Fernando Alvarez Ramírez. "Propiedades topológicas, electrónicas y ópticas de silicio amorfo puro y contaminado." PhD thesis. Universidad Nacional Autónoma de México, 2002.

[135] L. M. Mejía Mendoza. "Estudio Computacional de Aleaciones Amorfas Basadas en Silicio-Carbono y Silicio-Germanio." PhD thesis. Universidad Nacional Autónoma de México, 2014.

[136] Cristina Romero Rangel. "Simulaciones Computacionales de Materiales Nanoporosos. El Caso de Carbono." PhD thesis. Universidad Nacional Autónoma de México, 2014.

[137] Zaahel Mata Pinzón. "Propiedades electrónicas y vibracionales y su influencia en la superconductividad del bismuto amorfo y sus aleaciones con plomo, talio y antimonio." PhD thesis. Universidad Nacional Autónoma de México, 2016.

[138] Jonathan Galván Colín. "Atomic structure and properties of amorphous, liquid and amorphous porous Cu-Zr alloys by ab-initio simulations." PhD thesis. Universidad Nacional Autónoma de México, 2016.

[139] Isaías Rodríguez Aguirre. "Cálculo ab initio de propiedades estructurales y electrónicas en aleaciones paladio-hidrógeno (PdHx)." MA thesis. Universidad Nacional Autónoma de México, 2015.

[140] Isaías Rodríguez Aguirre. "Cálculo ab-initio de propiedades estructurales, electrónicas y vibracionales en aleaciones de paladio". PhD thesis. Universidad Nacional Autónoma de México, 2019.

[141] Fernando Alvarez and Ariel A. Valladares. "First-principles simulations of atomic networks and optical properties of amorphous SiN_x alloys". *Physical Review B* **68** (20), 2003, 205203. DOI: 10.1103/PhysRevB.68.205203.

[142] P. Duwez. "Structure and Properties of Glassy Metals". *Annual Review of Materials Science* **6** (1), 1976, 83–117. DOI: 10.1146/annurev.ms.06.080176.000503.

[143] Charlette M. Grigorian and Timothy J. Rupert. "Critical cooling rates for amorphous-to-ordered complexion transitions in Cu-rich nanocrystalline alloys". *Acta Materialia* **206**, 2021, 116650. DOI: 10.1016/j.actamat.2021.116650.

[144] Efthimios Kaxiras and John D. Joannopoulos. *Quantum Theory of Materials*. Cambridge University Press, 2019. DOI: 10.1017/9781139030809.

[145] Göran Grimvall. *Thermophysical Properties of Materials*. North Holland, 1999.

[146] J. C. Kraut and W. B. Stern. "The density of gold-silver-copper alloys and its calculation from the chemical composition". *Gold Bulletin* **33** (2), 2000, 52–55. DOI: 10.1007/BF03216580.

[147] H. Okamoto and T. B. Massalski. "The Ag-Au (Silver-Gold) system". *Bulletin of Alloy Phase Diagrams* **4** (1), 1983, 30–38. DOI: 10.1007/BF02880317.

[148] D. Hinojosa-Romero, I. Rodriguez, A. Valladares, R. M. Valladares, and A. A. Valladares. "Ab initio Study of the Amorphous Cu-Bi System". *MRS Advances* **4** (2), 2019, 81–86. DOI: 10.1557/adv.2019.83.

[149] H. Richter. "Solid Amorphous Bi, Ga, and Fe as Examples of Liquid-Like Amorphous Substances". *Journal of Vacuum Science and Technology* **6** (5), 1969, 855–858. DOI: 10.1116/1.1492720.

[150] Yakun Yuan *et al.* "Three-dimensional atomic packing in amorphous solids with liquid-like structure". *Nature Materials* **21** (1), 2021, 95–102. DOI: 10.1038/s41563-021-01114-z.

[151] H. Grigoriew and J. Leciejewicz. "X-ray and electron microscopy study of amorphous boron nitride films". *Thin Solid Films* **172** (2), 1989, L75–L79. DOI: 10.1016/0040-6090(89)90656-1.

[152] Murat Durandurdu. "Hexagonal nanosheets in amorphous BN: A first principles study". *Journal of Non-Crystalline Solids* **427**, 2015, 41–45. DOI: 10.1016/j.jnoncrysol.2015.07.033.

[153] W. J. Yu, W. M. Lau, S. P. Chan, Z. F. Liu, and Q. Q. Zheng. "Ab initio study of phase transformations in boron nitride". *Physical Review B* **67** (1), 2003, 014108. DOI: 10.1103/PhysRevB.67.014108.

[154] D. Strauch. "BN: phonon dispersion curves, phonon density of states". *Landolt-Börnstein - Group III Condensed Matter*. Ed. by U. Rössler. Vol. 44D. Springer-Verlag, Berlin Heidelberg, 2011, pp. 61–123.

[155] R. W. G. Wyckoff. *Crystal Structures*. Vol. 1. Interscience, New York, 1963.

[156] P. W. Bridgman. "Effects of High Shearing Stress Combined with High Hydrostatic Pressure". *Physical Review* **48** (10), 1935, 825–847. DOI: 10.1103/PhysRev.48.825.

[157] P. W. Bridgman. "Polymorphism, Principally of the Elements, up to 50,000 kg/cm^2". *Physical Review* **48** (11), 1935, 893–906. DOI: 10.1103/PhysRev.48.893.

[158] P. W. Bridgman. "The Resistance of 72 Elements, Alloys and Compounds to 100,000 kg/cm^2". *Proceedings of the American Academy of Arts and Sciences* **81** (4), 1952, 165. DOI: 10.2307/20023677.

[159] W. Klement, A. Jayaraman, and G. C. Kennedy. "Phase Diagrams of Arsenic, Antimony, and Bismuth at Pressures up to 70 kbars". *Physical Review* **131** (2), 1963, 632–637. DOI: 10.1103/PhysRev.131.632.

[160] Isaías Rodríguez, David Hinojosa-Romero, Alexander Valladares, Renela M. Valladares, and Ariel A. Valladares. "A facile approach to calculating superconducting transition temperatures in the bismuth solid phases". *Scientific Reports* **9** (1), 2019. DOI: 10.1038/s41598-019-41401-z.

[161] F. P. Bundy. "Phase Diagram of Bismuth to 130 000 kg/cm^2°C". *Physical Review* **110** (2), 1958, 314–318. DOI: 10.1103/PhysRev.110.314.

[162] Shûsuke Yomo, Nobuo Môri, and Tadayasu Mitsui. "Pressure-Temperature Phase Diagram of Bismuth at Low Temperatures". *Journal of the Physical Society of Japan* **32** (3), 1972, 667–676. DOI: 10.1143/JPSJ.32.667.

[163] N. Lotter and J. Wittig. "Evidence for an Electronic Phase Transition in Bismuth under Pressure". *Europhysics Letters (EPL)* **6** (7), 1988, 659–662. DOI: 10.1209/0295-5075/6/7/015.

[164] H. Iwasaki, J. H. Chen, and T. Kikegawa. "Structural study of the high-pressure phases of bismuth using high-energy synchrotron radiation". *Review of Scientific Instruments* **66** (2), 1995, 1388–1390. DOI: 10.1063/1.1145984.

[165] J. H. Chen, H. Iwasaki, and T. Kikegawa. "Crystal structure of the high pressure phases of bismuth Bi III and Bi III' by high energy synchrotron x-ray diffraction". *High Pressure Research* **15** (3), 1996, 143–158. DOI: 10.1080/08957959608240468.

[166] H. Iwasaki and T. Kikegawa. "Crystal structure of the high pressure phase of antimony SbII". *High Pressure Research* **6** (2), 1990, 121–132. DOI: 10.1080/08957959008203203.

[167] M. I. McMahon, O. Degtyareva, and R. J. Nelmes. "Ba-IV-Type Incommensurate Crystal Structure in Group-V Metals". *Physical Review Letters* **85** (23), 2000, 4896–4899. DOI: 10.1103/PhysRevLett.85.4896.

[168] O. Degtyareva, M. I. McMahon, and R. J. Nelmes. "Crystal Structure of the High Pressure Phase of Bismuth Bi-III". *Materials Science Forum* **378-381**, 2001, 469–475. DOI: 10.4028/www.scientific.net/MSF.378-381.469.

[169] R. J. Nelmes, D. R. Allan, M. I. McMahon, and S. A. Belmonte. "Self-Hosting Incommensurate Structure of Barium IV". *Physical Review Letters* **83** (20), 1999, 4081–4084. DOI: 10.1103/PhysRevLett.83.4081.

[170] Volker Heine. "As weird as they come". *Nature* **403** (6772), 2000, 836–837. DOI: 10.1038/35002691.

[171] M. I. McMahon, T. Bovornratanaraks, D. R. Allan, S. A. Belmonte, and R. J. Nelmes. "Observation of the incommensurate barium-IV structure in strontium phase V". *Physical Review B* **61** (5), 2000, 3135–3138. DOI: 10.1103/PhysRevB.61.3135.

[172] Ulrich Häussermann, Karin Söderberg, and Rolf Norrestam. "Comparative Study of the High-Pressure Behavior of As, Sb, and Bi". *Journal of the American Chemical Society* **124** (51), 2002, 15359–15367. DOI: 10.1021/ja020832s.

[173] M. I. McMahon, O. Degtyareva, R. J. Nelmes, S. van Smaalen, and L. Palatinus. "Incommensurate modulations of Bi-III and Sb-II". *Physical Review B* **75** (18), 2007, 184114. DOI: 10.1103/PhysRevB.75.184114.

[174] O. Degtyareva, M. I. McMahon, and R. J. Nelmes. "High-pressure structural studies of group-15 elements". *High Pressure Research* **24** (3), 2004, 319–356. DOI: 10/d85t9c.

[175] David Hinojosa-Romero, Isaías Rodríguez, Zaahel Mata-Pinzón, Alexander Valladares, Renela Valladares, and Ariel A. Valladares. "Compressed Crystalline Bismuth and Superconductivity — An ab initio computational Simulation". *MRS Advances* **2** (9), 2017, 499–506. DOI: 10.1557/adv.2017.66.

[176] David Hinojosa-Romero, Isaías Rodriguez, Alexander Valladares, Renela M. Valladares, and Ariel A. Valladares. "Possible superconductivity in Bismuth (111) bilayers. Their electronic and vibrational properties from first principles". *MRS Advances* **3** (6-7), 2018, 313–319. DOI: 10.1557/adv.2018.119.

[177] Fang Yang *et al.* "Spatial and Energy Distribution of Topological Edge States in Single Bi(111) Bilayer". *Physical Review Letters* **109** (1), 2012, 016801. DOI: 10.1103/PhysRevLett.109.016801.

[178] C. Sabater, D. Gosálbez-Martínez, J. Fernández-Rossier, J. G. Rodrigo, C. Untiedt, and J. J. Palacios. "Topologically Protected Quantum Transport in Locally Exfoliated Bismuth at Room Temperature". *Physical Review Letters* **110** (17), 2013, 176802. DOI: 10.1103/PhysRevLett.110.176802.

[179] Ilya K. Drozdov *et al.* "One-dimensional topological edge states of bismuth bilayers". *Nature Physics* **10** (9), 2014, 664–669. DOI: 10.1038/nphys3048.

[180] M. Bieniek, T. Woźniak, and P. Potasz. "Study of Spin-Orbit Coupling Effect on Bismuth (111) Bilayer". *Acta Physica Polonica A* **130** (2), 2016, 609–612. DOI: 10.12693/APhysPolA.130.609.

[181] Maciej Bieniek, Tomasz Woźniak, and Paweł Potasz. "Stability of topological properties of bismuth (1 1 1) bilayer". *Journal of Physics: Condensed Matter* **29** (15), 2017, 155501. DOI: 10.1088/1361-648X/aa5e79.

[182] Shuichi Murakami. "Quantum Spin Hall Effect and Enhanced Magnetic Response by Spin-Orbit Coupling". *Physical Review Letters* **97** (23), 2006, 236805. DOI: 10.1103/PhysRevLett.97.236805.

[183] Joel E. Moore. "The birth of topological insulators". *Nature* **464** (7286), 2010, 194–198. DOI: 10.1038/nature08916.

[184] M. Z. Hasan and C. L. Kane. "Colloquium: Topological insulators". *Reviews of Modern Physics* **82** (4), 2010, 3045–3067. DOI: 10.1103/RevModPhys.82.3045.

[185] Xiao-Liang Qi and Shou-Cheng Zhang. "Topological insulators and superconductors". *Reviews of Modern Physics* **83** (4), 2011, 1057–1110. DOI: 10.1103/RevModPhys.83.1057.

[186] Ariel A. Valladares, Isaías Rodríguez, David Hinojosa-Romero, Alexander Valladares, and Renela M. Valladares. "Possible superconductivity in the Bismuth IV solid phase under pressure". *Scientific Reports* **8** (1), 2018. DOI: 10.1038/s41598-018-24150-3.

[187] Wanaruk Chaimayo, Lars F. Lundegaard, Ingo Loa, Graham W. Stinton, Alistair R. Lennie, and Malcolm I. McMahon. "High-pressure, high-temperature single-crystal study of Bi-IV". *High Pressure Research* **32** (3), 2012, 442–449. DOI: 10.1080/08957959.2012.722214.

[188] Philip Brown, Konstantin Semeniuk, Diandian Wang, Bartomeu Monserrat, Chris J. Pickard, and F. Malte Grosche. "Strong coupling superconductivity in a quasiperiodic host-guest structure". *Science Advances* **4** (4), 2018. DOI: 10.1126/sciadv.aao4793.